WARWICK
THE UNIVERSITY OF WARWICK

A Thesis Submitted for the Degree of PhD at the University of Warwick

Permanent WRAP URL:
http://wrap.warwick.ac.uk/79675

Copyright and reuse:
This thesis is made available online and is protected by original copyright.
Please scroll down to view the document itself.
Please refer to the repository record for this item for information to help you to cite it.
Our policy information is available from the repository home page.

For more information, please contact the WRAP Team at: wrap@warwick.ac.uk

warwick.ac.uk/lib-publications

THE UNIVERSITY OF
WARWICK

A Solid State Nuclear Magnetic Resonance Study of Industrial Inorganic Pigments

by

Nick Dajda

Thesis

Submitted to the University of Warwick

for the degree of

Doctor of Philosophy

Department of Physics

October 2002

This thesis is dedicated
to my family.

Contents

List of Tables

List of Figures

Acknowledgments

I would like to thank Mark Smith for supervising my PhD studies, for providing continued support and enthusiasm, and always being available for discussions.

Thanks also to Nick Carthey and Peter Bishop at Johnson Matthey, without which there could be no NMR investigation into ceramic pigments. Their commitment to the project through organising extended visits to their research labs, and regular meet-ups ensured the PhD ran very smoothly. Thanks also to Jon Booth for assistance synthesising the silver pigments.

In the NMR laboratory, I would like express my gratitude to Andy Howes and Ian Poplett for teaching me the finer points of NMR experimentation. Thanks also goes to Ray Dupree, Allan Baldwin, Dan Padro, Kevin Pike, Geoff West and Philips Gunawidjaja for their support.

Finally, special thanks to my family, for giving their complete backing to my PhD studies, and to Nafeesa.

Declarations

The work for this thesis was carried out in the Department of Physics at the University of Warwick from October 1999 to September 2002. This thesis is the result of my own independant research except where referenced, and has not been previously submitted for any other degree.

Some of the results of chapters 4 and 5 have already been accepted for publication:

N. Dajda, N. Carthey, P. T. Bishop, J. Dixon and M. E. Smith, Atomic Site Preferences and Structural Evolution in Vanadium-Doped $ZrSiO_4$ from Multinuclear Solid State NMR, *Physical Review B*, Accepted December 2002.

It is anticipated that other parts of this thesis will be submitted for publication in the future.

Nick Dajda

Abstract

Nuclear magnetic resonance has been used to look at a number of colourful ceramic pigment systems, most of which are sold commercially in large quantities.

Doped zircon ($ZrSiO_4$) pigments were examined using ^{19}F, ^{23}Na, ^{29}Si, ^{51}V and ^{91}Zr NMR. In these systems, paramagnetic species are incorporated into the sample in small quantities creating the colourful pigment. The impurity dopants in the systems studied either dope directly into lattice sites in the zircon, or form an extra chemical phase. NMR was able to distinguish between these two doping mechanisms in a number of doped zircon pigments.

Most spectra showed effects which were due to the magnetic influence of paramagnetic colouring species, and the strength of the interaction depended on the magnetic moment of the ion containing the unpaired electron. In the case of vanadium doped zircon, the moment was small enough that it allowed extra contact shifted peaks to be resolved in the spectra which indicated that the V^{4+} colouring ion probably substitutes into both the tetrahedral SiO_4 site, and at the dodecahedral ZrO_8 site. This is of current interest, and many other spectroscopic and computational experiments have also been performed to elucidate which of the two sites V^{4+} is located at. A ^{17}O-enriched zircon sample was also synthesised through a sol-gel route, and the local environment at the oxygen sites was followed through zircon formation from the TEOS and Zr-isopropoxide precursors.

A multinuclear approach looking at the ^{11}B, ^{23}Na, ^{27}Al and ^{29}Si isotopes within silver containing glasses was able to provide information about the coordination of the isotopes within the glasses. ^{109}Ag NMR was evaluated as an experimental technique for examining silver containing compounds.

^{119}Sn NMR was used to quantify the amount of Sn(II) and Sn(IV) in orange

coloured SnO-ZnO-TiO_2 (TZT) produced pigments, and the colour of the sample was found to correlate with the width of the Sn(IV) peak. The level of Na_2CO_3-loading in yellow coloured TZT pigments also influenced the Sn(IV) linewidth, indicating that Sn(IV) is likely to be responsible for the perceived colour of the pigment. ^{17}O-enriched SnO_2 was also synthesised, and the ^{17}O and ^{119}Sn spectra allowed a measure of the crystallinity of the sample to be determined as it was successively heated to higher temperatures.

Abbreviations

DB	Double bearing
DD	Double drive
CP	Cross polarisation
CSA	Chemical shift anisotropy
CYCLOPS	Cyclically ordered phase sequence
DAS	Dynamic angle spinning
DOR	Double rotation
DTA	Differential thermal analysis
EFG	Electric field gradient
EPR	Electron paramagnetic resonance
ESR	Electron spin resonance
EXAFS	Extended X-ray absorption fine structure
FID	Free induction decay
FT	Fourier Transform
MAS	Magic angle spinning
MQMAS	Multiple quantum magic angle spinning
NMR	Nuclear magnetic resonance

NQR Nuclear quadrupole resonance

PAC Perturbed angular correlations

PAS Principle axis system

QCPMG Quadrupolar Carr-Purcell Meiboon Gill

REDOR Rotational echo double resonance

TEM Transmission electron microscopy

TEOS Tetraethylorthosilane

TOSS Total supression of spinning sidebands

TZT Tin-zinc-titanium

XANES X-ray absorption near edge structure

XAS X-ray absorption spectroscopy

XPS X-ray photoelectron spectroscopy

XRD X-ray diffraction

Chapter 1

Introduction

The aim of this thesis is to apply solid state Nuclear Magnetic Resonance (NMR) to probe the local environments in several pigment systems produced commercially by Johnson Matthey, and to find out more about their atomic scale structure.

Colourful ceramic pigments are usually produced by mixing an oxide colour source with other oxides to encapsulate the colour. This is then fired at temperatures ranging from ~500-1500°C[1]. A wide variety of pigments can be synthesised by using different colour sources, for example, different blue coloured pigments are produced commercially using cobalt, aluminium, vanadium and copper oxides as colourants. These pigments are then either mixed with a ceramic glaze and used as a finish for clay-based tiles and sanitaryware, or can be mixed with a plasticizer which can be used to create colourful plastic products. When added to a glaze, the pigment needs to be chemically stable up to the glaze's glass forming temperature, which is usually at least 1000°C[2, 3].

There is a large range of chemically complex pigment and glaze systems currently retailed. A large proportion of pigments currently on the market have been developed more than 50 years ago, yet are still not fully understood. This is despite the often very broad range of analytical techniques which have been applied to investigate them.

NMR is a spectroscopic technique which provides information about the local environment of probe nuclei within a sample[4]. It is site and element specific and so can be used to look at dilute nuclei within a sample, without having to be concerned with the signal from all other nuclei within the sample. This means it is a suitable technique for providing new information about the local environment within ceramic pigments. If

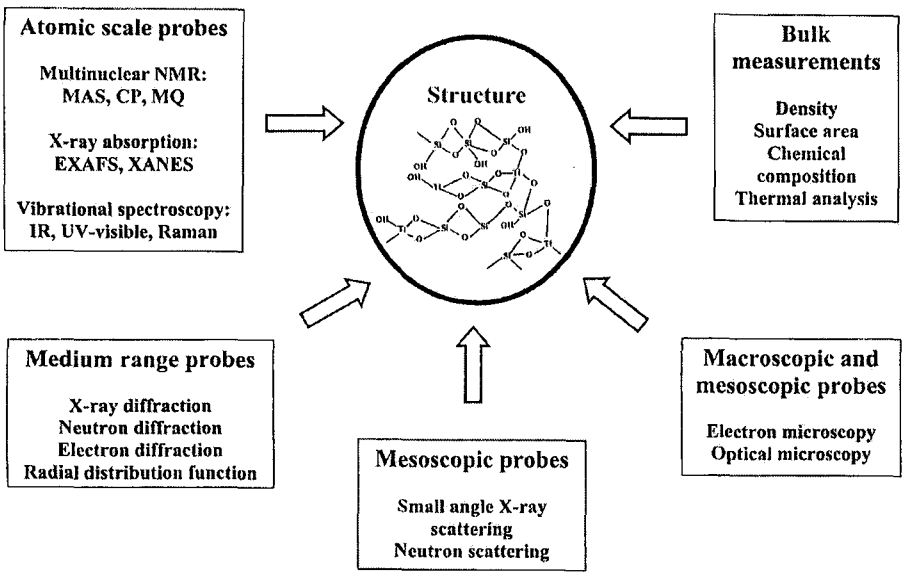

Figure 1.1: Relationship between the various methods for investigating the structures of materials[5].

the colour of a sample is due to a specific element within it, NMR can also potentially be used to investigate the local environment at this site giving rise to the colour.

NMR does not require any medium range order within a sample, so unlike routine X-ray techniques, NMR is very well suited to the study of non-crystalline compounds, and those which exhibit atomic disorder. Although spectra are only acquired here on solid state samples, NMR is also routine tool for molecular structure determination in solution samples, and is also widely used for non-invasive imaging with industrial and medical applications.

A wide range of techniques can be used to characterise materials, ranging in length scale from bulk measurements to atomic scale probes. Figure 1.1 shows the relationship between these different scales[5]. To gain the greatest insight into a material, it is important to investigate it using many different length-scale techniques. Solid state NMR is still a little used technique for investigating the atomic scale, however it is very useful for providing data to complement information from other techniques.

NMR is a well established technique, and one of the first resonance experiments was performed by Cleeton and Williams in 1934 where a microwave spectrometer was used to look at the inversion spectrum of ammonia molecules[6]. NMR was formally recognised as

a method of measuring the nuclear magnetic moment in 1946, and was observed independently by Bloch[7, 8] and Purcell[9]. Despite being a relatively old technique, NMR is still developing. There have been a number of milestones in NMR development which have led to increasing interest in the technique[10]. Early NMR experiments used a continuous frequency sweep to excite and measure nuclear transitions, however the implementation of Fourier Transform NMR spectroscopy by Ernst in 1966 led to a typical tenfold increase in sensitivity[11]. It also led to the invention of more complex multiple pulse and two-dimensional experiments. The advent of cryogenically cooled high magnetic field superconducting magnets also enabled routine high-field NMR to become a reality. One advantage of higher magnetic fields is that resolution is increased for a large proportion of systems. Second-order quadrupolar-broadened lineshapes will be narrowed at higher fields, and isotopes with low intrinsic magnetic moments will resonate at higher frequencies, often making these isotopes more amenable to NMR study. Higher magnetic fields also create more intense NMR signals since a larger population difference between nuclear spin states is induced. Magic angle spinning (MAS) has also enabled higher resolution spectra to be acquired for solid state NMR systems where resonance lines are broadened by the CSA and dipolar interactions[12]. This is now a routine technique with spinning speeds of 25 kHz being easily attainable.

Continued technique development in NMR also leads to a broader range of potential applications. For example, the recent multiple quantum magic angle spinning (MQMAS) technique can provide increased resolution in solid state spectra which are dominated by the second-order quadrupolar interaction[13].

1.1 Structure of thesis

The remainder of this work has been divided into six chapters. Chapter 2, Theory covers the physical description of the main interaction mechanisms that govern the NMR spectra acquired.

Chapter 3, Experimental outlines the main components of an NMR experiment, and the pulse sequences used to manipulate the sample's magnetisation. The properties of the isotopes studied are briefly discussed, and the sample preparation procedure employed

for manufacturing the different pigment systems is also described.

The doped zircon ($ZrSiO_4$) pigment system was investigated thoroughly and has been split into two chapters. Chapter 4, Doped zircon pigments examines zircon which has been doped with Pr, Fe, Nb, Mn and Cd. Synthetic and naturally occurring zircons are also examined in this chapter. Chapter 5 covers zircon which has been doped with vanadium, since the influence of paramagnetic V^{4+} in this system provides some additional interesting structural information. A novel, ^{17}O-enriched zircon is also synthesised so that the ^{17}O local environment can be examined before and after sample firing.

Chapter 6 initially examines a number of simple silver-containing compounds using ^{109}Ag NMR, and then extends this approach to investigate silver-containing glass pigments. This is complemented by a multinuclear NMR study covering other NMR active isotopes within these glasses.

Chapter 7 covers the SnO-ZnO-TiO_2 (TZT) pigment system. The effect of firing temperature is investigated using ^{119}Sn NMR and is compared to ^{119}Sn Mössbauer spectra acquired on the same samples. TZT pigments which have been doped with Na_2CO_3 to give a different colour are also examined using ^{23}Na and ^{119}Sn NMR. Finally, a ^{17}O-enriched sample of SnO_2 is synthesised using a sol-gel route. A multinuclear NMR approach is then employed to investigate the effect of different heat treatments on the microstructure of the sample.

References

[1] H. M. Smith, *High Performance Pigments*, Wiley-VCH, Germany (2002).

[2] P. A. Lewis, *Pigment Handbook, Vol 1*, Wiley, USA (1988).

[3] G. Buxbaum, *Industrial Inorganic Pigments, Second edition*, Bayer AG, Germany (1998).

[4] H. Eckert, Structural characterisation of noncrystalline solids and glasses using solid state NMR, *Progress in NMR Spectroscopy*, **24** 159 (1992).

[5] K. J. D. MacKenzie and M. E. Smith, *Multinuclear Solid-state NMR of Inorganic Materials*, Pergamon, Amsterdam, 2002.

[6] C. E. Cleeton and N. H. Williams, Electromagnetic waves of 1.1 cm wave-length and the absorption spectrum of ammonia, *Physical Review*, **45** 234 (1934).

[7] F. Bloch, Nuclear induction, *Physical Review*, **70** 460 (1946).

[8] F. Bloch, W. W. Hansen and M. Packard, The nuclear induction experiment, *Physical Review*, **70** 474 (1946).

[9] E. M. Purcell, H. C. Torrey and R. V. Pound, Resonance absorption by nuclear magnetic moments in a solid, *Physical Review*, **69** 37 (1946).

[10] J. W. Emsley and J. Feeney, Milestones in the first fifty years of NMR, *Progress in Nuclear Magnetic Resonance Spectroscopy*, **28** 1 (1995).

[11] R. Ernst and W. Anderson, Application of fourier transform spectroscopy to magnetic resonance, *Review of Scientific Instruments*, **37** 93 (1966).

[12] E. R. Andrew, A. Bradbury and R. G. Eades, Removal of dipolar broadening of nuclear magnetic resonance spectra of solids by specimen rotation, *Nature*, **183** 1802 (1959).

[13] L. Frydman and J. S. Harwood, Isotropic spectra of half-integer quadrupolar spins from bidimensional magic-angle spinning NMR, *Journal of the American Chemical Society*, **117** 5367 (1995).

Chapter 2

Theory

2.1 NMR Phenomena

If a nucleus has an odd mass number, it will possess a half-integral nuclear spin I. Nuclei with an even mass number and an odd charge number will have an integral nuclear spin. Most elements in the Periodic Table have an isotope which satisfies one of these conditions, and can potentially be probed using NMR[1-4]. The magnetic moment of the nucleus can be in any one of $2I + 1$ states and is given by

$$\mu = \gamma \hbar m_I \tag{2.1}$$

where m_I is the quantum number of the spin state, $m_I = -I, -I+1, \ldots, I-1, I$ and γ is the gyromagnetic ratio of the nucleus.

When this nucleus is placed in a magnetic field $\boldsymbol{B}$ (in the z direction here) it will have an energy

$$U = -\boldsymbol{\mu} \cdot \boldsymbol{B} = -\mu_z B \tag{2.2}$$

and since the magnetic dipole moment of the nucleus is dependent on the spin state m_I, it will now have a number of energy states it can exist in. Figure 2.1 shows the splitting of nuclear magnetic energy levels for a spin $I = \frac{1}{2}$ nucleus when placed within a magnetic field. From equation 2.1, each state will have an energy $U = -\gamma \hbar m_I B$. The selection rule for nuclear magnetic transitions is $\Delta m_I = \pm 1$, so the energy difference for a $\frac{1}{2} \rightarrow -\frac{1}{2}$ dipole transition is

$$E = \gamma \hbar B \tag{2.3}$$

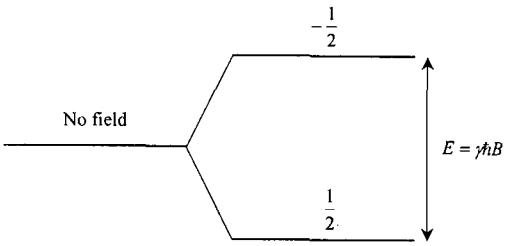

Figure 2.1: The effect of applying a magnetic field to a nucleus with spin $I = \frac{1}{2}$.

This is how the gyromagnetic ratio is defined since from a classical point of view, ω_0 is the frequency at which a magnetic dipole of moment $\mu = \gamma\hbar$ would precess as if it were orthogonal to the applied magnetic field. For the rest of this section it is convenient to think about the net magnetisation of the system as a vector $\boldsymbol{M}$ which will align along the z-direction of the field at thermal equilibrium.

If a second field B_1 is applied in the x-direction, and oscillates at an angular frequency ω_0, the magnetisation will precess in the y-z plane towards $-y$ at an angular frequency (from equation 2.3) $\omega_1 = \gamma B_1$. If the field is only applied for a time τ, the magnetisation will have precessed an angle θ about the x-axis:

$$\theta = \omega_1 \tau = \gamma B_1 \tau \tag{2.4}$$

so if $\theta = \frac{\pi}{2}$, this pulse will rotate the magnetisation from pointing along the z-axis to lying along the $-y$-axis. This magnetisation will then precess in the x-y plane at an angular frequency ω_0, and it is this precession that is measured during the NMR experiment, since this oscillating magnetisation induces a voltage in the detection coil through Faraday's induction effect.

The Fourier transform of the square wave pulse takes the form $\sin\tau/\tau$, so the envelope of magnetic energy level splittings excited will be a $\sin\tau/\tau$ function which is plotted in figure 2.2. This typically means that if a spectrum is to be acquired over a 200 kHz frequency range, the longest pulse length used would be about $1/(2\times10^5) = 5\ \mu$s. If a longer pulse were used, the heights of any resonances far from the carrier frequency would start to be attenuated by the $\sin\tau/\tau$ envelope, since they were not excited to the same extent as resonances closer to the carrier frequency of the pulse.

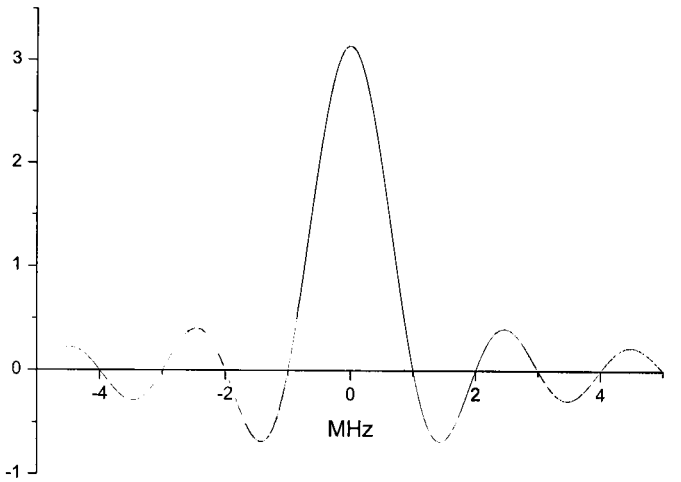

Figure 2.2: The RF radiation envelope created by a 5 μs pulse. The x-axis is MHz from the carrier frequency of the pulse.

2.1.1 The Bloch Equations

The Bloch equations describe what happens to the precessing magnetisation immediately after the 90° pulse. Bloch used a coordinate system that rotated in the x-y plane at the same frequency as the precession ω_0. In this rotating frame, the decay of magnetisation can be described by

$$\frac{dM_z}{dt} = \gamma \left(\boldsymbol{M} \times \boldsymbol{B}\right)_Z + \frac{M_0 - M_z}{T_1} \tag{2.5}$$

$$\frac{dM_x}{dt} = \gamma \left(\boldsymbol{M} \times \boldsymbol{B}\right)_X - \frac{M_x}{T_2} \qquad \frac{dM_y}{dt} = \gamma \left(\boldsymbol{M} \times \boldsymbol{B}\right)_Y - \frac{M_y}{T_2} \tag{2.6}$$

In equation 2.5, the z component of the magnetisation increases exponentially to a value of M_0 aligned along the applied field. The time taken to return to equilibrium is characterised by the spin-lattice relaxation time T_1:

$$M_z(t) = M_0 \left(1 - \exp\left(\frac{-t}{T_1}\right)\right) \tag{2.7}$$

so after a 90° pulse it takes a time of approximately $4T_1$ for the magnetisation to fully relax back along the field. There are a number of mechanisms that can aid T_1 relaxation which will be outlined in section 2.4. For a sample with a short T_1, more acquisitions can be acquired in a time period than for a sample with a long T_1, so more signal can

be measured. Care needs to be taken with a sample with a range of T_1s. If the recycle time used is not $4T_1$ of the longest relaxing species, the shorter T_1 species will give a disproportionately larger signal than the long T_1 species, since the long T_1 species will have been partially saturated. Quantitative comparisons between the two species cannot then be derived from spectra under conditions of partial saturation.

The component of magnetisation precessing in the x-y plane decays exponentially as the individual spins dephase. This is described by the spin-spin relaxation time constant T_2:

$$M_x(t) = M_{x,t=0} \exp\left(\frac{-t}{T_2^*}\right) \quad \text{where} \quad \frac{1}{T_2^*} = \frac{1}{T_2} + \frac{\gamma \Delta B}{2\pi} \tag{2.8}$$

where T_2^* is the effective T_2 relaxation which is responsible for the exponential decay envelope in the free induction decay of a Lorentzian line. This has extra broadening due to magnetic field inhomogeneities ΔB. In most of the solid state NMR spectra presented in this work, $\gamma \Delta B << T_2^{-1}$ and so $T_2^* = T_2$.

2.2 Interaction Mechanisms

The Hamiltonian governing the energy of a nuclear spin can be split up into many separate effects:

$$H = H_Z + H_{RF} + H_{CS} + H_D + H_Q + H_H + \ldots \tag{2.9}$$

where H_Z is the Zeeman interaction which describes the removal of the degeneracy in the magnetic energy levels by the applied magnetic field (see equation 2.2), and H_{RF} is the radio frequency pulse which excites transitions between the different nuclear magnetic energy levels. The remaining interactions are described in the following sections, and are the most dominant for the solid state systems examined here.

2.2.1 Chemical shift

The chemical shift interaction is caused by electrons surrounding the nucleus trying to oppose the applied magnetic field and shield the nucleus. Two mechanisms affect the amount of shielding experienced by the nucleus. The diamagnetic contribution to the shielding is due to the electrons opposing the magnetic field and so reducing the field at the nucleus. The paramagnetic contribution is caused by the applied field mixing excited

electrons which have paramagnetic properties with the ground state. Since the ground state now has a paramagnetic component, the field experienced will be increased.

The screening is orientation dependant and needs to be described by a second rank tensor $\boldsymbol{\sigma}$. The interaction Hamiltonian is

$$H_{CS} = -\gamma \boldsymbol{I} \cdot \boldsymbol{\sigma} \cdot \boldsymbol{B} \tag{2.10}$$

and $\boldsymbol{\sigma}$ is most simply described in a frame where only diagonal elements of the tensor are present. This is the principle axis system (PAS). The chemical shift interaction can then be described through the three diagonal elements δ_{xx}, δ_{yy} and δ_{zz} which are a measure of the amount of deshielding experienced by the nucleus:

$$\boldsymbol{\sigma_{pas}} = \begin{pmatrix} \sigma_{xx} & 0 & 0 \\ 0 & \sigma_{yy} & 0 \\ 0 & 0 & \sigma_{zz} \end{pmatrix} = \begin{pmatrix} 1-\delta_{xx} & 0 & 0 \\ 0 & 1-\delta_{yy} & 0 \\ 0 & 0 & 1-\delta_{zz} \end{pmatrix} \tag{2.11}$$

Chemical shift interaction measurements are usually reported using three quantities derived from the three components in the PAS[5]

$$\delta_{iso} = \frac{1}{3}\left(\delta_{xx} + \delta_{yy} + \delta_{zz}\right), \quad \delta_{aniso} = \frac{3}{2}\left(\delta_{zz} - \delta_{iso}\right), \quad \eta_{cs} = \frac{3\left(\delta_{xx} - \delta_{yy}\right)}{2\delta_{aniso}} \tag{2.12}$$

where δ_{iso} is the isotropic position of the line, δ_{aniso} is a measure of the anisotropic component of the interaction that gives rise to the static linewidth, and η_{cs} is the asymmetry factor. η_{cs} is the departure of the symmetry at the site from axial symmetry where $\eta_{cs} = 0$ to centrosymmetry where $\eta_{cs} = 1$.

For a crystallite at angles θ and ϕ to B_0, the contribution to the lineshape is then given by a shift of

$$\delta = \delta_{iso} + \frac{\delta_{aniso}}{2}\left(3\cos^2\theta - 1 + \eta\sin^2\theta\cos 2\phi\right) \tag{2.13}$$

and the whole static lineshape for a powder will be made up from weighted contributions from crystallites ranging over all θ and ϕ. Figure 2.3 shows example compound static powder lineshapes created for three different values of η.

Another more recent convention is also used for relating the CSA tensor elements to the powder spectrum[6]:

$$\delta_{iso} = \frac{1}{3}\left(\delta_{11} + \delta_{22} + \delta_{33}\right), \quad \Omega = \delta_{11} - \delta_{33}, \quad \kappa = \frac{3(\delta_{22} - \delta_{iso})}{(\delta_{11} - \delta_{33})} \tag{2.14}$$

where δ_{xx}, δ_{yy} and δ_{zz} have been sorted into δ_{11}, δ_{22} and δ_{33} where $\delta_{11} \geq \delta_{22} \geq \delta_{33}$. The chemical shift δ_{iso} is then still the same as used in equation 2.12. The main advantage of these units is that the span, Ω is the actual width of the powder pattern. The skew, κ is similar to the asymmetry parameter η_{cs} (figure 2.3) except it varies from -1 to 1, negating the need to use a negative value of Ω to describe an oblate axial shift tensor.

The isotropic chemical shift δ_{iso} is usually reported in units of parts per million (ppm):

$$\delta_{iso}(\text{ppm}) = 10^6 \frac{\delta_{iso}(\text{Hz}) - \delta_r(\text{Hz})}{\delta_r(\text{Hz})} \tag{2.15}$$

where δ_r is the frequency of a suitable reference compound for the nucleus under investigation. The first advantage of measuring a resonance frequency with respect to a reference compound is the same peak position will be measured independent of magnetic field drift and shimming, provided the reference is measured under the same shimming conditions and probe orientation, and at a similar time to the main experiment. The second useful property is that as long as there are no field dependent effects contributing to δ_{iso} (primarily the quadrupolar interaction), then the same ppm value will be measured for δ_{iso} regardless of the field employed.

2.2.2 Dipolar coupling

The magnetic moments of neighbouring nuclei coupling together can broaden a lineshape. This coupling can be transmitted through polarisation of bonding electrons (J-coupling), although this effect is usually not important in solid state NMR. The coupling can also be a through space interaction, and equation 2.16 gives the Hamiltonian for two interacting spins a distance r apart with gyromagnetic ratios γ_1 and γ_2:

$$\begin{aligned}
\boldsymbol{H}_d &= \frac{\gamma_1\gamma_2\hbar^2}{r^3}\left(A+B+C+D+E+F\right)\frac{\mu_0}{4\pi} \\
A &= -\boldsymbol{I}_{1z}\boldsymbol{I}_{2z}\left(3\cos^2\theta - 1\right) \\
B &= \tfrac{1}{4}\left[\boldsymbol{I}_{1+}\boldsymbol{I}_{2-} + \boldsymbol{I}_{2+}\boldsymbol{I}_{1-}\right]\left(3\cos^2\theta - 1\right) \\
C &= -\tfrac{3}{2}\left[\boldsymbol{I}_{1z}\boldsymbol{I}_{2+} + \boldsymbol{I}_{1+}\boldsymbol{I}_{2z}\right]\sin\theta\cos\theta\exp(-i\phi) \\
D &= -\tfrac{3}{2}\left[\boldsymbol{I}_{1z}\boldsymbol{I}_{2-} + \boldsymbol{I}_{1-}\boldsymbol{I}_{2z}\right]\sin\theta\cos\theta\exp(i\phi) \\
E &= -\tfrac{3}{4}\boldsymbol{I}_{1+}\boldsymbol{I}_{2+}\sin^2\theta\exp(-2i\phi) \\
F &= -\tfrac{3}{4}\boldsymbol{I}_{1-}\boldsymbol{I}_{2-}\sin^2\theta\exp(2i\phi)
\end{aligned} \tag{2.16}$$

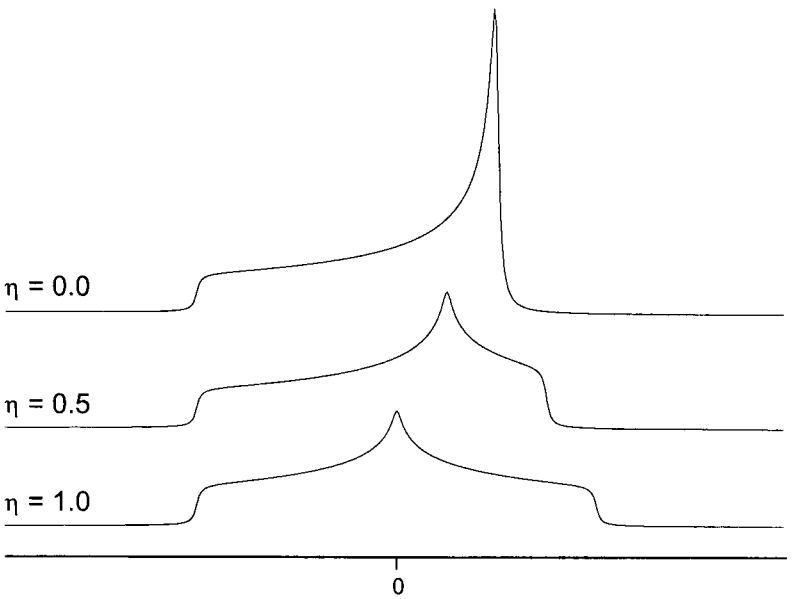

Figure 2.3: Simulated static CSA lineshapes. δ_{iso} and δ_{aniso} are the same for all lines, however η_{cs} has been simulated between 0.0 and 1.0.

Terms C to F are non-energy conserving and so require energy exchange between the two spins and the rest of the system. This is a means of T_1 relaxation, however during the timescale of a FID, these terms are small compared to the energy conserving terms A and B, so the Hamiltonian is usually truncated by omitting terms C to F leaving only the secular terms A and B.

Term A is the classical interaction of the coupling of two magnetic moments, and term B is a *flip-flop* term describing the transition of the spins between spin-states. When the two spins coupling together are not the same species, $\gamma_1 \neq \gamma_2$, and so the energy difference between spin states will be different for both species. Term B is now no longer energy conserving and will have less of an effect on the total Hamiltonian since additional interactions are required with the bulk system to conserve energy. This typically causes the linewidth of a heteronuclear coupled system to be smaller than the width for a homonuclear coupled system, where term B is energy conserving (providing the dipolar term is the dominant interaction in the two systems being compared).

The interaction also has applications in distance measurement between spins, since

the dipolar coupling $D = \mu_0\gamma_1\gamma_2\hbar^2/4\pi r^3$ has an r^{-3} dependence. A variety of pulse sequences exist for measuring D, for example REDOR[7].

2.2.3 Quadrupolar coupling

An electric field gradient is usually present at most sites in a sample, unless the local symmetry at the site is cubic and the electric field contribution from all neighbouring point charges is cancelled out. The gradient can be described by a second rank tensor $\boldsymbol{q}$ which in its principle axis frame consists of three components, $V_{xx} \leq V_{yy} \leq V_{zz}$.

For NMR nuclei with $I > \frac{1}{2}$, the electrical charge distribution about the nucleus is non-spherical. This gives these nuclei a quadrupole moment which couples with any electric field gradient present. Although this is an electrical interaction, there is a dependence on the magnetic quantum number m, hence this allows the electric field gradient to be measured through its influence on the magnetic energy levels of the probe nucleus. The interaction Hamiltonian is[8-10]

$$H_Q = \frac{eQ}{6I(2I-1)\hbar}\boldsymbol{I}\cdot e\boldsymbol{q}\cdot\boldsymbol{I} \tag{2.17}$$

Expanding the tensor components of $\boldsymbol{q}$, and for simplicity assuming the site has axial symmetry ($\eta_Q = 0$), the Hamiltonian becomes:

$$H_Q = \frac{e^2qQ}{4I(2I-1)\hbar}\left\{\frac{1}{2}(3\cos^2\theta-1)(3I_z^2-I^2)+\frac{3}{4}\sin^2\theta(I_+^2+I_-^2)\right. \\ \left.+\frac{3}{2}\sin\theta\cos\theta\left[I_Z\left(I_+ + I_-\right)+\left(I_+ + I_-\right)I_Z\right]\right\} \tag{2.18}$$

By performing a perturbation expansion, the effect of the interaction on the magnetic energy levels can be calculated. Only the first and second order frequency perturbations $\nu^{(1)}$ and $\nu^{(2)}$ are considered here since the nuclear quadrupole resonance (NQR) technique is better suited to situations where the quadrupolar coupling is so large that the H_Q can no longer be treated as a small perturbation. The first order perturbation is:

$$\nu^{(1)}(m) = \frac{3C_Q}{4I(2I-1)}\left(3\cos^2\theta-1\right)\left(m-\frac{1}{2}\right) \tag{2.19}$$

where $C_Q = (e^2qQ)/h$ is the quadrupolar coupling constant, and m is the magnetic quantum number[11]. From figure 2.4 it can be seen that all the energy levels are modified to first order. Both the $m = \pm\frac{1}{2}$ levels are perturbed by the same amount, so there is no

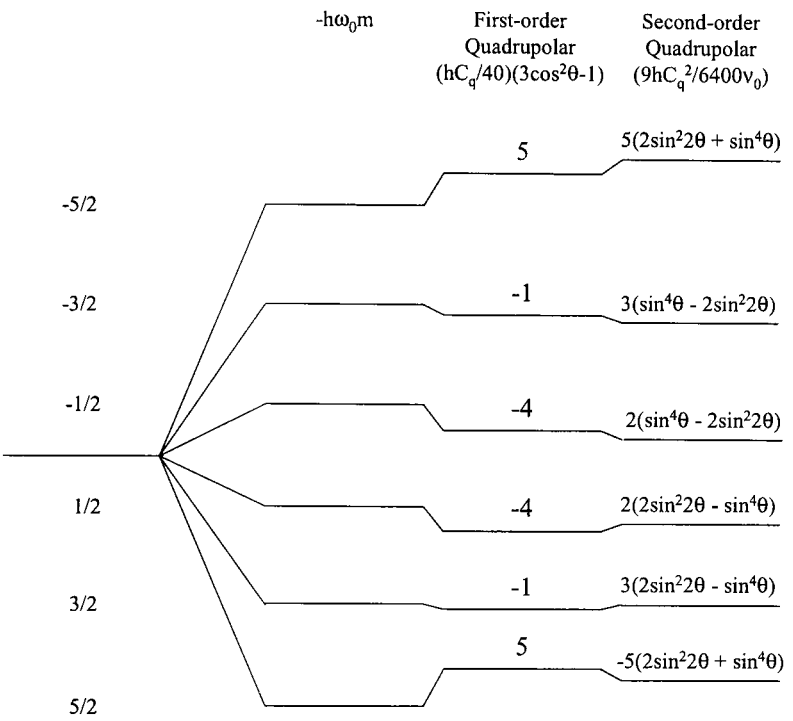

Figure 2.4: Energy level diagram for a spin $\frac{5}{2}$ nucleus[11].

net shift in the resonance frequency of the $\frac{1}{2} \rightarrow -\frac{1}{2}$ transition since the difference between levels is unchanged to first order. The remaining transitions are shifted either side of the central transition's resonance.

To second order, the frequency of the central transition is further shifted by

$$\nu_Q^{(2)}(m) = \frac{-9}{64}\frac{C_Q^2}{\nu_0 I^2(2I-1)^2}\left(a - \frac{3}{4}\right)(1-\cos^2\theta)(9\cos^2\theta - 1) \qquad (2.20)$$

where $a = I(I+1)$. The frequency of the central resonance is now shifted from its isotropic position, and this shift is dependant on $1/\nu_0$ so at higher applied fields, the quadrupolar induced lineshift and the second order quadrupolar line broadening will be reduced. The dependence of the position of a line $\delta(B_0)$ with field allows C_Q to be measured if η_Q is known (see section 5.6).

Figure 2.5 shows some second order quadrupolar central transition lineshapes when the sample is static, and when the sample is spinning infinitely fast. η_Q values of 0.0, 0.5 and 1.0 have been simulated, and it can be seen that spinning the sample reduces the

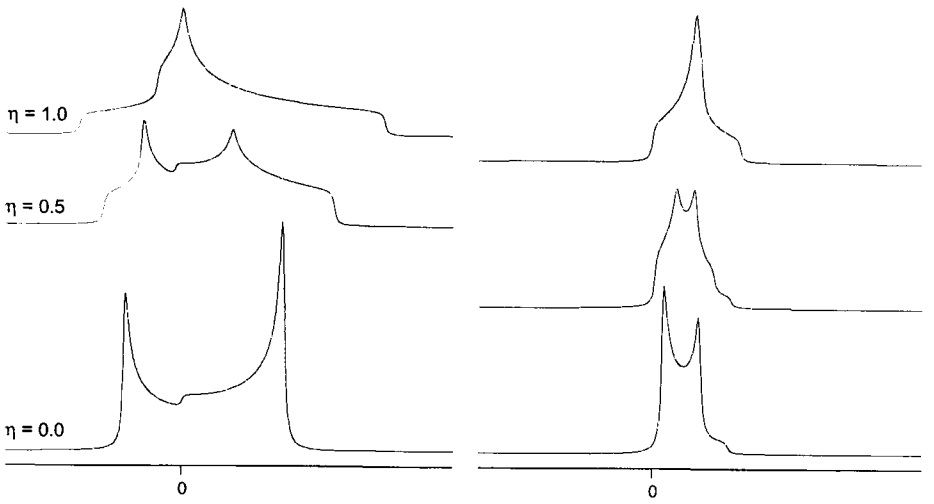

Figure 2.5: Simulated second order quadrupolar central transition lineshapes. The x-axis scaling is the same for both the static lineshapes (left) and MAS lineshapes (right). C_Q and δ_{iso} are also identical for all lineshapes, however a range of values of η_Q have been simulated. 0 on this scale corresponds to the isotropic chemical shift.

linewidth by a factor of $\sim 3-4$. When spinning, all of the lineshape is to more negative ppm of the isotropic line position δ_{iso}.

2.2.4 Hyperfine interactions

When a probe nucleus in a solid is close to an ion which exhibits electronic paramagnetism, the field experienced by the probe nucleus will be influenced by the unpaired electron of the paramagnetic nucleus through the hyperfine interaction. This can be written in general form [12, 13]

$$H_H = \left(\frac{\gamma_n}{2\pi}\right) \boldsymbol{A}_n \cdot \boldsymbol{I} = \left(\frac{\gamma_n}{2\pi}\right) (\boldsymbol{A}_f + \boldsymbol{A}_d + \boldsymbol{A}_l)\, I_z \boldsymbol{h}_0 \tag{2.21}$$

where $\boldsymbol{A}_f$, $\boldsymbol{A}_d$ and $\boldsymbol{A}_l$ are operators representing the Fermi contact, dipolar and nuclear-electron orbital interactions. I_z is the component of $\boldsymbol{I}$ along the magnetic field, and $\boldsymbol{h}_0$ is a unit vector along the field. For the shift to be observable, the electron spin relaxation rate $1/T_{1e}$ needs to be greater than the nuclear-electron hyperfine interaction so that the nuclear spin is only being influenced by the average electron spin. If they are both of similar frequency, the oscillation of the electron spin is slow enough that it has a much

more efficient coupling with the nuclear spin. This leads to broadening of the resonance and in solution NMR can lead to two lines, one for each electron spin state.

The Fermi contact interaction is a through bond effect. The unpaired electron spin density from the paramagnet is transferred to the probe nucleus via occupation of the s-orbital[14] which causes a shift of the resonance. As the number of bonds separating the probe and paramagnetic nuclei increases, the shift will decrease. The operator describing this part of the interaction is

$$\boldsymbol{A}_f = \frac{8\pi}{3} g_e \mu_b \sum_i \delta(r_i) \boldsymbol{s}_i \tag{2.22}$$

where g_e is the free electron g factor, μ_b is the Bohr magneton, $\boldsymbol{r}_i$ is the vector between the probe nucleus and electron i, and $\boldsymbol{s}_i$ is the spin momentum of electron i. The summation over all nearby unpaired electrons shows that the interaction is additive. This has been observed in ^{119}Sn MAS spectra of rare-earth stannates where extra contact-shifted lines were observed due to paramagnetic Sm^{3+} substituting for Y^{3+}[15]. The magnitude of the shift was dependant on the number of Sm^{3+} substituting into the local environment, and the integrals of the peaks could be used to calculate the distribution of Sm^{3+} within the structure.

Equation 2.22 can be simplified by treating the summation over nearby electron spins as the thermally averaged electron spin value $\langle S_z \rangle$[16], so the Hamiltonian for just the Fermi contact shift is

$$H_f = \left(\frac{\gamma}{2\pi}\right) I_z \boldsymbol{A_f} \cdot \boldsymbol{h_0} = \left(\frac{4\gamma}{3} g_e \mu_b\right) I_z \sum_i \delta(r_i) \boldsymbol{s}_i \cdot \boldsymbol{h_0} = A_f I_z \langle S_z \rangle \tag{2.23}$$

where A_f is the hyperfine coupling constant. Since $\langle S_z \rangle$ is proportional to χB_0, the shift will vary with temperature in the same way the magnetic susceptibility χ does. Both the Fermi contact and dipolar hyperfine interactions vary linearly with $\boldsymbol{s}_i$ (equations 2.22 and 2.24), so the temperature dependence of the shifts cannot be used directly to distinguish between the two interactions. However, it can be used to investigate χ when only one interaction is dominant, and it can (along with T_1 measurements) be used to identify a resonance that is shifted through a hyperfine interaction. The temperature dependence of the Fermi contact interaction has been exploited in ^{119}Sn MAS NMR of $Pr_2Sn_2O_7$[17]. At room temperature, the chemical shift was found to vary by 14 ppm when the temperature changed by 1 K due to the contact interaction between the Pr and Sn.

The dipolar coupling interaction present here is similar to the classic dipolar coupling interaction presented in section 2.2.2. Here it is not between two nuclear magnetic moments, it is between the electronic magnetic moment and the magnetic moment of the probe nucleus, and is given by

$$\boldsymbol{A}_d = g_e \mu_b \sum_i \left[3 \left(\boldsymbol{s}_i \cdot \boldsymbol{r}_i \right) \boldsymbol{r}_i - r_i^2 s_i \right] / r_i^5 \tag{2.24}$$

The anisotropic part of this interaction broadens the static resonance and enlarges the spinning sideband manifold for spinning samples. If the atomic susceptibility of the paramagnet $\chi_p = \mu_0 \mu_e / B_0$ is anisotropic, the interaction will cause a pseudocontact shift. When there is only one paramagnetic spin near the probe nucleus, this shift will usually be small compared to the manifold of spinning sidebands[18]. This dipolar term can also create efficient nuclear relaxation, and is discussed in section 2.4.1.

The nuclear-electric orbital interaction can be written as

$$\boldsymbol{A}_l = 2\mu_b \sum_i \frac{\boldsymbol{l}_i}{r_i^3} \tag{2.25}$$

where $\boldsymbol{l}_i$ is the orbital angular momentum operator for election i. The Fermi and dipolar interactions are usually large compared to this effect.

2.3 Magic Angle Spinning

When a sample is mechanically rotated within a magnetic field, a time dependant oscillation is added to the laboratory Hamiltonian, so

$$H_{\text{lab}}(t) = H + H^*(t) \tag{2.26}$$

The 'secular' part of the Hamiltonian for dipolar coupling between two spins (from equation 2.16) is dependant on a $(3\cos^2\theta - 1)$ term, where θ is the angle between the direction of the applied field and a vector connecting the two spins. If this two spin system is now spun about an axis at an angle α to the magnetic field, the $3\cos^2\theta - 1$ term can be rewritten as

$$3\cos^2\theta - 1 = \frac{1}{2}(3\cos^2\alpha - 1)(3\cos^2\beta - 1) + \frac{3}{2}\sin^2\alpha \sin^2\beta \cos 2\phi + \frac{3}{2}\sin 2\alpha \sin 2\beta \cos\phi \tag{2.27}$$

where β is the angle made by the vector joining the two coupled spins, and the axis of rotation. ϕ is the amount of rotation such that the velocity of rotation is $d\phi/dt$. If equation 2.27 is now averaged over one rotor cycle, the average can be written as

$$\overline{3\cos^2\theta - 1} = \frac{1}{2}(3\cos^2\alpha - 1)(3\cos^2\beta - 1) \tag{2.28}$$

so the average will be zero if α is chosen such that $3\cos^2\alpha - 1 = 0$. This value of α is called the Magic Angle since rotation about this angle at sufficient speed will remove the anisotropic part of the dipolar interaction, leaving a much narrower line. If the frequency of rotation is not larger than the static linewidth, the $H^*(t)$ term creates a series of rotational echos in the FID separated by the rotation period. These Fourier transform into a set of spinning sidebands spaced an integer number of rotation frequencies apart from the isotropic line. Their amplitude is usually comparable to the amplitude of the original static lineshape at that frequency. Spinning sidebands can complicate spectra since it is sometimes not obvious which line is actually the isotropic line, although this can be resolved by spinning at different speeds which can be seen in figure 7.4. The TOSS pulse sequence is one approach that can be employed to cancel out the rotational echos and remove the sidebands[19].

A $(3\cos^2\theta - 1)$ term is also present in the chemical shift interaction in equation 2.13, and in the first-order quadrupolar broadening in equation 2.19. Because of this, the anisotropic broadening created by these two interactions can also be removed through MAS. The second-order quadrupolar term in equation 2.20 has a different angular dependence, which requires the sample to be spun about a different axis to remove the anisotropic component of this interaction. Thus, when either CSA and dipolar, or second order quadrupolar broadening are the dominant interaction, an angle can always be chosen to spin about that will remove either of these broadening mechanisms. If CSA or dipolar, and quadrupolar broadening both contribute simultaneously, the sample has to be spun about two axes simultaneously to remove all anisotropic broadening. In practise, this double rotation (DOR) technique is technically challenging and two other methods can be used to increase resolution. Dynamic angle spinning (DAS) involves allowing the sample to evolve for a time τ at one angle, and then an echo is acquired at another angle[20]. This has been largely superseded by multiple quantum magic angle spinning (MQMAS) which allows the magnetisation to evolve in a different quantum coherence for

a time τ, before it is converted back to a single quantum coherence for observation[21]. Both these experiments are two dimensional since τ is incremented, and a spectrum with no anisotropic quadrupolar component can be created by projecting the second dimension of the spectra onto the y-axis. A more thorough explanation of magic angle spinning can be found in the article by Maricq and Waugh[22].

2.4 Relaxation Mechanisms

There are many mechanisms that contribute to T_1 and T_2 relaxation, and only a simple model using thermal fluctuations is presented here. T_1 and T_2 relaxation are caused by local fluctuations in the magnetic or electric field at the nucleus[9], and the change in local field from the average field $\overline{\boldsymbol{B}}$ due to a thermal fluctuation can be written as

$$\delta \boldsymbol{B} = \boldsymbol{B} - \overline{\boldsymbol{B}} \tag{2.29}$$

where $\boldsymbol{B}$ is the actual field experienced by the nucleus. The relaxation times due to these field fluctuations can be described by the correlation time τ_0 over which the spin system is influenced by the fluctuation[10]:

$$\frac{1}{T_1} = \gamma^2 \left(\overline{\delta B_x^2} + \overline{\delta B_y^2} \right) \frac{\tau_0}{1 + \omega_0^2 \tau_0^2} \tag{2.30}$$

$$\frac{1}{T_2} = \gamma^2 \left[\overline{\delta B_z^2} \tau_0 + \frac{1}{2} \left(\overline{\delta B_x^2} + \overline{\delta B_y^2} \right) \frac{\tau_0}{1 + \omega_0^2 \tau_0^2} \right] \tag{2.31}$$

From this result, when $\tau_0 = 1/\omega_0$ the frequency of the fluctuations is the same as the Larmor frequency, and T_1 will be at a minimum. This is because the fluctuation has the same energy as the difference between magnetic spin levels, and can efficiently stimulate transitions between levels. The fluctuations also cause transverse T_2 relaxation through changing the phase of precessing spins to reduce the net precessing magnetisation. It is interesting to note that only the transverse x and y components of the field fluctuation contribute to longitudinal T_1 relaxation, whilst both the longitudinal and transverse field of the fluctuation aids transverse T_2 relaxation.

T_1 relaxation can also be reduced through the interaction mechanisms mentioned in section 2.2. Of these, the quadrupolar interaction for a system with a large C_Q is an

efficient relaxation mechanism and can reduce T_1 to < 0.5 s, provided that fluctuations of the correct frequency are present.

The dipolar mechanism also aids T_1 relaxation, however its effect is typically much smaller than the quadrupolar and hyperfine interactions. For spin $\frac{1}{2}$ systems which rely on dipolar and thermal interactions for relaxation, T_1 times tend to be shorter for probe nuclei with higher dipole moments. This is why ^{109}Ag NMR systems usually have long T_1 times as $\gamma(^{109}\text{Ag}) = -1.25 \times 10^7$ rad T^{-1} s^{-1}, and ^{19}F species tend to have shorter T_1 times since $\gamma(^{19}\text{F}) = 25.181 \times 10^7$ rad T^{-1} s^{-1}.

2.4.1 Paramagnetic relaxation

The through space dipolar interaction between the magnetic moment of an unpaired electron and a nucleus can be a very efficient mechanism for nuclear relaxation. This interaction between a paramagnetic ion at a distance r from a nucleus will induce longitudinal nuclear relaxation at a rate [13]:

$$\frac{1}{T_1} = \frac{2}{5}\left(\frac{\mu_0}{4\pi}\right)^2 \frac{\gamma^2 g_e^2 \mu_B^2}{r^6} \langle S_z \rangle^2 \frac{3\tau_0}{1+\omega_0^2\tau_0^2} \tag{2.32}$$

where g_e is the electron g-factor. The relaxation time T_1 is then proportional to r^6, so the closer the paramagnet is to a nucleus, the quicker the nuclear relaxation. T_1 is also proportional to $\langle S_z \rangle^{-2}$, so the greater the thermally averaged electron spin value, the shorter the relaxation time. This can lead to the case where the magnetic moment of the paramagnet is strong enough for the nucleus to relax on the timescale of the FID. It can then not contribute any signal to the total FID, so its signal has been wiped out beyond detection. Because of the r^6 strength of the interaction, NMR signal from nuclei within a sharp wipe out radius from a strong paramagnet will be screened beyond detection, leaving only signal from nuclei further away from strong paramagnetic sites.

2.5 Phase cycling

Phase cycling is used in all the experiments performed to remove unwanted artifacts in the NMR spectrum that were created by the receiver not being setup optimally. The FIDs are measured using quadrature phase detection where the NMR signal is split into

Transmitter Phase	0°	90°	180°	270°
Real channel	R	I	-R	-I
Imaginary channel	I	-R	-I	R

Table 2.1: The CYCLOPS phase cycling sequence[24].

two. One half is mixed with the carrier frequency, and the other half is mixed with the carrier frequency that has been phase shifted by 90°. These two channels are taken to be the real and imaginary signal.

There are three mechanisms that can occur in the receiver to create unwanted artifacts (quad images) after Fourier transformation[23]. The 90° phase shift between the two channels can drift. Both channels can acquire DC offsets (although this can be corrected by the processing software), and the gains of the two mixers can drift so one channel is amplified preferentially to the other.

In a single pulse experiment, the CYCLOPS (CYCLically Ordered Phase Sequence) sequence is usually employed to cancel out any artifacts[24]. The phase of the magnetisation tipping pulse is cycled through 0°, 90°, 180° and 270° over every four acquisitions, and the signal from the real and imaginary channels are added or subtracted from one of the two memory channels in the computer (table 2.1). This results in the artifacts being cancelled out. It is worthwhile to have the receiver reasonably well configured since more signal is cancelled out when the receiver is further from the proper settings. This is wasted signal which is not contributing to the spectra. The two computer FID channels are then converted into one NMR spectrum by performing a complex Fourier transform on them.

As well as being used for overcoming receiver deficiencies, phase cycling is also used in more sophisticated multiple quantum experiments performed on quadrupolar nuclei. By varying the phases of the excitation and conversion pulses, all unwanted coherence pathways can be cancelled out leaving only the signal from the desired coherence[21].

References

[1] C. P. Slichter, *Principles of Magnetic Resonance, Third Edition*, Springer-Verlag (1989).

[2] A. Abragam, *The Principles of Nuclear Magnetism*, Oxford University Press (1961).

[3] M. J. Duer, *Solid State NMR, Principles and Applications*, Blackwell Science (2002).

[4] M. H. Levitt, *Spin Dynamics: Basics of Nuclear Magnetic Resonance* Wiley, Chichester (2001).

[5] D. M. Grant, Chemical Shift Tensors, *Encyclopedia of NMR*, John Wiley and Sons, Chichester, **3** 1298 (1998).

[6] J. Mason, Conventions for the reporting of nuclear magnetic shielding (or shift) tensors suggested by participants in the NATO ARW on NMR shielding constants at the University-of-Maryland, College-Park, July 1992, *Solid State Nuclear Magnetic Resonance*, **2** 285 (1993).

[7] T. Gullion and J. Schaefer, Rotational-echo double-resonance NMR, *Journal of Magnetic Resonance*, **81** 196 (1989).

[8] M. H. Cohen and F. Reif, Quadrupole effects in nuclear magnetic resonance studies of solids, *Solid State Physics*, **5** 321 (1957).

[9] A. P. Guimarães, *Magnetism and Magnetic Resonance in Solids*, John Wiley and Sons, New York, (1998).

[10] A. Carrington and A. D. McLachlan, *Introduction to Magnetic Resonance*, Harper, New York, (1967).

[11] M. E. Smith and E. R. H. van Eck, Recent advances in experimental solid state NMR methodology for half-integer spin quadrupolar nuclei, *Progress in Nuclear Magnetic Resonance Spectroscopy*, **34** 159 (1999).

[12] R. J. Kurland and B. R. McGarvey, Isotropic NMR Shifts in Transition Metal Complexes: The Calculation of the Fermi Contact and Pseudocontact Terms, *Journal of Magnetic Resonance*, **2** 286 (1970).

[13] I. Bertini, C. Luchinat and G. Parigi, Magnetic susceptibility in paramagnetic NMR, *Progress in Nuclear Magnetic Resonance Spectroscopy*, **40** 249 (2002).

[14] H. M. McConnell and R. E. Robertson, Isotropic Nuclear Resonance Shifts, *Journal of Chemical Physics*, **29** 1361 (1968).

[15] C. P. Grey, C. M. Dobson, A. K. Cheetham and R. J. B. Jakeman, Studies of Rare-Earth Stannates by ^{119}Sn MAS NMR. The use of Paramagnetic Shift Probes in the Solid State, *Journal of the American Chemical Society*, **111** 505 (1989).

[16] Y. J. Lee and C. P. Grey, ^{6}Li Magic-Angle Spinning (MAS) NMR Study of Electron Correlations, Magnetic Ordering and Stability of Lithium Manganese(III) Oxides, *Chemistry of Materials*, **12** 3871 (2000).

[17] G. M. P. van Moorsel, E. R. H. van Eck and C. P. Grey, $Pr_2Sn_2O_7$ and $Sm_2Sn_2O_7$ as high-temperature shift thermometers in variable-temperature ^{119}Sn MAS NMR, *Journal of Magnetic Resonance A*, **113** 159 (1995).

[18] Y. J. Lee, F. Wang and C. P. Grey, ^{6}Li and ^{7}Li MAS NMR Studies of Lithium Manganate Cathode Materials, *Journal of the American Chemical Society*, **120** 12601 (1998).

[19] H. W. Spiess, *Dynamic NMR Spectroscopy. NMR Basic Principles and Progress*, **15** 55 (1978).

[20] K. H. Mueller, B. Q. Sun, G. C. Chingas, J. W. Zwanziger, T. Terao and A. Pines, Dynamic-angle spinning of quadrupolar nuclei, *Journal of Magnetic Resonance*, **86** 470 (1990).

[21] L. Frydman and J. S. Harwood, Isotropic spectra of half-integer quadrupolar spins from bidimensional magic-angle spinning NMR, *Journal of the American Chemical Society*, **117** 5367 (1995).

[22] M. M. Maricq and J. S. Waugh, NMR in Rotating Solids, *Journal of Physical Chemistry*, **70** 3300 (1979).

[23] D. D. Traficante, Phase-Sensitive Detection. Part II: Quadrature Phase Detection, *Concepts in Magnetic Resonance*, **2** 181 (1990).

[24] D. I. Hoult and R. E. Richards, Critical factors in the design of sensitive high resolution nuclear magnetic resonance spectrometers, *Proceedings of the Royal Society, London*, **344** 311 (1975).

Chapter 3

Experimental

3.1 NMR Experimental setup

The main equipment needed to perform an NMR experiment is outlined in figure 3.1. A sample is held within a room temperature probe which is inside a superconducting solenoid magnet. A suite of electronics connected to a computer is used to manipulate the magnetisation of the sample through radio frequency pulses. The sample's magnetic response to these pulses is measured, and processed on the computer. NMR has been applied to a wide range of chemical systems and subsequently there is a large volume of literature on the different techniques available. This chapter is compiled from recent books[1-4] and articles[5-10] on solid state NMR.

3.1.1 Fields

Four magnetic fields of 5.6, 7.05, 8.45 and 14.1 T were available in the laboratory which have proton frequencies of 240, 300, 360 and 600 MHz respectively. The bore-size of all the magnets once the room temperature shim coils have been installed is 89 mm, however the field maxima in the 14.1 T magnet is at a greater distance from the base of the magnet, so it needs its own set of slightly longer probes. Experiments within the 5.6 T magnet were conducted using a Chemagnetics CMX Lite spectrometer, which was interfaced to a Sun Sparcstation 2 computer running Spinsight spectral acquisition and processing software. The 7.05 T magnet used a slightly older Bruker MSL spectrometer with built in computer which ran DISMSL software. The 8.45 T spectrometer was the most modern, consisting

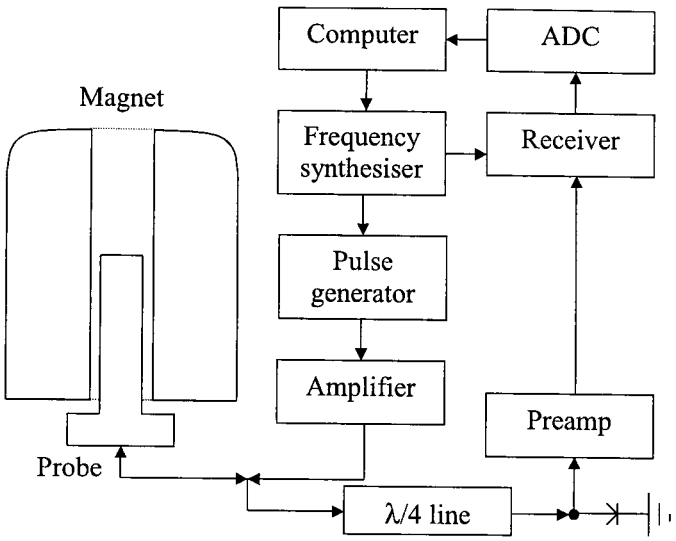

Figure 3.1: Schematic of the main components of an NMR spectrometer.

of a Chemagnetics Infinity console and a Sun Ultra 5 running Spinsight. Connected to the 14.1 T magnet was a similar Chemagnetics Infinity console, and a Sun Sparcstation 2 also controlled acquisition using Spinsight software. The philosophy behind the Spinsight software used differs slightly from the usual, slightly more powerful software which is used mainly for solution state NMR. Solution state experiments are usually very routine, and generally a large number of short experiments will be conducted, so the software is designed with quick and easy processing of the FIDs in mind, with an emphasis also on efficient database storage of the large amount of data acquired. Spinsight is better suited to solid state NMR where, due to the variety of nuclei examined and number of different probes and different pulse sequences typically used, easy optimisation of the experimental settings is more important than quick processing of data.

The magnets themselves all consisted of a superconducting solenoid cooled to 4.2 K by liquid helium. A set of superconducting shim coils within the magnet, and a set of copper shim coils in the room temperature bore of the magnet were used to maximise the homogeneity of the magnetic field. Since the sample in different probes sits at slightly different positions within the field, it was often necessary to re-shim the room temperature coils when changing to a different probe.

3.1.2 Probes

The probe is used for holding the sample in the main field B_0. Inside the probe, the sample is situated inside an inductor which is part of a resonant electrical circuit. This circuit can be tuned to the Larmor frequency ω_0 of the nucleus that is to be observed by using a variable capacitor and variable inductor present in the circuit. When the circuit is correctly tuned, it will efficiently convert an incoming electrical pulse of frequency ω_0 into an oscillating electromagnetic field within the coil. The nucleus can then couple with the magnetic component of this field and absorb quanta of energy $\hbar\omega_0$. After a 90° pulse, the magnetisation acts as if it has been rotated 90° away from the z-axis. It will then precess within the field at a frequency ω_0 which will induce a current within the probe coil. This weak electrical signal is then measured by the receiver.

A wide variety of probes were available for use with the spectrometers, each suited to a different type of experiment. Most allowed a sample to be spun and could be tuned to most nuclei with a gyromagnetic ratio equal to or larger than that of ^{17}O. Two commonly used NMR isotopes, ^{1}H and ^{19}F have gyromagnetic ratios that are much larger than the remainder of the nuclei (see table 3.2). To cope with this, most probes have two signal channels so the resonant circuit actually has two resonances, but still only the one inductor to manipulate the sample's magnetisation. The first channel, usually called X tunes over the range of common NMR nuclei. The second channel, H tunes to ^{1}H, and depending on the probe, ^{19}F as well. Having two channels also has the added advantage that the magnetisation of ^{1}H species can be manipulated by the spectrometer whilst simultaneously manipulating another species using the X channel (see section 3.2.4). The 600 MHz spectrometer takes this a stage further and using triple channel probes, three species of nuclei can be manipulated simultaneously through the X, Y and H channels.

Most probes differ from one another by the size of the rotor that is used to spin the sample. The rotor is usually spun by applying a high pressure stream of air around the rotor through the bearing line which holds the rotor clear of the stator. A second line, the drive, controls the angular velocity of the rotor by directing air onto a set of vanes which have been machined onto the rotor. The maximum velocity that the outside of the rotor can rotate at is then governed by the speed of sound in air[12]. The speed of sound in nitrogen is marginally higher, however this gas is normally used for spinning moisture

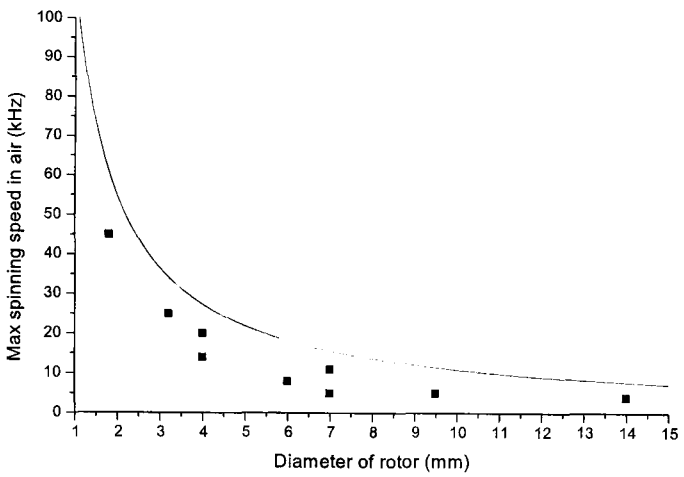

Figure 3.2: Maximum rotational speed F_{max} for a rotor spinning in air, given by $F_{max} = v_{air}/(\pi d)$[12] where v_{air} is the speed of sound in air, and d is the diameter of the rotor. Plotted are the rotor sizes and spinning speeds available in the laboratory.

sensitive samples.

The maximum rotational speed of the rotor will also depend on the diameter of the rotor, and plotted in figure 3.2 are the spinning speeds and rotor sizes available in the laboratory. Clearly, the disadvantage of using a smaller rotor that can spin faster is that less actual sample can be accommodated within the rotor. Although another advantage is that at smaller coil diameters, a higher B_1 can be created without the coil arcing, so shorter pulses can be used which excite a wider range of frequencies. In general, a choice of which probe to use will be a trade-off between these three factors.

3.1.3 Electronics

A radio frequency pulse is created by taking the carrier frequency from the frequency synthesiser and gating it with a square wave pulse of the desired length. This pulse is then phase shifted about an angle ϕ, and amplified before being fed into the probe.

Using the same coil for manipulating the sample's magnetisation, and measuring its response creates the problem that the high power pulse amplifier and sensitive receiver have to be connected to the same resonant circuit[11]. On three of the four spectrometers used, this is overcome by shielding the receiver using a quarter wavelength cable connected

to a grounded diode (figure 3.1). When a pulse travels down this $\lambda/4$ line, it will easily have a high enough voltage to overcome the diode's activation voltage, and will be reflected back down the $\lambda/4$ line rather than go into the receiver. The reflected signal will be half a wavelength out of phase when it has travelled back down the $\lambda/4$ line, and will destructively interfere with the incoming signal. The result of all this is that when the pulse is on, everything in the circuit from the start of the $\lambda/4$ line to the receiver is effectively removed from the circuit.

After the pulse, the tiny voltage created by the sample (of order μV) will not be enough to cause the diode to conduct, and so goes straight into the receiver rather than to ground. The amplifiers are also blanked out after the pulse so they cannot introduce any spurious signals into the receiver. The signal is usually amplified by a preamplifier straight after the diodes before being sent on the rest of the way to the receiver. Once the amplified signal is in the main receiver, it is split into real and imaginary components. These are digitised by the analogue to digital converter (ADC) within the receiver. The time interval over which each point is sampled for is the dwell time, and this determines the frequency window observable, since the spectral width is the reciprocal of the dwell time. The signal is also filtered before analogue to digital conversion to attenuate unwanted noise from outside the frequency window of interest.

3.1.4 Variable temperature NMR

Most MAS probes allow variable temperature measurements to be performed by heating or cooling the bearing gas line whilst the sample is spinning. Variable temperature measurements were only performed here using a Bruker 7 mm probe which has a heating element running the length of the bearing line inside the probe before the stator.

To perform high temperature measurements, it is simply a matter of heating the bearing line with a temperature control unit connected to the heating element and a thermocouple inside the probe. Nitrogen gas is used to stop the heating element from oxidising. This gas is also used for low temperature measurements since components of air can freeze at relatively high temperatures. For low temperature measurements, the nitrogen also needs to first pass through a heat exchanger submerged within a dewar of liquid nitrogen. It is then heated by the element in the probe to the desired temperature.

3.2 Pulse sequences used

A wide variety of pulse sequences exist to manipulate sample magnetisation in different manners. The different pulse sequences used to investigate the pigment samples are explained here.

3.2.1 Single pulse

A simple, single pulse experiment is depicted in figure 3.3. Here, the magnetisation is tipped through an angle $\pi/2 = \gamma B_1 t_p$, and the FID is measured using a four step phase cycle sequence. The FID cannot be acquired immediately after the end of the pulse since the electronics take a finite time to blank the amplifiers off, and get the receiver ready for acquisition.

Another effect contributing to the deadtime is probe coil ringdown. When the B_1 pulse is applied to the coil, it is suddenly subject to the force between the oscillating B_1 field and the static B_0 field. This causes it to oscillate at the Larmor frequency ω_0, and when the pulse is turned off, its continued oscillation within B_0 can cause a voltage to be induced in it. This can be detected by the receiver, and the time this spurious signal takes to decay is dependant on the diameter of the coil, the frequency of the pulse and the material the coil is manufactured from. Ringdown can typically last for a millisecond for a low-γ nucleus (^{109}Ag) in a 10 mm coil, or a couple of microseconds for a medium-γ nucleus (^{27}Al) in a 3.2 mm coil.

Different tip angles can be used if the T_1 relaxation time for the sample is long. For example, a 30° tip angle was used for most of the ^{29}Si measurements, and the time taken for the magnetisation to effectively relax back along the field is approximately T_1. Another advantage of the shorter pulse is that it allows a wider range of frequencies to be irradiated, however this is not usually a limitation in ^{29}Si NMR.

When examining quadrupolar nuclei, the 90° pulselength is usually measured for a solution reference. The pulselength used for the main experiment is then this 90° value, divided by the factor $I + \frac{1}{2}$. Since the angle a quadrupolar nucleus is tipped to is dependant on the quadrupolar coupling, C_Q of the nucleus, as well as the length of the pulse, this ensures that the excitation of quadrupolar nucleus lies in the linear regime[9].

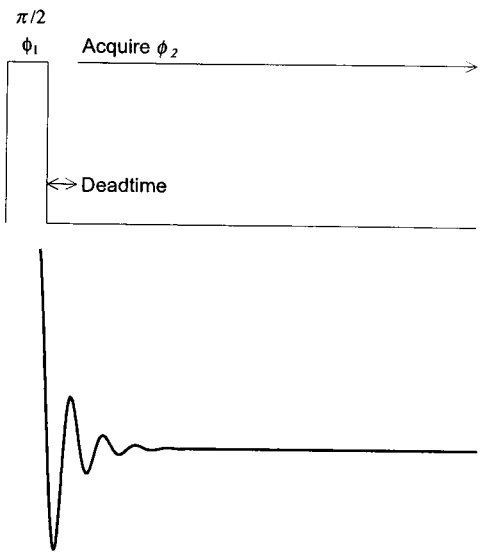

Figure 3.3: A single pulse sequence.

So if a variety of resonances with different C_Qs are present in the sample, they will all be effectively tipped to a similar angle. This can allow quantitative analysis to be performed on spectra of quadrupolar nuclei.

Data processing

Once the FID has been acquired, it then needs to be converted into a frequency domain spectrum. A number of techniques were used to enhance the clarity of spectra, and typical processing steps for a single pulse and echo acquisition are illustrated in figure 3.4.

A DC offset correction was used to ensure that the end of the FID, where there was no signal present averaged about the $y = 0$ axis. The acquisition software looked at the last portion of the FID and calculated the mean value of the data over this period. It then subtracted this amount from the entire acquisition so the FID oscillated about the correct baseline. The phase cycling employed usually left the final FID tail reasonably close to the baseline to begin with.

Linear back prediction was used to simulate the first datapoints in the FID that could not be acquired due to the receiver deadtime. If the FID does not begin at $t = 0$ when the magnetisation actually started precessing after the pulse, the points missed out

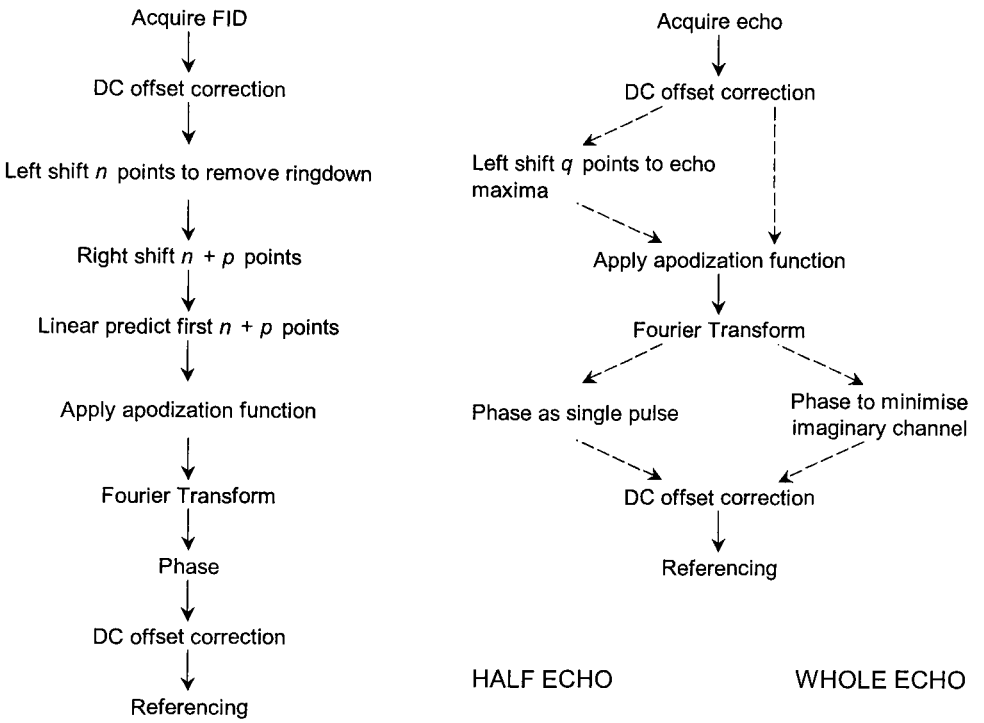

Figure 3.4: Typical processing steps for converting a FID from a single pulse experiment (left) and an echo experiment (right) into a referenced spectrum. n is the number of points at the beginning of the FID containing ringdown, p is the number of points not acquired due to receiver deadtime and q is the number of points from the beginning of the FID to the echo maxima.

will manifest themselves as a rolling baseline in the Fourier transformed spectrum.

Exponential line broadening was also used to preferentially enhance the beginning of the FID where the signal was greatest relative to the noise. This is where the FID $S(t)$ is multiplied by an exponential decay function[11]:

$$A(t) = S(t) \times \exp(-\pi L_B t) \tag{3.1}$$

where the L_B parameter controls how much broadening is applied. The tail end of the spectrum, which is only noise is then attenuated. Exponential line broadening increases the width of any lines in the spectrum in a Lorentzian manner.

Gaussian broadening can also be applied with exponential broadening which will

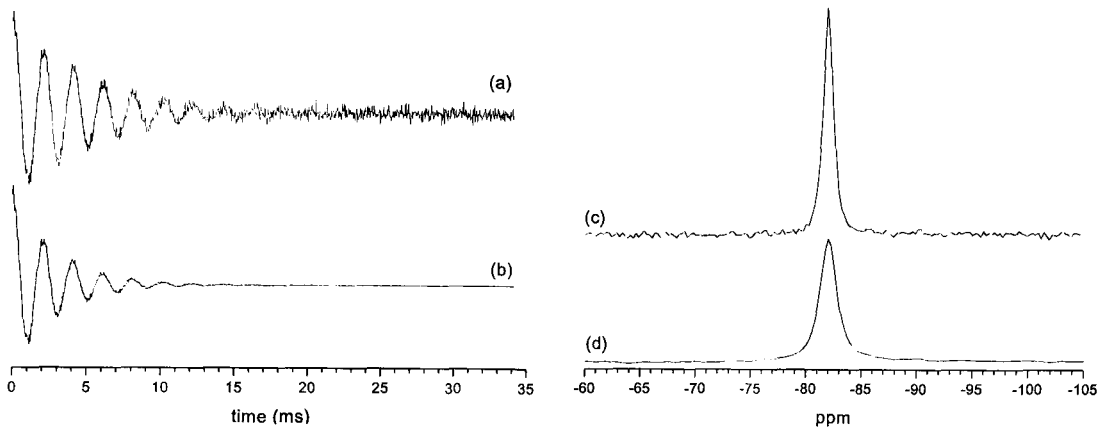

Figure 3.5: A FID and spectrum before ((a) and (c)) and after ((b) and (d)) 50 Hz exponential line broadening.

add a Gaussian component to the lineshape:

$$A(t) = S(t) \times \exp\left[-\pi L_B \left(t - \frac{t^2}{2G_B A_L}\right)\right] \tag{3.2}$$

where G_B is the amount of Gaussian broadening applied, and A_L is the length of the FID acquisition in seconds. Figure 3.5 shows a FID and its Fourier Transform before and after the application of 50 Hz of exponential line broadening. Before broadening, the resolution of the line is better, however after broadening the background noise has been attenuated, and the line broadened. By applying Gaussian broadening with a negative G_B, the opposite effect happens. The resolution of a line can be further increased which can be useful when attempting to resolve solution spectra, however the baseline noise will also be increased.

Once the FID has been Fourier transformed, it needs to be phased. When the FID is acquired into the real and imaginary channels of the receiver, the receiver has no information about the phase of the real part of the signal, so a mixture of the real and imaginary components of the signal will be present in both channels. Phasing is the procedure where the phase angle between the real channel of the receiver and the real component of the data is adjusted until the spectrum visually has a horizontal baseline and peaks that point vertically upwards. The only component of the data presented in a conventional spectrum is the real part, which after phasing should be entirely contained

within the real channel. This zero order phasing is described by equation 3.3[11].

$$A(\omega) = pA_R(\omega)\cos(\omega) + \sqrt{1-p^2}A_I(\omega)\sin(\omega) \tag{3.3}$$

where $A_R(\omega)$ and $A_I(\omega)$ are the unphased real and imaginary components of the spectrum. First order phasing can also be used to correct for small amounts of deadtime at the beginning of FIDs, and is also important for processing whole echo experiments. This assumes that the phase is not the same for all frequencies, but varies linearly instead. p in equation 3.3 is then replaced by

$$p = p_0 + p_1(\omega - \omega_0) \tag{3.4}$$

where p_0 and p_1 are the zero and first order phase angles.

Finally, a second DC operation is usually performed to ensure that the baseline of the spectrum is at $y = 0$. This step is performed since integrations performed on lines in the spectrum will not measure the correct integral if there is a DC offset component present.

3.2.2 $\frac{\pi}{2} - \pi$ echo with extended phase cycling

In this echo experiment, the magnetisation is first tipped by a $\frac{\pi}{2}$ pulse and allowed to evolve for a time τ. It is then tipped by a pulse twice as long (π here), and after another time τ an echo will form (figure 3.6). For the case of a $\frac{\pi}{2} - \pi$ pulse sequence, this can be explained using the rotating frame model of the magnetisation introduced by Bloch. The first pulse tips the magnetisation about the y axis from lying on the z axis onto the x axis. These spins then dephase in the $x - y$ plane since some spins will precess faster than the rotating frame precession, and some spins will precess slower. This causes the FID signal to decay to nothing. A time τ afterwards, the magnetisation is flipped 180° about the y axis so the dephased spins still lie in the $x - y$ plane, but are a mirror image of themselves (the mirror being the $x - z$ plane). The spins now precess in the opposite direction at the same speed they dephased at, so a time τ after the second pulse, all the spins recombine to create an echo.

There are two commonly performed echo experiments, whole echo acquisition and half echo acquisition. Whole echo experiments are suitable for acquiring spectra of broad

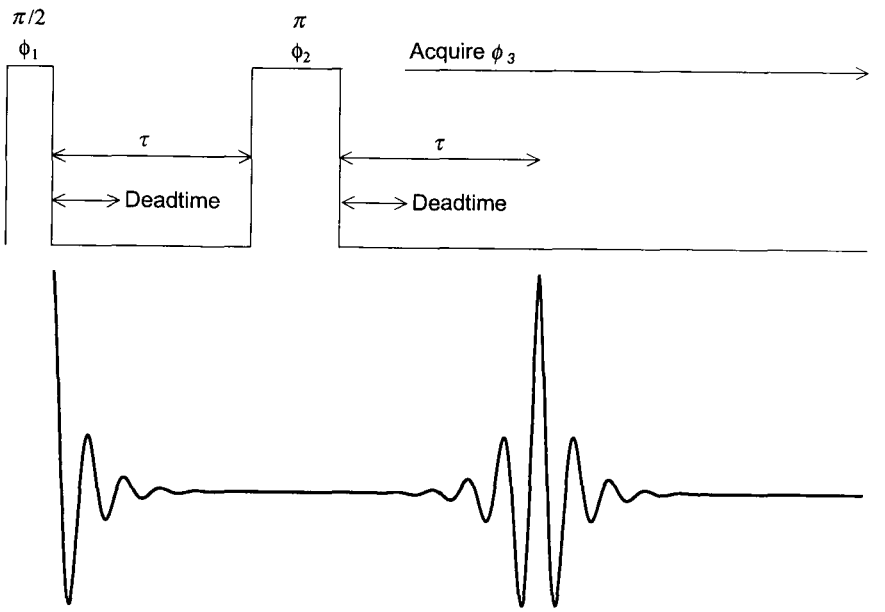

Figure 3.6: The $\frac{\pi}{2} - \pi$ pulse sequence.

ϕ_1	$xxxx$	$yyyy$	$\bar{x}\bar{x}\bar{x}\bar{x}$	$\bar{y}\bar{y}\bar{y}\bar{y}$
ϕ_2	$xy\bar{x}\bar{y}$	$xy\bar{x}\bar{y}$	$xy\bar{x}\bar{y}$	$xy\bar{x}\bar{y}$
ϕ_3	$\bar{y}y\bar{y}y$	$\bar{x}x\bar{x}x$	$y\bar{y}y\bar{y}$	$x\bar{x}x\bar{x}$

Table 3.1: The 16 step phase cycling sequence used for the $\frac{\pi}{2} - \pi$ echo. $x, y, \bar{x}$ and $\bar{y}$ represent $0°, 90°, 180°$ and $270°$ phase shifts.

lines. Half echos are used for narrower lines which will have longer echos. Since a longer τ is needed to acquire all of the first half of a long echo, T_2 relaxation effects can cause the intensity of the whole echo to be attenuated. A compromise is to select τ such that the second half of the echo is acquired instead of the whole echo. This leads to the problem that the FID tail created by the first pulse can run into the acquisition of the echo. This problem was overcome in 1986[13] where extended phase cycling was introduced to create destructive interference of the FID tails from the initial $\pi/2$ pulse, whilst allowing the spin echos to constructively add. Table 3.1 shows the 16 step phase cycling used where ϕ_1, ϕ_2 and ϕ_3 are the phases of the first and second pulses, and of the receiver.

If a sample is being spun during the experiment, τ needs to be an integer number

of rotor cycles apart. This can then limit how short τ can be since for a sample spinning at 10 kHz, τ needs to be a multiple of 100 μs, whereas for a static sample τ can be as low as $\sim$ 10 μs.

Processing the FIDs is also slightly different, and figure 3.4 shows the typical procedures employed. Exponential broadening will usually be applied, however in the case of the full echo acquisition, the exponential maxima needs to coincide with the echo maxima. Phasing is also different, the half echo will require no first order phasing since the acquisition begins at the maxima of the FID. Extensive first order phasing is required for whole echos since the FID maxima is some time into the acquisition. Phasing is simplified slightly for whole echos since the positive and negative t of the signal has been measured, so the imaginary channel will be zero when the spectrum is correctly phased to zero and first order.

3.2.3 $\frac{\pi}{2} - \frac{\pi}{2}$ echo

The $\frac{\pi}{2} - \pi$ echo sequence is suitable for refocusing chemical shift anisotropy and heteronuclear dipole-dipole coupling[4]. The quadrupolar or solid echo $\frac{\pi}{2} - \frac{\pi}{2}$ pulse sequence is suitable for lines whose dominant broadening mechanism is through quadrupolar coupling or homonuclear dipole-dipole coupling. It was this pulse sequence which lead to the first observation of an echo by Hahn.

3.2.4 Cross polarisation

Cross polarisation (CP) is a two channel technique where the magnetisation from proton and X-channel nuclei are manipulated simultaneously. Figure 3.7 shows the pulse sequence employed for the two channels.

The pulse sequence starts with a $\frac{\pi}{2}$ pulse on the H channel which effectively moves the proton magnetisation onto the $x - y$ plane in the rotating frame picture. This is followed by a contact pulse on both channels. If the Hartmann-Hahn match condition is met:

$$\gamma_H B_{1H} = \gamma_X B_{1X} \tag{3.5}$$

then both the X and H nuclei will precess at the same rate, and are spin-locked. The magnetic energy level splitting for the two species are then equal, so magnetisation from

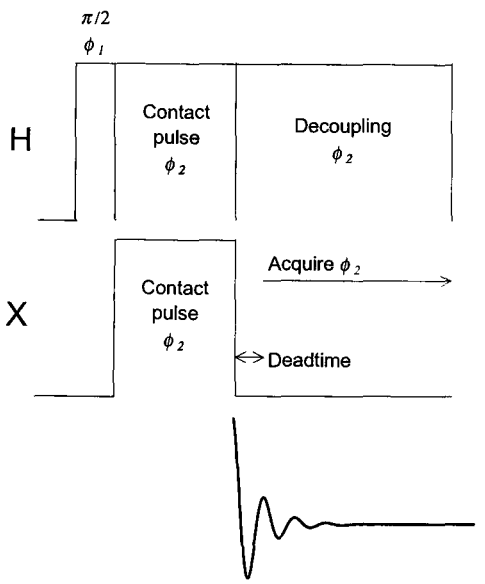

Figure 3.7: The cross polarisation pulse sequence.

the protons induced by the earlier $\frac{\pi}{2}$ pulse can then exchange energy with nearby X channel nuclei through the flip-flop B term in the dipolar interaction (equation 2.16). When the contact pulse is turned off, a normal FID can then be measured from the X channel nuclei since the X magnetisation is now effectively precessing in the $x - y$ plane. A decoupling field is usually applied to the proton channel whilst acquisition is performed. This is used to keep the protons continually precessing so that any dipolar couplings between protons and X channel nuclei are averaged out.

This technique has only been applied to ^{13}C in this work and has the advantage that since the ^{13}C magnetisation is derived from the $\frac{\pi}{2}$ pulse on the proton channel, the recycle delay used is limited by the T_1 time of the protons in the sample. This is usually much faster than for the ^{13}C nuclei. This technique will only excite resonances of X channel nuclei who are close enough to protons to exchange magnetisation during the contact period, and this can be useful for filtering out only C-H species in samples.

Magic angle spinning averages out dipolar couplings and so reduces cross polarisation efficiency. At high spinning frequencies, achieving a good match condition becomes more difficult and so relatively modest spinning speeds tend to be used in conjunction

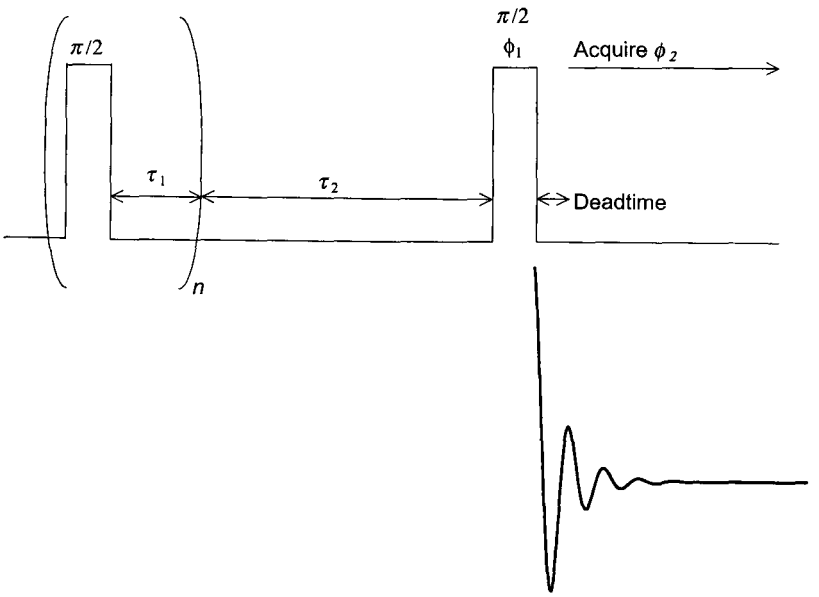

Figure 3.8: The saturation-recovery pulse sequence.

with CP.

3.2.5 Saturation recovery

Saturation recovery is a technique used for measuring the T_1 times of resonances, and the pulse sequence used is depicted in figure 3.8. The magnetisation is initially saturated by a train of $\frac{\pi}{2}$ pulses, resulting in the net magnetisation being reduced to nothing. It is important that these pulses are spaced by at least the time it takes the FID to decay to zero, otherwise the magnetisation tends to be spin locked by the pulses and is not reduced to zero by the end of the train.

The magnetisation is then allowed to recover for a time τ_2, and after a $\frac{\pi}{2}$ detection pulse the FID is measured. The experiment is then repeated for a number of different τ_2. T_1 is calculated for a resonance by measuring the integral of the resonance line for each τ_2 and fitting them to equation 2.7 which is

$$M_z(\tau_2) = M_0 \left(1 - \exp\left(\frac{-\tau_2}{T_1}\right)\right)$$

Another technique used for measuring T_1 times is a $\pi - \tau - \frac{\pi}{2}$ pulse sequence. In the rotating frame, the magnetisation is initially rotated onto the $-z$ axis by the π pulse. After recovering for a time τ, the magnetisation is then measured after the $\frac{\pi}{2}$ detection pulse. This technique is not as suitable as saturation recovery for long T_1 species since the magnetisation needs to completely recover between acquisitions, so a delay of $4T_1$ is needed. The saturation recovery technique is limited by the longest τ_2 employed.

3.3 Spectral simulation

Some of the lineshapes produced by the interaction Hamiltonians can be simulated using the windows based Winfit software[14]. For simple $I = \frac{1}{2}$ nuclei experiments, it allowed Gaussian and Lorentzian lines to be fitted which was useful for fitting Q^n silicate species in ^{29}Si spectra. It also allowed simulation of spinning sideband manifolds dominated by the chemical shift interaction. Spinning quadrupolar central transition lineshapes could be calculated, although the software assumed an infinite spinning speed. Static quadrupolar lineshapes could also be simulated with an additional CSA tensor component. Fitting quadrupolar parameters at multiple fields was also a valuable unambiguous method of fitting quadrupolar spectra, since the quadrupolar parameters must be the same at every field. However, the spectra will be different due to the ν_0^{-1} dependence of the second order quadrupolar effect with field (equation 2.20).

3.4 Physical properties of NMR nuclei studied

Listed in table 3.2 are some relevant properties of the nuclei studied during this work. Receptivity is loosely defined as $CB_0^2\gamma^{2-3}/kT$ where C is the natural abundance of the isotope under investigation. Receptivity is a measure of the amount of signal one can expect to measure from a particular nucleus at different temperatures and magnetic fields, so an experiment at 14.1 T will give a factor of 4 increase in signal compared to an experiment at 7.05 T. Low temperature NMR measurements also give a greater signal than at room temperature, as long as the sample's chemistry is the same at the lower temperature. Due to the increased experimental complexity involved, this technique is not generally used to increase signal to noise.

Isotope	Spin I	C (%)	γ (10^7 rad T^{-1} S^{-1})	Q (10^{28} m^2)	Quadrupole broadening	Receptivity relative to ^{13}C
^{1}H	$\frac{1}{2}$	99.985	26.7520			5.67×10^3
^{11}B	$\frac{3}{2}$	80.42	8.5843	2.83×10^{-1}	4.06×10^{-2}	7.52×10^2
^{13}C	$\frac{1}{2}$	1.108	6.7283			1.00
^{17}O	$\frac{5}{2}$	0.037	-3.6279	-2.56×10^{-2}	6.40×10^{-2}	6.11×10^{-2}
^{19}F	$\frac{1}{2}$	100	25.181			4.73×10^3
^{23}Na	$\frac{3}{2}$	100	7.08013	0.10	2.47	5.26×10^2
^{27}Al	$\frac{5}{2}$	100	6.9760	0.15	1	1.17×10^3
^{29}Si	$\frac{1}{2}$	4.70	-5.3188			3.69×10^{-4}
^{51}V	$\frac{7}{2}$	99.76	7.0453	-5×10^{-2}	5.78×10^{-2}	2.17×10^3
^{91}Zr	$\frac{5}{2}$	11.23	-2.4959	-0.21	6.02	6.04
^{107}Ag	$\frac{1}{2}$	51.82	-1.087			0.197
^{109}Ag	$\frac{1}{2}$	48.18	-1.250			0.279
^{119}Sn	$\frac{1}{2}$	8.58	-10.021			25.6

Table 3.2: Physical properties of the NMR nuclei studied in this thesis (from Harris[2] and Smith and van Eck[9]).

The receptivity values listed in table 3.2 do not take into account the typical T_1 relaxation time of the species present in the sample which will obviously differ between systems. Hence, even though the ^{109}Ag silver isotope is $\times 10^3$ more receptive than ^{29}Si, ^{29}Si is usually the easier nucleus to study since T_1 relaxation is typically two orders of magnitude faster.

The receptivity also makes no distinction between spin $I = \frac{1}{2}$ and quadrupolar nuclei where the signal will be distributed between the $2I$ transitions. A quadrupole broadening column has been included in table 3.2 which gives the second-order quadrupolar broadening factor, which has been normalised to that of ^{27}Al and is proportional to[9]

$$\text{Quadrupolar broadening} \sim \frac{Q^2}{\gamma} \frac{\left(a - \frac{3}{4}\right)}{\left(2I\left(2I-1\right)\right)^2} \tag{3.6}$$

Listed in table 3.3 are the primary and secondary references used to determine the 0 ppm reference of the chemical shift scale. Choosing quadrupolar references can be challenging since if there is an electric field gradient present at the probe nucleus in the reference compound, the quadrupolar induced shift will make the reference field dependant, which makes comparing spectra taken at different fields problematic.

Isotope	Reference compound	Secondary reference	Secondary shift
^{1}H	TMS $Si(OCH_3)_4$		
^{11}B	$BF_3.(CH_3)_2O$	Boric acid H_3BO_3	18.8 ppm
^{13}C	TMS $Si(OCH_3)_4$	Adamantane $C_{10}H_{16}$	38.56 and 29.5 ppm
^{17}O	H_2O		
^{19}F	$CFCl_3$		
^{23}Na	NaCl solution	NaCl powder	7.2 ppm
^{27}Al	$Al(H_2O)_6^{3+}$	AlO_6 line in YAG	0.7 ppm
^{29}Si	TMS $Si(OCH_3)_4$		
^{51}V	$VOCl_3$	0.016M $NaVO_3$ solution	−574.4 ppm
^{91}Zr	bis(cyclopentadienyl)zirconium dibromide in tetrahydrofuran	$BaZrO_3$	208.1 ppm
$^{107,109}Ag$	$AgNO_3$ solution		
^{119}Sn	$Sn(CH_3)_4$	SnO_2	−604.3 ppm

Table 3.3: Primary reference compounds for the isotopes studied, and where relevant, the secondary shift agents used have also been listed.

3.4.1 ^{17}O NMR

^{17}O ($I = \frac{5}{2}$) has a relatively large chemical shift range and small quadrupole moment so spectra can be acquired which are very sensitive to the local environment. They can also be acquired quite quickly because of the small quadrupolar effects which aid relaxation. The main drawback with this nucleus is its low natural abundance of only 0.037%, so isotopic enrichment of samples is usually necessary.

3.4.2 ^{29}Si NMR

^{29}Si is a spin $I = \frac{1}{2}$ nucleus with quite a low abundance of 4.7%. Despite the low abundance, ^{29}Si MAS NMR has been used extensively here to characterise impurity-doped zircon pigments. The favourable gyromagnetic ratio of the isotope and level of scientific interest in silicon compounds has made ^{29}Si a routine solid state NMR nucleus. At a field of 7.05 T, spinning speeds in excess of 5 kHz are rarely needed since the bulk of ^{29}Si resonances lie in the chemical shift range $\sim$ 0 to −150ppm. ^{29}Si NMR has been widely used as a technique for quantification of Q^n species in amorphous silicate oxides (n being the number of non-bridging oxygen bonds at the SiO_x site) since δ_{iso} is dependant on n[15].

Paramagnetic effects

Signal screening in silicate samples by paramagnetic impurity dopants needed to be rationalised to ensure that signal loss in ^{29}Si spectra was at an acceptable level. The methodology employed was to weigh samples after ^{29}Si measurements so that a molar signal could be calculated. This was then normalised with respect to the molar signal given by a silicate reference compound containing no paramagnetic impurities. Provided this normalised value was at least 50-60% that of the reference compound, screening was deemed to be at an acceptable level to allow reasonably unambiguous spectral interpretation. When performing signal quantification experiments, it was important to ensure that a sufficiently long pulse recycle delay was used so that signal saturation did not affect the measurements. This was especially important for the reference compound where paramagnetic doping could not provide a means of efficient T_1 relaxation.

3.4.3 ^{91}Zr NMR

Despite being a very useful nucleus in the world of high strength ceramics, ^{91}Zr has not been the subject of much study by NMR either in the liquid or solid states[16]. The large quadrupole moment of the nucleus leads to couplings of $C_Q \sim 20$ MHz for ZrO_2 (monoclinic, tetragonal and orthorhombic)[17] and so mainly cubic materials have been studied.

At a field of 14.1 T, the central transition resonance of a site with $C_Q = 20$ MHz is ~ 300 kHz wide and MAS is not a suitable method for increasing resolution. A homemade static probe-head was used with additional resistance added in series with the coil to reduce the Q of the probe. Q is a measure of the sharpness of the frequency response of the probe, and is defined as the resonance frequency divided by the fullwidth at half height of the frequency response. When using sufficiently hard pulses (shorter than 2 μs), the Q-spoiling created a uniform probe response over ~ 500 kHz giving reasonably undistorted quadrupolar lineshapes. Q-spoiling also reduces the ringdown time and so echo acquisition can begin sooner. A uni-axial press was used to compact samples into a cylindrical pellet. This allowed more sample and less air to be measured, increasing the filling factor for the coil.

3.5 X-Ray diffraction

X-Ray diffraction measurements were used to verify sample phase composition. Spectra were acquired at Warwick on a Philips diffractometer using a Cu K_α source which has a frequency of 1.5419 Å. Measurements were also performed at Johnson Matthey using a Bruker AXS D-50 diffractometer also employing Ni filtered Cu K_α radiation. Typical scan rates of 0.25° 2θ per minute were used on both, covering a range of $10° \leq 2\theta \leq 70°$ in steps of 0.05° 2θ.

3.5.1 Crystallographic calculations

Interrogation of crystal structure data was helped through two software packages. Crystalmaker 2 running on a power macintosh allowed visualisation and bond angle and length calculations to be performed. GSAS was also used to perform more accurate bond calculations.

3.6 Sample Manufacture

3.6.1 Doped zircon pigments

Three undoped crystalline zircon samples were prepared by mixing finely ground ZrO_2 and SiO_2 powders in an equimolar ratio. NaF, NaCl and other fluxing agents were also added to lower the temperature required for zircon to form. These powders were mixed in a turbular mixer for at least ten minutes to create a homogeneous mixture.

Commercial zircons are fired by passing a closed crucible containing the reactants through a furnace on a conveyor belt. To mimic this environment, a Nanneti fan assisted furnace was used to ramp the samples up to temperature over 20 minutes. The samples were then kept at temperature for 20 minutes at either 860°C or 1060°C, before being cooled during a final 20 minute period.

Yellow praseodymium-doped zircons were produced using this same recipe with the addition of Pr_6O_{11} as a Pr^{4+} source. A firing temperature of 1060°C was needed for the reaction to complete. Two series of Pr-doped zircons were made where sample production variables were systematically changed to try and influence the amount of Pr^{4+} entering

the zircon lattice. In one set of five samples, the PV series were made using variable amounts of Pr_6O_{11}. PV1 had 25% the known optimum amount of Pr. PV2 through PV5 had 50%, 75%, 100% and 125% of the optimum amount which is typically $\sim$ 1 mol%. All these samples were fired for 20 mins at 1060°C with 20 min ramp up and ramp down periods.

A second set of samples, the PT series all used the optimum Pr source recipe. However, the amount of time the samples were fired for was varied. The samples were ramped to and from 1060°C over 15 minute periods with PT1 through PT4 being held at temperature for 0, 10, 20 and 60 minutes. Both series of Pr-doped samples were milled and washed after firing to remove toxic water soluble byproducts formed from the fluxing agents.

A set of Fe-doped zircons were also prepared. Since the colour forming mechanism is thought to be due to $\alpha-Fe_2O_3$ mixed in with the zircon, it was decided that acid washing the samples rather than modifying the starting Fe content would be a more suitable way to influence the amount of Fe in the sample. The samples were prepared by mixing an equimolar ratio of ZrO_2 and SiO_2 along with NaF and NaCl mineralisers. The mixing technique was also varied. Three samples were made by either mixing the reactants using a turbular mixer, by pressing them into a pellet or by dry milling them prior to firing. After firing at 1060°C for 20 mins (and two 20 min ramp periods), a portion of each sample was wet milled and acid washed to try and remove as much iron as possible.

Nb-, Mn- and Cd-doped zircons were prepared in a similar manner to the Pr- and Fe-doped zircons. Nb- and Mn-doped zircons were prepared by mixing an equimolar ratio of ZrO_2 and SiO_2 in a turbular mixer along with a NaF mineraliser. NbO_2 was added as a pigment source for Nb-doped zircon whilst $MnCO_3$ was used for Mn-doping. These mixtures were then heated to 1060°C in a closed crucible for 20 mins, with 20 min ramp up and ramp down periods. CdS was used as a Cd source, and the SiO_2, ZrO_2 and NaF reactants were also mixed in a turbular mixed, and heated to 950°C for 20 mins in a closed crucible, with the same 20 min ramping periods.

3.6.2 Vanadium-Doped Zircon

Sample preparation was similar to the praseodymium-doped zircons, except that due to the fluxing effects of the V_2O_5 V^{4+} source used, the samples only needed to be fired at 860°C. Again, two series of samples were produced. The VV samples were made using varying amounts of V_2O_5 source, with VV1 through VV5 using 25%, 50%, 75%, 100% and 125% of the optimum amount.

The VT series of samples were made using the optimum recipe using different firing times. VT1 through VT4 were heated to and from 860°C over 15 min periods, and held at temperature for 0, 10, 20 and 60 minutes. VT5, VT6 and VT7 were heated to and from 1060°C in 15 min segments, staying at temperature for 0, 10 and 20 mins.

After firing, a small portion of unwashed sample was set aside and the remainder was wet milled for 2 mins. This was then washed and dried. The water used to wash the samples was analysed using an inductive coupled plasma technique to measure the concentrations of vanadium species present. This allowed the amount of vanadium that should be left within the sample to be elucidated.

V-$ZrSiO_4$ was also prepared using a sol-gel route which enabled ^{17}O enriched water to be added. The extra ^{17}O which was incorporated into the pigment helped make ^{17}O NMR possible, overcoming the main experimental complication which arises from the natural abundance of ^{17}O being only 0.037%. Zirconium-n-propoxide was dissolved in ethanol with 10% ^{17}O-enriched water. A hydrated vanadium source was dissolved in ethanol and added to the mixture, followed by tetraethylorthosilicate (TEOS) also dissolved in ethanol. The mixture was stirred for three hours with a magnetic stirrer bar, dried overnight at 60°C and dried under vacuum for 24 hours. NMR was performed at multiple field strengths before and after firing in air for 30 minutes at 1000°C.

3.6.3 Silver glasses and silver reference compounds

Silver glasses were made by mixing the oxides: SiO_2, Na_2O, B_2O_3, Al_2O_3 and Ag_2O. The reactants were mixed in a turbular mixer for 10 minutes, and then heated in a crucible to 1500°C at 30°C min^{-1}. It was then held at temperature for 60 mins, and quenched by pouring into cold water. The quenched glass was finally wet milled for 10 mins and sieved using a 58 μm mesh sieve. This powder was dried and divided into four portions, three

of which were pressed into a pellet using a uni-axial press, and subjected to further heat treatments.

One pellet was placed into an oven preheated to 400°C, and was left there for 30 mins. One pellet was heated in a fast fire furnace to 800°C over 10 mins. This was held at temperature for 30 mins, and ramped back down to room temperature over a final 10 min period. The third pellet was heated to 1200°C over 20 mins, held at temperature for three mins, and ramped back down to temperature again over 5 mins.

Two silver halides, AgI and AgCl were synthesised. AgCl was produced by dissolving $AgNO_3$ and NaCl in separate beakers of deionised water in equimolar ratios. These two solutions were then mixed together causing an AgCl precipitate to form. This was then filtered out, washed thoroughly and allowed to dry in an oven. A similar procedure was followed to create AgI, however the NaCl was replaced with NaI.

3.6.4 Tin-Zinc-Titanium (TZT) pigment preparation

Yellow coloured TZT pigments were prepared in a similar manner to the doped zircon pigments. A 1:1:2 mixture of SnO, ZnO and TiO_2 were mixed in a turbular mixer for 10 minutes. This was then heated in a closed crucible in the Nanneti fast-fire furnace by ramping the sample up to 950°C over a 18 min period. This was held at temperature for a further 18 mins, and then cooled to room temperature over a final 18 min period. The samples were then ground in a pestle and mortar, however no sample washing was required since no toxic mineralisers were incorporated into the starting mixture.

The effects of different firing temperatures and Na_2CO_3 additions were investigated, so three batches of samples were prepared. In a first set of samples, the usual TZT recipe was prepared, however the heating time was varied in 100°C steps from 18 mins at 500°C to 18 mins at 900°C. A second set of samples was prepared with the addition of 5 mol% Na_2CO_3. These samples were heated to 550, 650, 750, and 850°C for 18 mins. A third set of pigments were produced with Na_2CO_3 added at 1, 2, 5, 10 and 20% levels. These were heated only at 850°C for 18 mins.

3.6.5 ^{17}O enriched SnO_2

Tin isopropoxide was dissolved at 10 wt% in isopropanol. Whilst stirring the solution, 20% ^{17}O enriched water was slowly added in the molar ratio $2(H_2O)$ to $1(Sn(OPr)_4)$. This was stirred continuously for several days until gelling occurred. The gel was then further dried by placing it under a vacuum for 24 hours. The sample was then heated sequentially to different temperatures in the range $150, 300, \ldots, 900°C$ under a nitrogen atmosphere to reduce ^{17}O loss, with multi-nuclear NMR being performed on the sample after every heat treatment.

References

[1] E. Fukushima and S. B. W. Roeder, *Experimental Pulse NMR. A Nuts and Bolts Approach*, Addison-Wesley, Massachusetts (1981).

[2] R. K Harris, *NMR Spectroscopy: A Physiochemical view*, Longman, Harlow (1983).

[3] M. H. Levitt, *Spin Dynamics: Basics of Nuclear Magnetic Resonance* Wiley, Chichester (2001).

[4] M. J. Duer, *Solid State NMR, Principles and Applications*, Blackwell Science (2002).

[5] R. J. Kirkpatrick, MAS NMR spectroscopy of minerals and glasses, *Reviews in Mineralogy*, **18** 341 (1988).

[6] J. F. Stebbins, NMR spectroscopy and dynamic processes in mineralogy and geochemistry, *Reviews in Mineralogy*, **18** 405 (1988).

[7] A. P. M. Kentgens, A practical guide to solid-state NMR of half-integer quadrupolar nuclei with some applications to disordered systems, *Geoderma*, **80** 271 (1997).

[8] M. E. Smith and J. H. Strange, NMR techniques in materials physics: a review, *Measuring Science Technology*, **7** 449 (1996).

[9] M. E. Smith and E. R. H. van Eck, Recent advances in experimental solid state NMR methodology for half-integer spin quadrupolar nuclei, *Progress in Nuclear Magnetic Resonance Spectroscopy*, **34** 159 (1999).

[10] D. L. Bryce, G. M. Bernard, M. Gee, M. D. Lumsden, K. Eichele and R. E. Wasylishen, Practical aspects of modern routine solid-state multinuclear magnetic resonance spectroscopy: one-dimensional experiments, *Canadian Journal of Analytical Sciences and Spectroscopy*, **46** 46 (2001).

[11] K. J. D. MacKenzie and M. E. Smith, *Multinuclear Solid-state NMR of Inorganic Materials*, Pergamon, Amsterdam, 2002.

[12] E. R. Andrew, L. F. Farnell, M. Firth, T. D. Gledhill and I. Roberts, High-speed rotors for nuclear magnetic resonance studies on solids, *Journal of Magnetic Resonance*, **1** 27 (1969).

[13] A. C. Kunwar, G. L. Turner and E. Oldfield, Solid-State Spin-Echo Fourier Transform NMR of ^{39}K and ^{67}Zn Salts at High Field, *Journal of Magnetic Resonance*, **69** 124 (1986).

[14] D. Massiot, F. Fayon, M. Capron, I. King, S. Le Calvé, B. Alonso, J. O. Durand, B. Bujoli, Z. Gan and G. Hoatson, Modelling one- and two-dimensional solid-state NMR spectra, *Magnetic Resonance in Chemistry*, **40** 70 (2002).

[15] H. Eckert, Structural characterisation of noncrystalline solids and glasses using solid state NMR, *Progress in NMR Spectroscopy*, **24** 159 (1992).

[16] M. E Smith, Recent Progress in Solid-State NMR of Low-γ Nuclei, *Annual Reports on NMR Spectroscopy*, **43** 121 (2001).

[17] T. J. Bastow, M. E. Smith and S. N. Stuart, Observation of Zr-91 NMR in zirconium-based metals and oxides, *Chemical Physics Letters*, **191** 125 (1992).

Chapter 4

Doped zircon pigments

4.1 Introduction

Zircon ($ZrSiO_4$) is a naturally occurring mineral used mainly as a refractory material due to its high resistance to chemical attack, low thermal expansion and high melting point. The main refractory uses of zircon are in the steel industry and in making alumina-zirconia-silica composites[1]. Zircon is also used as the primary source of ZrO_2. ZrO_2 is used as a high strength ceramic in the steel industry and as a milling media. ZrO_2 is also used in pigments and engineering wear components, and is the major component of modern oxygen sensors used widely within the automotive industry. Since it preferentially conducts O^{2-} ions, it is also used in ceramic fuel cells[2] which have the potential to become commercially viable products in the near future[3]. Zircon is also the main source of Hafnium which is present at a level of 1-3%.

Zircon is a co-product of beach sand mining for titanium ores. The biggest producer is Australia which mined 400,000 metric tonnes in 1999[4], followed by South Africa and the United States who produced 219,000 and 118,000 metric tonnes respectively.

The unit cell of zircon is shown in figure 4.1. The structure consists of a chain of edge sharing ZrO_8 dodecahedra and SiO_4 tetrahedra. The space group of the structure is $I4_1/amd$, and this chain extends along the c-axis. The unit cell parameters are $a = b =$ 6.6052 Å, $c = 5.9802$ Å, $\alpha = \beta = \gamma = 90°$[5].

Zircon is a good host material for pigments since it has a high dissolution resistance and tinctorial strength[6]. Once a pigment source has been encapsulated within zircon it

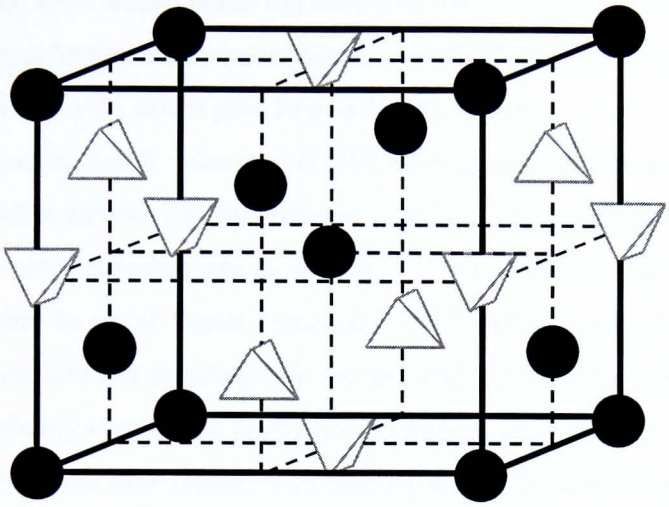

Figure 4.1: The crystal structure of zircon. The tetrahedra represent SiO_4 tetrahedra, and the circles represent zirconium ZrO_8 sites.

is stable to $\sim$ 1200°C[7]. Zircon pigments are typically mixed at a level of 1-5% in a glaze to colour ceramics. When this glaze is fired, the zircon pigment will not interact with it, due to its high melting point and resistance to chemical attack.

In this chapter the effect of doping zircon with Pr, Fe, Cd, Mn and Nb is investigated using solid state ^{29}Si and ^{91}Zr NMR. The most actively studied zircon pigment, vanadium-doped zircon is examined in the next chapter.

4.1.1 Fe-doped zircon

Iron doped zircon is a pink coral coloured pigment which is made by heating equimolar ratios of ZrO_2 and SiO_2 to $\sim$ 1100°C in an airtight crucible in the presence of a Fe source (e.g. $FeSO_4.7H_2O$[8]) and mineralisers (usually NaCl and/or NaF).

There have been a number of studies looking at how the Fe is incorporated into the zircon structure. Berry used a number of techniques to examine zircons with various levels of iron doping[8, 9]. XRD confirmed the presence of an α-Fe_2O_3 (hematite) phase when at least 0.5 wt% Fe was added. ^{57}Fe Mössbauer measurements found a quadrupole split absorption due to Fe^{3+} within the zircon, and a sextet due to α-Fe_2O_3. It also showed a

magnetically ordered α-Fe_2O_3 phase in the < 0.5 wt% sample which was too dilute to be detected by XRD. Fe^{3+} would enter the structure for low concentrations of Fe addition, although the zircon lattice could not accommodate any more Fe^{3+} once Fe addition was > 0.22 wt%, and extra Fe would just form α-Fe_2O_3 regions.

Electron paramagnetic resonance (EPR) experiments were used to try and elucidate Fe^{3+} location within zircon. At concentrations of Fe < 0.2 mol% the Fe^{3+} was found to be in a low symmetry rhombic site as well in α-Fe_2O_3. At concentrations > 0.2 mol%, the Fe^{3+} was found to sit at higher symmetry axial sites as well. On the basis of their unit cell measurements not showing any change with Fe loading, it was concluded that the Fe^{3+} was probably situated in interstitial rhombic and axial sites.

EPR experiments were repeated by Ball[10] where two sites of axial symmetry were found. One was attributed to the dodecahedral ZrO_8 site due to its D_{2d} symmetry and the close match of the two ionic radii (0.078 nm for Fe^{3+} and 0.084 nm for Zr^{4+}[11]). The mechanism for charge compensation was not elucidated, and the nature of the second axial site was also not clear. On the basis of theoretical calculations it was thought unlikely that the second site would be Fe^{3+} substituting into the smaller Si^{4+} tetrahedra whose ionic radius is 0.040 nm.

Recent Mössbauer refinements on variable Fe-content zircons suggest that at low concentrations, Fe is mainly present as Fe^{3+} at the ZrO_8 site[12]. This was from the observation of a doublet in the spectra. This doublet was then dominated by a sextet which appears at $\sim$ 3% Fe content, and gets larger with additional Fe addition. This sextet was attributed as before, to magnetic $\alpha-Fe_2O_3$ forming a phase separated mixture with the Fe-$ZrSiO_4$. These results were supported by their XRD measurements which showed a decrease in the unit cell parameters of $ZrSiO_4$ with increasing Fe addition.

Berry[8], Ball[10], Tartaj[13] and Llusar[14] are all in agreement that the origin of the coral colour is dominated by the amount of α-Fe_2O_3 present within the pigment.

4.1.2 Pr-doped zircon

Praseodymium-doped zircon forms a strong yellow colour and was first developed in 1952 by Fujii and Sono[15]. It is made using a similar route to Fe-$ZrSiO_4$ except the Fe source is replaced with a Pr source, usually Pr_6O_{11}[16].

In common with Fe-doped zircon, there has been a lot of research into how the Pr is accommodated within the pigment, and how the colour can be optimised using the minimum amount of Pr source. One of the first studies was by Harris who used EPR to find six widely spaced hyperfine lines[17]. These lines were independent of crystal orientation, and on the basis of hyperfine field calculations it was shown that the lines were due to Pr^{4+} within the zircon. No comment on the nature of the site of the Pr^{4+} could be made.

Stiebler then applied XRD and diffuse reflection measurements to the problem[18]. XRD measurements performed on undoped and Pr-doped zircon showed no increase in the size of the unit cell when Pr was added. This is inconsistent with Pr^{4+} substitution into the structure at ZrO_8 or SiO_4 sites. Diffuse reflection measurements[18] only showed Pr^{3+} present, and the yellow colour of the pigment was attributed to the presence of this Pr^{3+} in the structure along with the charge compensation mechanisms that accompany it. On the basis of this data it was not possible to elucidate the location of the Pr^{3+} within the zircon.

More recently, Ocaña has conducted two studies on the Pr-$ZrSiO_4$ system. In the first, various X-ray diffraction spectroscopies were used to investigate the site of Pr ions within the pigment[19]. XRD measurements indicated an increase in unit cell size when the zircon was doped with Pr, and along with L_{III} edge XANES measurements it was concluded that Pr^{4+} was present. Examination of the EXAFS area of XAS spectra found that the oscillation could be fit best using one 8-fold coordinated site with oxygens a distance of 2.13 Å and 2.30 Å from the Pr^{4+}. This indicated that the Pr^{4+} had substituted at ZrO_8 dodecahedra. Furthermore, XPS surface measurements gave the Pr/$ZrSiO_4$ ratio to be 4% which indicated preferential enrichment of Pr in the outer layers of zircon particles.

In the second study, the effect of NaF addition as a mineraliser when synthesising Pr-$ZrSiO_4$ was concentrated upon[16]. Using ESR measurements, only six lines due to Pr^{4+} could be observed when NaF was used in the starting mixture. When NaF was not included, L_{III} edge XANES found only Pr^{3+}, and using XRD phase measurements it was concluded that this was in $Pr_2Zr_2O_7$, not Pr^{3+} within the zircon itself. XRD measurements only showed an increase in unit cell size when NaF was added and Pr^{4+}

was present. The conclusions of this study were that NaF decreases the temperature for zircon formation, and at that lower temperature Pr^{4+} is stable.

Hill also conducted a recent study into the effects of different processing variables on the final colour of pigment formed[20]. It was found that the temperature the sample was fired at, and the mineraliser content of the recipe were the most important factors when producing the pigment, and the colour was independent of the particle size of the ZrO_2 used.

4.2 Zircon reference samples

Figure 4.2 shows the ^{29}Si spectra of the two zircon heat treatments. It also shows the spectra of two naturally occurring zircons mined in the Ukraine (zircon 1 and zircon 2). The spectra were acquired on a Bruker MSL-300 spectrometer using a Bruker 7 mm double bearing MAS probe. The samples were spun to at least 3.5 kHz, and a 2.5 μs pulse was used to induce a magnetisation tip of $\pi/6$. A recycle delay of 60 s ensured the ^{29}Si signal was fully relaxed.

The sharp peak at -81.8 ppm in the Ukraine zircons and the 1060°C sample is at the well known zircon position[21]. There is only one line, consistent with there being only one inequivalent silicon site in the unit cell. This resonance is not present for the sample heated to 860°C since that was not hot enough for zircon to form.

All samples were weighed after ^{29}Si measurements. Since the composition of the synthetic zircons were known, and assuming that the natural zircons are 100% $ZrSiO_4$, the number of silicon nuclei present for each experiment could be calculated as is outlined in section 3.4.2. This allowed scaling of the integrated intensities so they can be compared quantitatively. The whole spectrum integrals for zircon 1 and zircon 2 gave 61% and 55% the amount of ^{29}Si signal that Z1 produced, which is because it was assumed that the zircons were a pure $ZrSiO_4$ phase. It is not uncommon for naturally occurring zircon to contain radioactive impurities, for example ^{238}U, ^{235}U or ^{232}Th. These substitute into the dodecahedral zirconium site, and when these nuclei undergo α-decay, the recoil energy from the radioactive nucleus creates a localised area of glassy material within the zircon[22, 23]. This ability of zircon to efficiently contain radioactive decays has led to

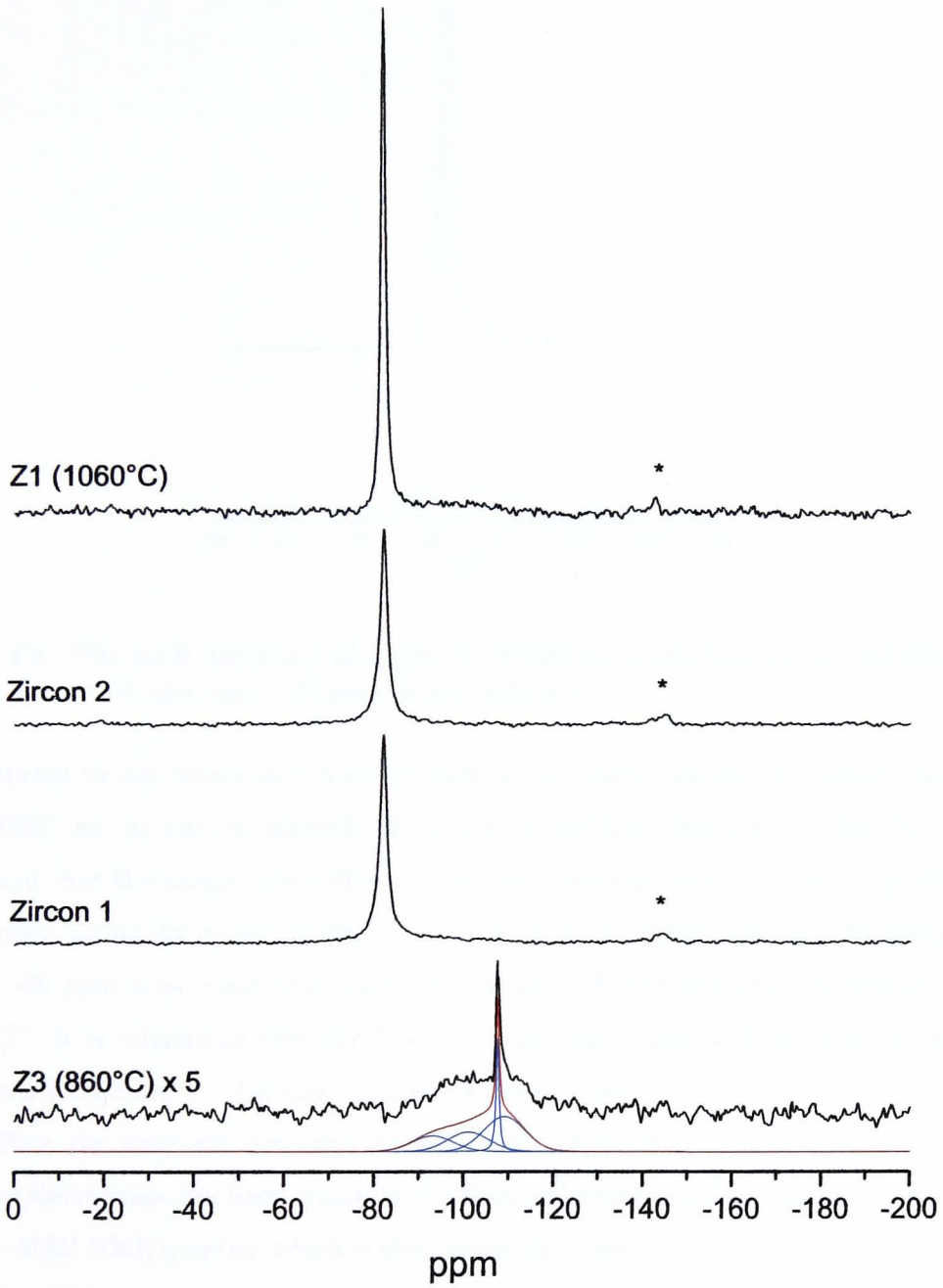

Figure 4.2: ^{29}Si spectra of two naturally occurring zircons (zircon 1 and zircon 2) and two synthetic samples (Z1 and Z3) heated to 1060°C and 860°C. All spectra are scaled to show the relative amount of signal measured, however Z3 has been enlarged for clarity. The results of peak fitting are in table 4.1.

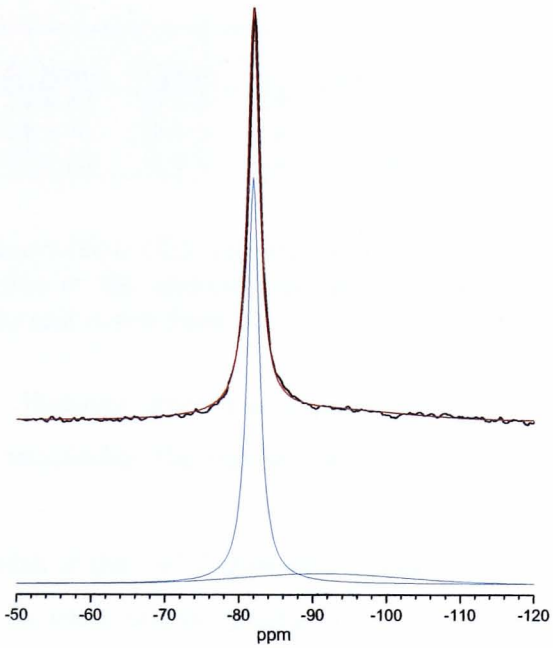

Figure 4.3: ^{29}Si MAS spectrum of zircon 2. Fitted to it are Lorentzian and Gaussian lineshapes at -82 ppm and -86 ppm in the ratio 4:1.

the proposal to use zircon as a host for radioactive waste. Farnan has shown that ^{29}Si MAS NMR can be used to quantify the extent of radiation damage in zircon[24, 25]. It was found that the normal crystalline zircon phase appears as a Lorentzian lineshape at -81.6 ppm, whilst the glassy radiation damaged phase manifests itself as a Gaussian peak in the -86 ppm area, consistent with the average polymerisation in amorphised zircon being Q^2. It is interesting that the ^{29}Si spectrum here allows a distinction to be made between a disordered crystal and a genuinely glassy solid.

Both the naturally occurring zircons have suffered from α-decay damage and the extent of the damage has been quantified by fitting Gaussian and Lorentzian lineshapes to the ^{29}Si MAS NMR spectra, which is demonstrated in figure 4.3. The fitting of the broad Gaussian component was very sensitive to the phasing of the spectra, and the phasing was refined to optimise the fit and appearance of the baseline.

The CSA parameters were calculated by fitting lines to the spinning sidebands present in the spectra, and the results of this fitting are listed in table 4.1. A more accurate fit could be achieved by spinning the sample slower and using the extra sidebands

	Lorentzian					Gaussian		
Sample	δ_{iso} (ppm)	Δ (ppm)	Ω (ppm)	κ	Ratio	δ_{iso} (ppm)	Δ (ppm)	Ratio
Z1	-81.7 ± 0.2	1.2 ± 0.1	43 ± 4	-1.0				
zircon1	-81.9 ± 0.2	1.9 ± 0.1	50 ± 4	-1.0	$79 \pm 5\%$	-89.7 ± 1.0	32 ± 2	$21 \pm 5\%$
zircon2	-81.9 ± 0.2	2.0 ± 0.1	44 ± 4	-1.0	$83 \pm 5\%$	-93.4 ± 1.0	111 ± 4	$17 \pm 5\%$

Table 4.1: Results of Lorentzian CSA spinning sideband manifold and single Gaussian fitting to the ^{29}Si spectra of the undoped zircons in figure 4.2. Δ is the width of a resonance at half height, and κ was fixed at -1.

to further refine the fit. However, since it is assumed that $\kappa = -1$ due to the tetragonal symmetry at the SiO_4 tetrahedra, the one sideband was sufficient to get an idea of the CSA.

The increased width of the -81.7 ppm zircon peak for the natural samples shows a greater dispersion than for the synthetic sample. This indicates a wider range of isotropic values, and hence a wider range of local environments. Factors which control this local environment include atomic disorder and defects. The effect of atomic disorder and defects mean that the electron density at the silicon site can vary, and hence the chemical shift. Silicate ^{29}Si chemical shifts are known to be sensitive to Si-O-Si bond angles[21, 26], so a distribution in Si-O-Zr bond angles due to a nearby distortion could induce this broadening, although the higher ionicity of the O-Zr bond would greatly reduce this effect. The resonance can also be broadened by substitution of radioactive nuclei for next nearest neighbour zirconia atoms, distorting the ZrO_8 dodecahedra. In natural samples it should be remembered that paramagnetic impurities can also cause broadening as well as structural effects.

Although no zircon has formed in Z3 where the firing temperature was too low, zircon can form at 860°C when a vanadium pigment is added to the reactants, since the pigment source also acts as a fluxing agent. The ^{29}Si MAS spectrum of Z3 shows a peak at -107.5 ppm which is due to unreacted SiO_2 as crystalline quartz[27]. The broad peak centred at -105 ppm can be fitted using three Gaussians of width 11 ppm at positions of -93, -101 and -109 ppm. These correspond to Q^2, Q^3 and Q^4 silicate species and are are fitted in the ratio 20:24:43:15, the final number being the integral of the Lorentzian line used to fit the quartz phase.

On the basis of these four spectra, sample Z1 (the crystalline zircon sample heated

Figure 4.4: The five PV samples after firing. The leftmost crucible (PV1) has 25% the optimum amount of pigment, increasing in steps of 25% to the furthest right where 125% pigment source has been added (PV5).

to 1060°C) was chosen as a signal reference source. This is used in later experiments to measure how much ^{29}Si signal is being measured from doped zircon pigments, and how much is being screened by paramagnetic species within the samples.

4.3 Pr-doped zircons

Figure 4.4 shows the visual appearance of the five PV series of samples where the amount of Pr_6O_{11} in the starting recipe was varied from 25% to 125% of the commercially used quantity.

Before the ^{29}Si spectra of the Pr-doped zircon pigments could be interpreted, the effect of any paramagnetic Pr species on the ^{29}Si signal needed to be evaluated. ^{29}Si spectra were acquired in the same manner as for the undoped zircons. A 30° pulse was used with a 60 s recycle period to ensure minimal signal saturation occurred. The samples were spun in the Bruker 7 mm DB probe at 5 kHz, and were weighed after acquisition so the ^{29}Si signal measured could be compared with the undoped zircon reference to quantify signal screening.

The results of the signal quantification are displayed in figure 4.5. Sample PT1 has been omitted since it was not held at temperature long enough for zircon to form. The furnace started ramping down from temperature when the temperature within the furnace arrived at 1060°C. Although the reaction is relatively quick, only the air within the furnace reached 1060°C momentarily, and the temperature of the reactants within the crucible would have been lower due to the time it takes for heat to conduct through the crucible into the mixture.

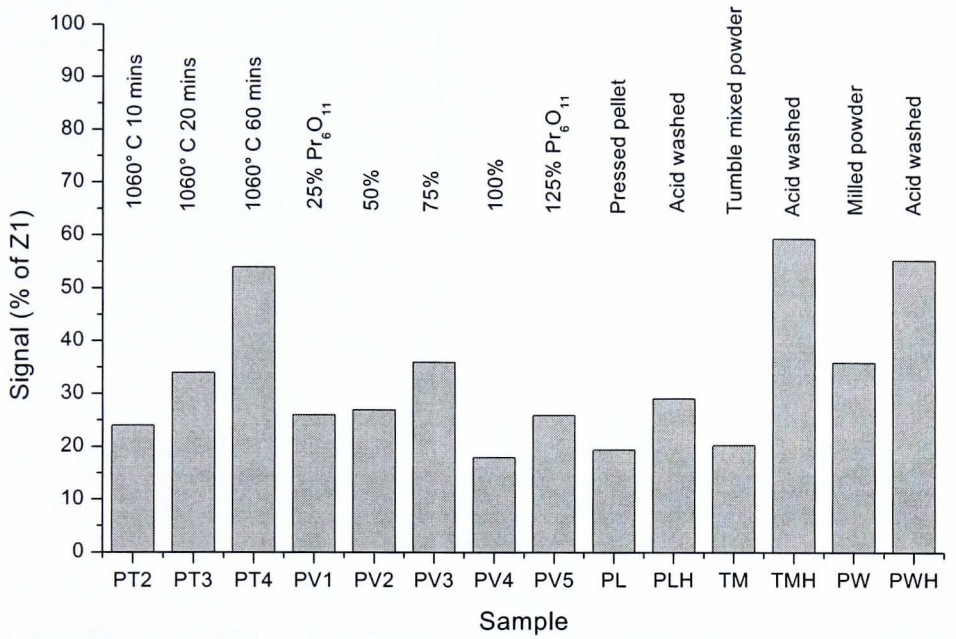

Figure 4.5: The absolute signal measured (see section 3.4.2) for the variable firing time Pr-$ZrSiO_4$ (PT) samples, the variable Pr content Pr-$ZrSiO_4$ (PV) samples and the Fe-doped zircons. The signal has been normalised with respect to the undoped synthetic zircon sample Z1.

The amount of signal being masked by the praseodymium in the zircon is as much as 75% in PT2. This means that since so much signal is not being detected, only limited comment can be made about the system. The low amount of signal observed suggests that an efficient hyperfine coupling mechanism is occurring. If the Pr is present as Pr^{3+} within another phase as was suggested by Stiebler[18], then the through space dipolar interaction would be needed to mask out the signal. However, if it is present as Pr^{4+} at ZrO_8 sites, then a Fermi through bond effect will dominate which is likely to be a more efficient signal screening mechanism. So on the basis of the large loss of ^{29}Si signal measured, Pr existing as doped Pr^{4+} within zircon is more likely, however this cannot rule out the possibility of Pr also existing as a separate phase.

The amount of signal observed increases with firing time. Samples PT2-4 were fired at 1060°C for 10, 20 and 60 mins, and twice the signal is observed after 60 mins compared to 10. This supports the Pr^{4+} doping mechanism since it has been found that when a

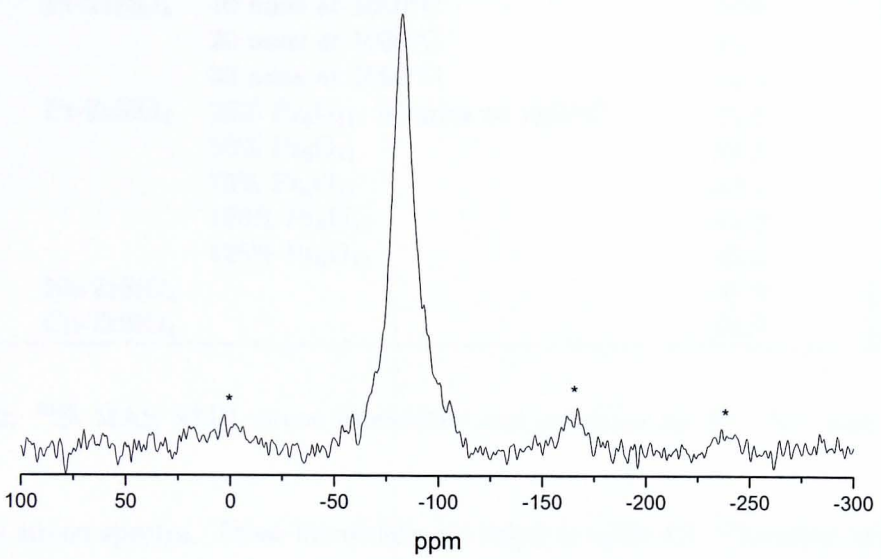

Figure 4.6: ^{29}Si MAS NMR of Pr-$ZrSiO_4$ (PT4). Only 54% of the expected ^{29}Si signal is seen, so other resonances may have been screened beyond detection.

doped zircon pigment, where the colouring site has substituted into the zircon lattice undergoes prolonged heating, the colour fades as the colouring site is expelled from the zircon[28]. This reduction of the amount of Pr^{4+} in the zircon causes reduced screening of the ^{29}Si signal, so more signal is measured.

The variation of signal measured with Pr source in the starting mixture (the PV samples) shows that the amount of Pr^{4+} entering the structure is largely independent of the starting mixture. However, the least signal is seen when the optimum amount of Pr source is used in PV4. This is the mixture which gives the best pigment colour so it is likely to contain the most Pr^{4+}.

The ^{29}Si MAS NMR spectrum of the Pr-$ZrSiO_4$ sample giving the most signal (PT4) is shown in figure 4.6. The zircon resonance is still observable at -82 ppm although it is much broader due to the hyperfine interaction between the probe ^{29}Si nuclei and the unpaired electron of the Pr^{4+}. There are more spinning sidebands present in this spectra compared with those of the undoped zircons in figure 4.2, so the static linewidth of these impurity-doped samples has increased.

The linewidth at half height (Δ) of the main resonance has been measured for all

Sample	Doping	Preparation	δ_{iso} (ppm) ± 0.4	Δ (ppm)
PT2	Pr-$ZrSiO_4$	10 mins at 1060°C	-83.6	8 ± 1.0
PT3		20 mins at 1060°C	-84.0	11 ± 1.5
PT4		30 mins at 1060°C	-84.5	8 ± 1
PV1	Pr-$ZrSiO_4$	25% Pr_6O_{11}, 20 mins at 1060°C	-81.8	9 ± 1
PV2		50% Pr_6O_{11}	-82.1	11 ± 2
PV3		75% Pr_6O_{11}	-82.1	22 ± 2
PV4		100% Pr_6O_{11}	-81.3	14 ± 2
PV5		125% Pr_6O_{11}	-82.2	12 ± 2
NB1	Nb-$ZrSiO_4$		-81.9	1.4 ± 0.3
CD1	Cd-$ZrSiO_4$		-81.9	1.2 ± 0.3

Table 4.2: ^{29}Si MAS NMR zircon linewidths and positions for Pr-, Nb- and Cd-doped zircons.

Pr-doped zircon spectra. These linewidths are listed in table 4.2. The effect of prolonged heating does not appear to significantly change the width of the zircon resonance. The linewidth does vary when the amount of Pr_6O_{11} source used in the starting recipe is changed, and reaches a maximum when 75% the optimum amount of Pr_6O_{11} is added. Sample PV4 was prepared under the same conditions as PT3 since the recipes and firing times for both samples are identical. The measured linewidth for the two samples is the same within experimental error.

4.4 Fe-doped zircon

Three Fe-doped coral zircon pigments were prepared using the commercial Fe-$ZrSiO_4$ recipe. The starting mixtures were either mixed in a turbular mixer, mixed in a ceramic ball mill or pressed into a pellet. After firing, a portion of each sample was acid washed to remove as much excess Fe as possible.

^{29}Si NMR measurements were performed in the same manner as for the Pr-doped and undoped zircons. A 30° pulse was used with a 60 s recycle delay whilst the sample was spinning at 4.5 kHz in a Bruker 7 mm DB probe.

Figure 4.5 shows the amount of ^{29}Si NMR signal measured from the Fe-doped samples compared to the undoped reference zircon. There has been signal loss in all six samples which is likely to be screening by iron present within the sample as a soluble

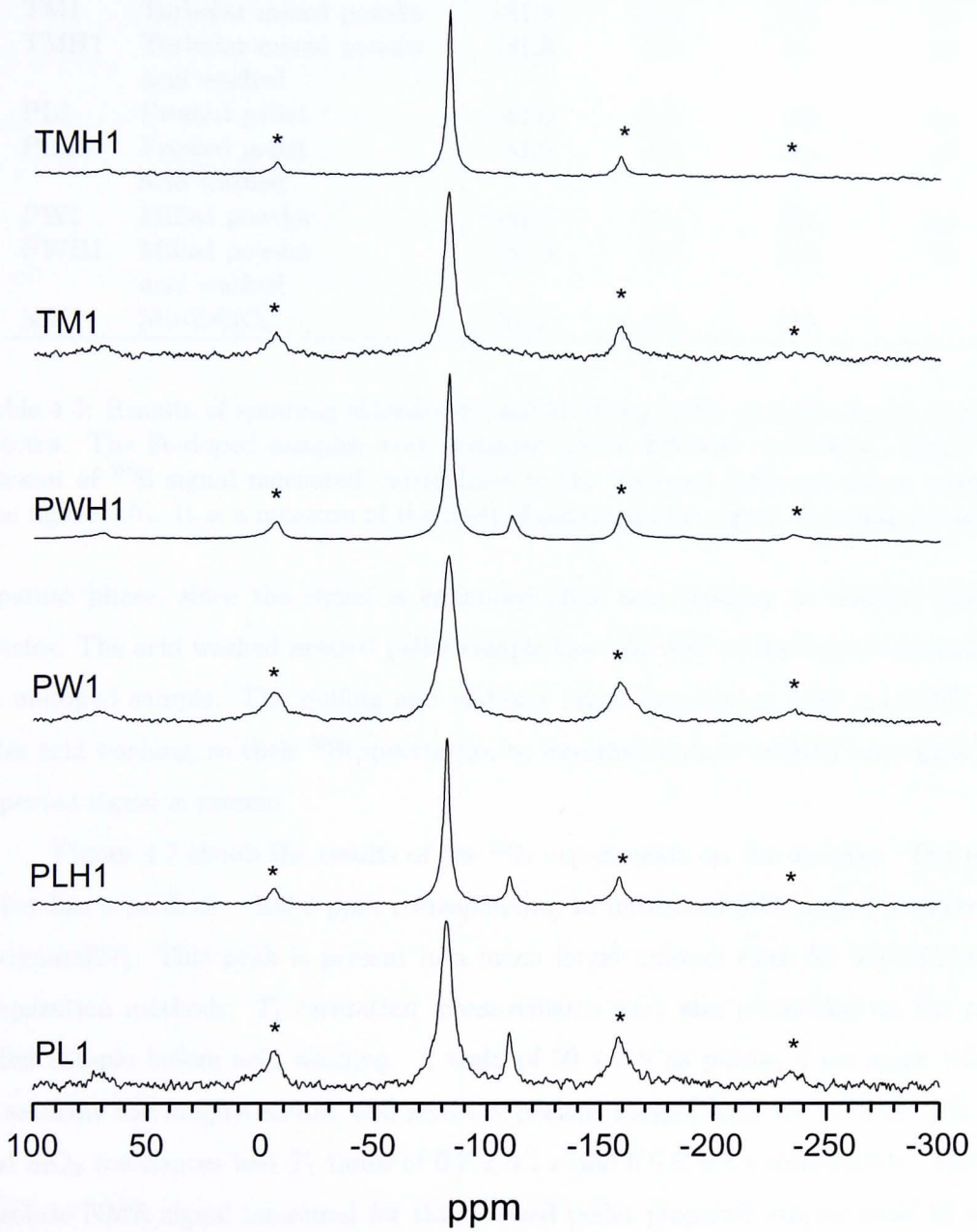

Figure 4.7: ^{29}Si MAS spectra of iron-doped zircons made using three preparation methods (PL1 was fired as a pressed pellet, TM1 was mixed in a turbular mixer and PW1 was milled before firing). The three samples have also been acid washed (PLH1, TMH1, and PWH1).

Sample	Preparation	δ_{iso} (ppm) ±0.4	Δ (ppm) ±0.3	Ω (ppm) ±15	Signal (%) ±10
TM1	Turbular mixed powder	−81.9	5.5	138	20
TMH1	Turbular mixed powder acid washed	−81.6	2.9	91	59
PL1	Pressed pellet	−81.6	6.8	159	19
PLH1	Pressed pellet acid washed	−81.9	3.3	113	29
PW1	Milled powder	−81.6	7.4	151	36
PWH1	Milled powder acid washed	−81.9	3.7	118	56
MN1	Mn-$ZrSiO_4$	-81.3	1.8	113	

Table 4.3: Results of spinning sideband manifold fitting to Fe- and Mn-doped zircon ^{29}Si spectra. The Fe-doped samples were prepared under different conditions. Signal is the amount of ^{29}Si signal measured, normalised to the undoped reference zircon sample Z1 (see figure 4.5). It is a measure of the level of paramagnetic signal screening present.

separate phase, since the signal is enhanced after acid washing to remove these iron species. The acid washed pressed pellet sample has only 30% of the signal expected from an undoped sample. The milling and turbular mixer approaches both have 60% signal after acid washing, so their ^{29}Si spectra can be interpreted more reliably since most of the expected signal is present.

Figure 4.7 shows the results of the ^{29}Si experiments on the samples. The pressed pellet has a peak at −109.8 ppm corresponding to unreacted SiO_2 which is likely to be tridymite[27]. This peak is present in a much larger amount than for any of the other preparation methods. T_1 saturation measurements were also performed on the pressed pellet sample before acid washing. A train of 50 × 3.0 μs pulses, 4 ms apart was used to saturate the magnetisation, and recovery periods ranged from 0.1 to 60 s. The zircon and SiO_2 resonances had T_1 times of 0.2 ± 0.1 s and 6.0 ± 0.4 s respectively. The small absolute NMR signal measured for this pressed pellet prepared sample must be mainly due to paramagnetic broadening since the $4 \times T_1$ times of the two resonances observed are far shorter than the 60 s pulse delay used.

All the zircon resonances consist of many more spinning sidebands in these spectra compared to the normal crystalline zircons examined in figure 4.2. This is due to the paramagnetic Fe increasing the intensity of the sidebands through a paramagnetic effect,

and ^{27}Al studies on kaolinite containing a secondary Fe^{3+} containing phase have also shown an increase in spinning sideband intensities when more Fe^{3+} phase was present[29, 30]. ^{29}Si NMR has also shown a correlation between spinning sideband manifold intensity and the presence of Fe within muscovite samples[31].

In order to quantify the paramagnetic broadening, a set of spinning sidebands were fitted to each spectrum with a span Ω (equivalent to that for the CSA interaction) which could be used as a measure of the extent of the spinning sideband manifold. The results of this fitting are listed in table 4.3, although the values of the skew κ used to fit the spectra are not listed. This is because the CSA interaction is not the dominant effect causing the extra sideband intensity, so κ has no real equivalent here. The fitting of a set of interaction sidebands is only being used as a consistent method for quantifying the width of the sideband manifold.

Table 4.3 shows that as well as as the absolute signal changing when iron has been washed out of the sample, Ω and Δ are reduced as well. Ω is reduced by typically $30 - 50$ ppm by the removal of iron, but is still at least twice the value of $40 - 50$ ppm expected for an undoped zircon (table 4.1). This, along with the signal measurements and the colour of the sample indicates that there is still iron left within the sample. The removal of some paramagnetic Fe does reduce Ω and Δ since the net hyperfine effect of the remaining Fe is smaller.

The linewidths Δ of the main zircon resonances are much smaller than those seen for Pr-$ZrSiO_4$, where the doping mechanism is thought to be local substitution of Pr^{4+} at ZrO_8 sites. This, and the increased sideband intensities observed suggest that the presence of paramagnetic iron is likely to be as Fe^{3+} in an α-Fe_2O_3 phase, consistent with Berry's findings[8, 9].

It can also be concluded that the least efficient preparation method is using a pressed pellet since the ^{29}Si NMR shows unreacted SiO_2 is present. This is likely to be because gaseous SiF_4 is required to form zircon which can diffuse more freely in the milled and turbular mixed powders, than in the pressed pellet. Prior to acid washing, the turbular mixed powder gave the least signal and is likely to be more efficient at incorporating Fe into the sample. After acid washing, the turbular mixed and milled powders give very similar signals, so the amount of Fe remaining in these samples is likely

to be similar.

4.5 Nb-, Mn- and Cd-doped zircon

Nb- and Mn-doped zircon pigments which are not in large scale production commercially were also examined using ^{29}Si MAS NMR. Nb-doped zircon is a yellow colour, and Mn-doped zircon is purple in colour. Cd-doped zircon which is produced commercially is a yellow/red colour, and was also examined.

Nb-doped zircon was synthesised using the usual mixture of ZrO_2, SiO_2, NaF and NbO_2 as the pigment source. This was fired at 1060°C in an airtight crucible.

The Mn-doped pigment was created using $MnCO_3$ as the pigment source and the mixture was fired at 1060°C, again in a closed crucible. The only research published on this pigment is by Kato who looked at the best mixture of Mn-, Pr- and Fe-doped zircons to give a red colour[32]. It was found that a mixture of 8:1:1 Mn:Pr:Fe-$ZrSiO_4$ gave the reddest colour.

Cd-doped zircon is produced by mixing ZrO_2, SiO_2 with CdS. This is then heated to 950°C in the presence of mineralisers, and a fraction of the CdS is encapsulated within the zircon to create a yellow colour. If CdSeS is used instead of CdS, a red pigment is created[33]. Since the colour of the pigment can vary slightly from one batch to the next when produced on a large scale, SiO_2 is usually added in varying amounts to dilute the pigment so that it appears to be the standard colour.

Figure 4.8 shows the ^{29}Si MAS NMR spectra of the three doped zircon samples which were acquired under the same conditions as for the Pr- and Fe-doped zircons. The chemical shift and linewidth of the main zircon resonances are listed in table 4.2. Unreacted SiO_2 can be seen at -109 ppm in all the pigment spectra which could be due to a number of reasons. The Mn- and Nb-doped pigments have not been optimised for large scale production yet, so the ZrO_2:SiO_2:colour source ratio may not be the optimum. The reactants may not be mixed thoroughly enough, or may not have been heated long enough at a high enough temperature. X-ray diffraction of the three samples confirms that zircon is the main phase present. The Cd-doped zircon analysed is a production sample of the pigment, and the SiO_2 peak in the ^{29}Si spectrum is likely to be due to the

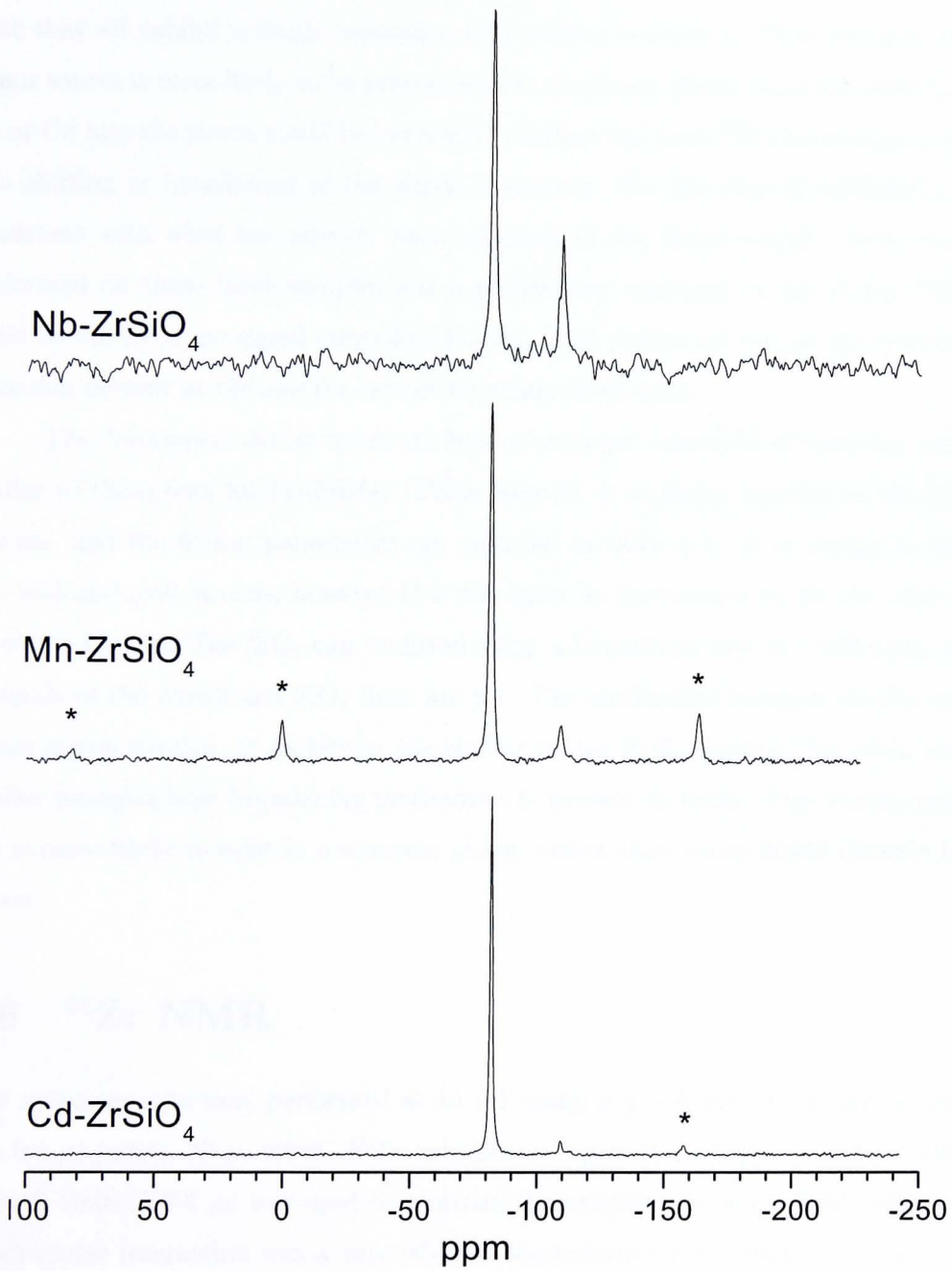

Figure 4.8: ^{29}Si MAS NMR at 4.5 kHz of zircon doped with Nb, Mn and Cd.

deliberate addition of SiO_2 to produce a standard colour.

The Nb- and Cd-doped zircons show the normal zircon resonance. There appear to be no differences between these spectra, and the undoped zircon spectra in figure 4.2, since they all exhibit a single resonance with similar linewidths. This indicates that the colour source is more likely to be present within a separate phase, since the substitution of Nb or Cd into the zircon could be expected to distort the local ^{29}Si environment, resulting in a shifting or broadening of the zircon resonance. For the case of Cd-$ZrSiO_4$, this is consistent with what has already been reported in the literature[33]. Since the NMR performed on these three samples was a preliminary approach to see if any ^{29}Si signal could be observed, no signal quantification has been performed yet, so the level of signal screening present in the spectra cannot be commented upon.

The Mn-doped zircon spectrum has an enlarged manifold of spinning sidebands similar to those seen for Fe-$ZrSiO_4$. These were fit in a similar manner to the Fe-doped spectra, and the fitting parameters are reported in table 4.3. Δ is similar to the Nb-, Cd- and undoped zircons, however Ω is the same as has been seen for the acid washed Fe-doped zircons. The SiO_2 can be fitted using a Lorentzian line at -109 ppm, and the integrals of the zircon and SiO_2 lines are 9:1. The similarities between the Fe- and Mn-doped zircon spectra, in particular the similar values of Ω measured for both, suggest a similar paramagnetic broadening mechanism is present in both. This would mean that Mn is more likely to exist in a separate phase, rather than being doped directly into the zircon.

4.6 ^{91}Zr NMR

^{91}Zr measurements were performed at 14.1 T using a $\frac{\pi}{2} - \frac{\pi}{2}$ echo sequence consisting of two 0.4 μs pulses, 50 μs apart. Echo acquisition begun 10 μs after the second pulse and a dwell time of 0.4 μs was used to measure frequencies over a 2.5 MHz window. The quadrupolar interaction was a very efficient mechanism for T_1 relaxation, and a recycle delay of 0.1 ms was used which allowed 1.5×10^6 transients to be summed over a weekend.

Figure 4.9 shows the static ^{91}Zr NMR performed on four doped zircons. All the lineshapes measured for the different dopants show a characteristic second-order quadrupolar

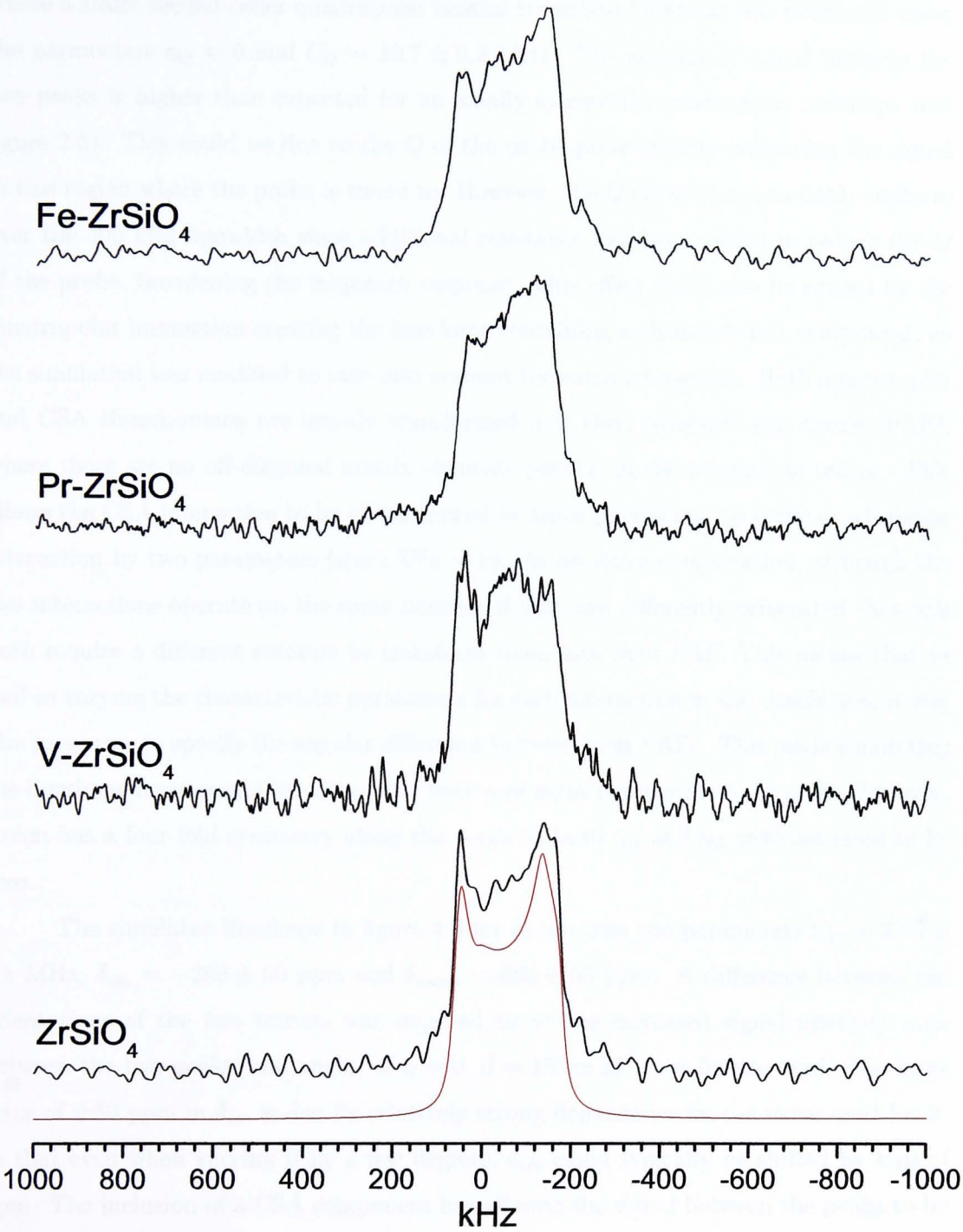

Figure 4.9: ^{91}Zr static spectra at 14.1 T of four doped zircon pigments.

lineshape of the central transition. Fitting was only attempted for the undoped zircon where a static second-order quadrupolar central transition lineshape was simulated using the parameters $\eta_Q = 0$ and $C_Q = 19.7 \pm 0.2$ MHz. The amount of signal between the two peaks is higher than expected for an axially symmetric quadrupolar lineshape (see figure 2.5). This could be due to the Q of the probe preferentially enhancing the signal in this region where the probe is tuned to. However, the Q should be reasonably uniform over the 300 kHz linewidth since additional resistance had been added to reduce the Q of the probe, broadening the frequency response. This effect could also be caused by the quadrupolar interaction creating the lineshape containing a chemical shift component, so the simulation was modified to take into account the extra interaction. Both quadrupolar and CSA Hamiltonians are usually transformed into their principle axis frame (PAF), where there are no off-diagonal matrix elements present in the interaction tensor. This allows the CSA interaction to be characterised by three parameters, and the quadrupolar interaction by two parameters (since $\nabla^2\phi = 0$). As an extra complication, although the two interactions operate on the same nucleus, if they are differently orientated they will both require a different rotation to transform them into their PAF. This means that as well as varying the characteristic parameters for each interaction in the simulation, it was also necessary to specify the angular difference between their PAFs. This made simulating the lineshape more complicated as there were now eight parameters to fit with. However, zircon has a four fold symmetry along the c-axis so both η_{cs} and η_Q were assumed to be zero.

The simulated lineshape in figure 4.9 for zircon uses the parameters $C_Q = 20.5 \pm 0.1$ MHz, $\delta_{iso} = -260 \pm 50$ ppm and $\delta_{aniso} = 680 \pm 50$ ppm. A difference between the orientations of the two tensors was required to fit the increased signal intensity area between the two peaks, and angles of $\alpha = 0$, $\beta = 152 \pm 20°$, $\gamma = 0$ were used. The large error of ± 50 ppm in δ_{iso} is due its relatively strong dependence on the value used for β, so that even when varying β by a few degrees, δ_{iso} could typically be shifted by tens of ppm. The inclusion of a CSA component has allowed the signal between the peaks to be fitted better, and also allowed the intensities of the two peaks to be better fitted, since a purely axially symmetric quadrupolar lineshape has a more intense singularity to more negative ppm.

Bond	Wyckoff (1927) [36]	Krstanović (1958) [37]	Gibbs (1971) [38]	Siggel (1990) [5]
Zr - O	4×2.05Å	4×2.15Å	$4 \times 2.131 \pm 0.001$Å	4×2.129Å
	4×2.41Å	4×2.31Å	$4 \times 2.268 \pm 0.001$Å	4×2.269Å
Si - O	4×1.61Å	4×1.62Å	$4 \times 1.622 \pm 0.001$Å	4×1.622Å

Table 4.4: Zr-O and Si-O bondlength refinements in $ZrSiO_4$.

Bastow has performed ^{91}Zr NMR on a single crystal of zircon for a range of rotations about the [100]-axis[34]. By fitting the rotation pattern of the shift of the central transition resonance with crystal orientation, $C_Q = 20.47$ MHz and $\delta_{aniso} = -169$ ppm were calculated. The discrepancy between Bastow's measurements of δ_{iso} and δ_{aniso}, and those simulated here could lie in the the assumption that the two tensors are not coincident.

A perturbed angular correlations study has also been performed by Rubio-Puzzo where it was found that $C_Q = 16.1$ MHz[35]. η_Q was found to be 0.21, despite the symmetry of the structure. This non-zero η_Q was explained using Wyckoff's crystallographic measurements from 1927[36] where the oxygens about the Zr site form a highly distorted cube with four oxygens 2.41Å from the Zr, and four 2.05Å away. However, these values have been refined since to a less distorted cube and the refinements are listed in table 4.4.

NMR and PACS do not appear to be complementary techniques for measuring quadrupolar effects in zircon. Whilst it is known that ^{180}Hf behaves in a very similar manner to ^{91}Zr, the PACS technique is observing the $\gamma - \gamma$ cascade generated by ^{181}Ta. If this probe nucleus distorts the ZrO_8 dodecahedral site, the electric field gradient experienced by it will not be the same as that experienced by ^{91}Zr, and a different quadrupolar coupling will be measured. However, PACS was able to elucidate more than one ^{181}Ta site whereas ^{91}Zr NMR at 14.1 T does not offer the resolution needed to observe more than one resonance in these doped zircons. Higher fields will help this problem and novel new pulse techniques, for example QCPMG spikelet spectra[39] might also be able to provide extra resolution.

4.7 Conclusions

The ^{29}Si MAS NMR spectra of the synthetic and naturally occurring zircons in figure 4.2 show that the synthetic sample gives significantly more signal than the radiation damaged

zircons. This is partly due to the difficulty in accurately integrating the broad amorphous peak in the radiation damaged samples. It is also partly due to the likelihood of contaminants being present in the natural samples which will cause the signal integration measurements to underestimate the ^{29}Si signal given measured. Another possible contribution to the signal loss could be from the presence of small quantities of paramagnetic radioactive impurities in the naturally occurring samples.

The main zircon resonance in the spectra of the Fe-doped zircons is typically a factor of $\times 50$ broader than for the undoped zircons. This, and the enlargement of the manifold of spinning sidebands giving rise to larger values of Ω, is a strong indication that a dipolar, through-space paramagnetic interaction is present between paramagnetic Fe sites and probe ^{29}Si nuclei. This is likely to be caused by Fe mixing into the zircon as a separate $\alpha-Fe_2O_3$ phase. Similar broadening effects have been observed previously in ^{29}Si spectra of other silicates containing Fe_2O_3[29-31]. This doping mechanism is consistent with the mechanism suggested by Berry [8, 9].

When different sample preparation procedures are employed to synthesise Fe-$ZrSiO_4$, the turbular mixing approach produces a sample which yields the least ^{29}Si signal. Since XRD measurements indicate only a single zircon phase, this preparation method is likely to be the most efficient at incorporating $\alpha-Fe_2O_3$ into the pigment, since paramagnetic signal screening is at the highest.

Comparison between the ^{29}Si spectra for the undoped reference zircons, and the Pr-doped zircons indicate that for all Pr-doped zircons, a large proportion of potential ^{29}Si signal is being screened. This is likely to be because Pr^{4+} is doping directly into ZrO_8 sites in zircon, although is too large an atom to be able to dope into the smaller SiO_4 sites. Pr^{4+} has a large magnetic moment, and a Fermi through-bond interaction between Pr^{4+} and ^{29}Si nuclei is likely to be causing the substantial line broadening. The spectra measured do not suggest that Pr^{3+} could be present in an extra phase, since any broadening would be through a dipolar interaction. This would not screen the signal as efficiently as the Fermi contact interaction associated with Pr^{4+} doping.

Limited comment can be made on the Nb- and Cd-dopings, since ^{29}Si zircon resonance line broadening or spinning sideband broadening was not observed. T_1 and signal quantification measurements on these two samples could be used to investigate whether

any interaction between pigment and ^{29}Si nuclei is present. The Mn-doped sample displays an increased spinning sideband manifold similar to that observed for Fe-$ZrSiO_4$, however the zircon resonance was not broadened to the same extent as the Fe-$ZrSiO_4$ resonance. This indicates that the Mn pigment is more likely to exist in a separate phase which is very well mixed with the zircon. ^{29}Si NMR on the Mn- and Nb-doped zircons shows that the pigment preparation has not been optimised since unreacted SiO_2 is observed.

References

[1] P. Chandley, The synthesis and spectroscopy of doped zircon and other lattices, *PhD Thesis*, Univeristy College London, 1991.

[2] S. P. S. Badwal and K. Foger, Solid Oxide Electrolyte Fuel Cell Review, *Ceramics International*, **22** 257 (1996).

[3] K. Kendall, Fuel cells eye up the mainstream market, *Physics World*, **15** 30 (2002).

[4] J. B. Henrick, Zirconium and Hafnium, *U.S. Geological Survey, Mineral Commodity Summaries*, 191, Januray 2002.

[5] A. Siggel and M. Jansen, Positions of dopant rare-earth and vanadium in zirconia pigments - an X-ray investigation, *Zeitschrift fur Anorganische und Allgemeine Chemie*, **583** 67 (1990).

[6] G. Monros, J. Carda, P. Escribano and J. Alarcon, Synthesis of V-$ZrSiO_4$ solid solutions, *Journal of Materials Science Letters*, **9** 184 (1990).

[7] J. A. Taylor and A. Bull, *Ceramic Glaze Technology*, Pergamon Press, New York (1986).

[8] F. J. Berry, D. Eadon, J. Holloway and L. E. Smart, Iron-doped zirconium silicate. Part 1-The location of iron, *Journal of Materials Chemistry*, **6** 221 (1996).

[9] F. J. Berry, D. Eadon, J. Holloway and L. E. Smart, Iron-doped zircon: The mechanism of formation, *Journal of Materials Science*, **34** 3631 (1999).

[10] D. Ball and J. A. van Wyk, The Electron Paramagnetic Resonance of Fe^{3+} Observed in Two Axial Sites in Synthetic Single Crystals of Zircon ($ZrSiO_4$), *Physica Status Solidi (b)*, **218** 545 (2000).

[11] R. D. Shannon, Revised Effective Ionic Radii and Systematic Studies of Interatomic Distances in Halides and Chalcogenides, *Acta Crystallographica*, **A32** 751 (1976).

[12] E. Carreto, C. Piña, H. Arriola, C. Barahona A. N. Nava and V. Castaño, Mössbauer study of the structure of Fe-zircon system, *Journal of Radioanalytical and Nuclear Chemistry*, **250** 453 (2001).

[13] P. Tartaj, R. González-Carreño, C. J. Serna and M. Ocaña, Iron Zircon Pigments Prepared by Pyrolysis of Aerosols, *Journal of Solid State Chemistry*, **128** 102 (1997).

[14] M. Llusar, J. Calbo, J. A. Badenes, M. A. Tena and G. Monrós, Synthesis of iron zircon coral by coprecipitation routes, *Journal of Materials Science*, **36** 153 (2001).

[15] K. Fujii and K. Sono, *Reps. Govt. Res. Inst. Ceram.*, **6** 18 (1952).

[16] M. Ocaña, A. Caballero, A. R. González-Elipe, P. Tartaj, C. J. Serna and R. I. Merino, The effects of the NaF flux on the oxidation state and localisation of praseodymnium in Pr-doped zircon pigments, *Journal of the European Ceramic Society*, **19** 641 (1999).

[17] E. A. Harris, J. H. Mellor and S. Parke, Electron Paramagnetic Resonance of Tetravalent Praseodymium in Zircon, *Physica Status Solidi (b)*, **122** 757 (1984).

[18] M. Stiebler, C. Steudtner and S. Kemmler-Sack, Praseodymium Zircon Yellow, *Physica Status Solidi (a)*, **132** 495 (1992).

[19] M. Ocaña, A. Caballero, A. R. González-Elípe, P. Tartaj and C. J. Serna, Valence and Localization of Praseodymnium in Pr-Doped Zircon, *Journal of Solid State Chemistry*, **139** 412 (1998).

[20] K. Hill, R. Lehman and D. Swiler, Effects of Selected Processing Variables on Color Formation in Praseodymnium-Doped Zircon Pigments, *Journal of the American Ceramic Society*, **83** 2177 (2000).

[21] M. Mägi, E. Lippmaa, A. Samoson, G. Engelhardt and A. R. Grimmer, Solid-state high resolution silicon-29 chemical shifts in silicates, *Journal of Physical Chemistry*, **88** 1518 (1984).

[22] B. D. Beff, N. J. Hess, W. J. Weber, S. D. Conradson, M. J. Schweiger and R. C. Ewing, XAS and XRD study of annealed ^{238}Pu- and ^{239}Pu-substituted zircons ($Zr_{0.92}Pu_{0.08}SiO_4$), *Journal of Nuclear Materials*, **278** 212 (2000).

[23] S. Ríos, T. Malcherek, E. K. H. Salje and C. Domenghetti, Localized defects in radiation-damaged zircon, *Acta Crystallographica Section B*, **56** 947 (2000).

[24] I. Farnan, ^{29}Si NMR characterisation of the crystalline-amorphous transition in $ZrSiO_4$, *Phase Transitions*, **69** 47 (1999).

[25] I. Farnan and E. K. H. Salje, The degree and nature of radiation damage in zircon observed by ^{29}Si nuclear magnetic resonance, *Journal of Applied Physics*, **89** 2084 (2001).

[26] J. V. Smith and C. S. Blackwell, Nuclear magnetic resonance of silica polymorphs. *Nature*, **303** 223 (1983).

[27] J. F. Stebbins, Nuclear magnetic resonance spectroscopy of silicates and oxides in geochemistry and geophysics, *Mineral physics and crystallography. A handbook of physical constants*, AGU, Washington, 1995.

[28] V. I. Matkovich and P. M. Corbett, Formation of zircon from zirconium dioxide and silicon dioxide in the presence of vanadium pentoxide, *Journal of the American Ceramic Society*, **44** 130 (1960).

[29] P. A. Schroeder and R. J. Pruett, Fe ordering in kaolinite: Insights from ^{29}Si and ^{27}Al MAS NMR spectroscopy, *American Mineralogist*, **81** 26 (1996).

[30] P. A. Schroeder, R. J. Pruett and V. J. Hurst, Effects of secondary iron phases on kaolinite ^{27}Al MAS NMR spectra, *Clays and Clay Minerals*, **46** 429 (1998).

[31] K. J. D. MacKenzie, I. W. M. Brown, C. M. Cardile and R. H. Meinhold, The thermal reactions of muscovite studied by high-resolution solid-state 29-Si and 27-Al NMR, *Journal of Materials Science*, **22** 2645 (1987).

[32] M. Kato, S. Yamashita and M. Takahashi, Red coloring of glaze by manganese-zircon purple pigment, *Journal of the Ceramic Society of Japan*, **108** 742 (2000).

[33] V. L. La Villa and J. M. Rincón López, Study of the Mechanism of Formation of a Zircon-Cadmium Sulphoselenide Pigment, *Transactions Journal of the British Ceramic Society*, **80** 105 (1981).

[34] T. J. Bastow, ^{91}Zr nuclear quadrupole coupling in zircon ($ZrSiO_4$), *Journal of Physics: Condensed Matter*, **2** 6327 (1990).

[35] L. Rubio-Puzzo, M. C. Caracoche, M. M. Cervera, P. C. Rivas, A. M. Ferrari and F. Bondioli, Hyperfine Characterization of Pure and Doped Zircons, *Journal of Solid State Chemistry*, **150** 14 (2000).

[36] R. W. G. Wyckoff and S. B. Hendricks, Crystal Structure of Zircon, and Criteria for the Special Position in Tetragonal Spacegroups, *Zeitschrift für Kristallographie*, **66** 73 (1927).

[37] I. R. Krstanović, Redetermination of the oxygen parameters in zircon ($ZrSiO_4$), *Acta Crystallographica*, **11** 896 (1958).

[38] K. Robinson, G. V. Gibbs and P. H. Ribbe, The structure of zircon: a comparison with garnet, *American Mineralogist*, **56** 782 (1971).

[39] F. H. Larsen, H. J. Jakobsen, P. D. Ellis, N. C. Nielsen, QCPMG-MAS NMR of half-integer quadrupolar nuclei, *Journal of Magnetic Resonance*, **131** 144 (1998).

Chapter 5

Vanadium-doped zircon

5.1 Introduction

Blue coloured vanadium-doped zircon has received the most scientific attention of all the doped zircons. It is produced in large quantities commercially by mixing ZrO_2 and SiO_2 in an equimolar ratio. A pigment source such as V_2O_5 is added in excess along with mineralisers (usually including NaF) to lower the temperature required for pigment formation. A recent study by Llusar[1] on the best composition to use to optimise colour, and minimise environmentally damaging byproducts found the mixture $(ZrSiO_4)(V_2O_5)_{0.19}(NaF)_{0.05}(NaCl)_{0.10}$ provided the best results.

The first vanadium-doped pigments were created by Seabright[2], who established through X-ray diffraction techniques that the pigment was a single zircon phase with vanadium somehow incorporated within it. Sometime later, Matkovich[3] used differential thermal analysis (DTA) to investigate why the pigment was blue in colour when Na_2O was used as a mineraliser, and green when it was omitted. When blue pigment made using Na_2O was washed with water, no vanadium species were removed. When the Na_2O flux was omitted, V_2O_5 could be washed out leaving the pigment a blue colour. Since V_2O_5 is a yellow colour, the mixture of it and the blue colour of the remaining pigment caused the original green colour. This was attributed to the mineraliser reducing the temperature that zircon was formed from SiO_2 and ZrO_2. At lower temperatures, V_2O_4 is stable and V^{4+} can be incorporated into the zircon. Without the mineraliser, zircon forms at higher temperatures where a mixture of V_2O_4 and V_2O_5 exists, so V^{4+} enters the zircon lattice

to give it a blue colour, and V^{5+} stays as a yellow V_2O_5 phase. It was also found that V-$ZrSiO_4$ was not the equilibrium mixture, and if it is held at temperature the V^{4+} in the zircon will be liberated to form $ZrSiO_4$ and V_2O_5.

The green colour of V-$ZrSiO_4$ has also been investigated by Vicent[4] who varied the fluoride addition and preparation method to see how the shape and size of the vanadium particles affected the colour. No correlations were observed, however IR measurements showed that more Si-O bonds were present in greener materials compared to blue zircons.

Demiray[5] fired V-$ZrSiO_4$ under various conditions designed to encourage different vanadium oxidation states. It was found through comparison with YPO_4 absorption spectra which contain V^{3+}, that this oxidation state could not be incorporated into V-$ZrSiO_4$, and through crystal field calculations it was concluded that vanadium was only present as V^{4+} within the zircon, and was only at the ZrO_8 site.

Electron spin resonance (ESR) measurements by Gregorio[6] found eight equally spaced lines which were attributed to the hyperfine interaction of the d^1 electrons of the V^{4+} with the nuclear spin of $I = \frac{7}{2}$ at the ^{51}V nucleus. It was also possible to calculate hyperfine field values, although from ESR measurements the results could not directly be interpreted in terms of doping for different $ZrSiO_4$ sites. In contrast to Demiray's optical absorption measurements, Gregorio was unable to conclude whether the SiO_4 or ZrO_8 sites were occupied since both have D_2d symmetry. However, this did suggest that SiO_4 was more likely to be occupied, as the cubic crystal field splittings were similar to those previously measured for other $3d^1$ ions in XO_4 coordinations. They also performed point charge calculations which predicted d electron energy level splittings for the SiO_4 that were more similar to those seen experimentally, and less similar to the predictions for V^{4+} located at a ZrO_8 site.

Xiaoyu[7] later analysed Gregorio's ESR spectra and found it could be explained using conventional crystal field theory. It was concluded that the spectra could be explained by the doping of V^{4+} at both SiO_4 and ZrO_8 sites.

Raman spectroscopic measurements on V-$ZrSiO_4$ have been attempted twice. Initially, Lyons[8] found that the V-$ZrSiO_4$ spectra showed a Raman line of B_{2g} symmetry associated with a spontaneous distortion about the ligand cage surrounding the V^{4+} ion, which looked more likely to be V^{4+} at a SiO_4 site. This was later confirmed by de Waal[9],

who found their measurements were similar to other experiments performed on vanadium compounds where V^{4+} was tetrahedrally coordinated. With V^{4+} at a SiO_4 site, it was possible to perform V-O bond length calculations of 1.75Å, consistent with simulated values.

Chandley[10] used lattice-energy calculations and single crystal XRD to investigate the location of V^{4+} within zircon. When trying to simulate V^{4+} located at an interstitial site within zircon, it was found that after the ion is placed at that site and the structure allowed to equilibrate, the ion would end up displacing a Si^{4+} or Zr^{4+} and would be returned to the lattice. The conclusion was that partial substitution of V^{4+} at both SiO_4 and ZrO_8 sites was most likely as had been seen in the ESR and optical measurements performed prior to this paper.

Another theoretical simulation approach was taken by Beltrán[11], who used a cluster-in-the-lattice scheme which involved finding quantum mechanical solutions to various sizes of clusters of zircon. The effect of doping V^{4+} at the two sites within zircon was investigated, and in contrast to Chandley's calculations, only the ZrO_8 position was found to be energetically favourable.

Monros[12] was the first to apply the sol-gel technique to synthesise V-$ZrSiO_4$. This required much longer firings and higher temperatures than the ceramic preparation route (at least 1300°C for 8h). This allowed higher purity samples to be obtained with a greater control over the level of vanadium doping. The sol-gel technique was further refined by Tartaj[13], Vicent[4] and Valentin[14].

Tetragonal ZrO_2 solid solutions containing V^{4+} have also been investigated using XRD[15] and ESR and optical methods[16]. It was found that ~ 5 mol% vanadium can be accommodated within the ZrO_2, and the V^{4+} is located at ZrO_8 sites.

The two most recent studies dedicated to elucidating the location of V^{4+} within zircon were undertaken by Ocaña[17] and Puzzo[18]. Ocaña used a variety of spectroscopic techniques to examine the siting of vanadium, and suggested that it substitutes for both silicon in the tetrahedral site (N_T is the number of tetrahedral sites occupied), and to a lesser extent zirconium in the dodecahedral site (N_D). EXAFS measurements of the vanadium K-edge gave the ratio of the occupancy of the two sites as $N_T/N_D = 1.6$. This ratio could also be used to rationalise their IR measurements. Ocaña also noted that V^{4+}

was not distributed homogeneously within the sample, but had a tendency to be in layers towards the outer surface of the zircon particles. This raises the point that examining practically interesting materials to model the substitution distribution can have additional chemical complexity.

Puzzo[18] undertook a perturbed angular correlations (PAC) study which revealed the dodecahedral zirconium in a vanadium-doped zircon existed in three different environments:

1. Where no vanadium was near enough to influence the electric field gradient (EFG) experienced,

2. where vanadium had substituted for next nearest neighbour zirconium, and

3. where zirconium was thought to be near either vanadium substituting for a tetrahedral silicon, or possibly that V^{4+} was occupying a strongly distorted tetrahedral interstitial site.

Taking the two perturbed signals and assuming that the latter was a tetrahedral silicon site gives the ratio of the substitution for tetrahedral and dodecahedral sites as $N_T/N_D = 0.1$.

5.2 Visual Appearance

Figure 5.1 shows the appearance of the VV variable dopant source pigments after firing. Clearly the amount of V_2O_5 added is crucial to the colour of the pigment formed. This is in contrast to the Pr-doped zircons which exhibited the same colour for a large variation in pigment source addition. The Pr-doped zircons were fired at a higher temperature (1060°C) than the VV series of samples here, so the fluxing effect of the V_2O_5 may only be efficient when it is present in the optimum amount.

5.3 ^{29}Si MAS NMR

^{29}Si NMR measurements were performed under the same conditions as the doped zircon measurements previously. The spectra were acquired on a Bruker MSL-300 spectrometer

Figure 5.1: The five VV samples after firing. The crucible to the left has 25% the optimum amount of pigment, increasing in steps of 25% to the right where 125% pigment source has been added.

using a Bruker 7 mm double bearing MAS probe. The samples were spun to at least 3.5 kHz, and a $\pi/6$ tip angle was used along with a recycle delay of 60 s to ensure the ^{29}Si signal was not saturated. The absolute NMR signal acquired for the samples was quantified in the same manner as outlined in section 3.4.2.

5.3.1 Different V_2O_5 composition

Five doped zircons were prepared with different quantities of V_2O_5 source in the initial mixture, which were labelled VV1 through VV5. VV1 had 25% the known optimum amount of V_2O_5, VV2 had 50% through to VV5 which had 125% of the amount known to give the best pigment colour (which is $\sim$ 3 mol%). The ^{29}Si signal quantification shown in figure 5.2 shows that VV4 gives the most ^{29}Si signal of about 70% the expected ^{29}Si signal. All the other four samples give below 50%, so have to be interpreted with caution since the remainder of the signal could be paramagnetically broadened.

X-ray diffraction phase analysis of the five samples indicates that zircon has been formed in VV4, with VV3 and VV5 indicating a little zircon formation, but mainly consisting of unreacted SiO_2 and ZrO_2. VV1 and VV2 show only SiO_2 and ZrO_2. This further confirms the fluxing effect of the V_2O_5 since zircon has not formed at 860°C unless the optimum amount of V_2O_5 was added. T_1 measurements were not performed on all samples due to the length of time each acquisition of took. It is likely though, that signal saturation effects are also partly responsible for the signal loss seen in samples VV2, VV3 and VV5 where there has been little or no zircon formation. This is despite using a relatively long recycle delay of 60 s and $\pi/6$ tip angle.

Figure 5.3 shows the ^{29}Si spectra of the five samples after washing. Q^0 zircon

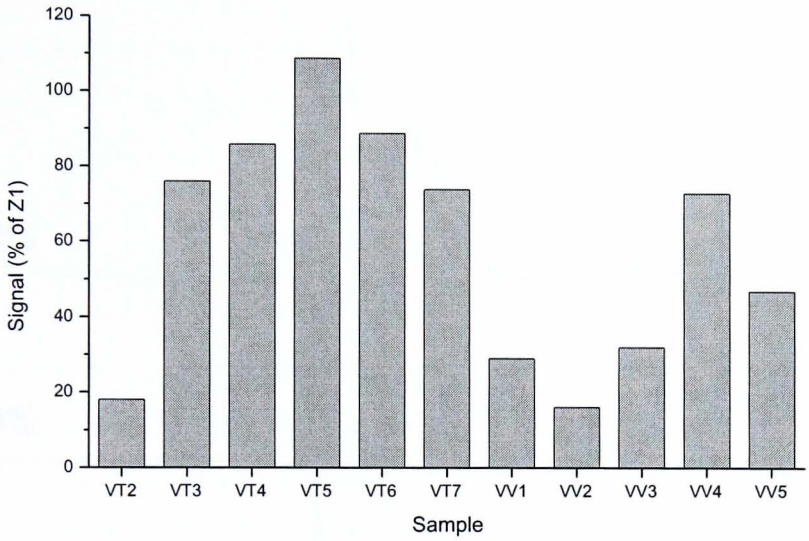

Figure 5.2: The integrated signal measured from ^{29}Si MAS NMR, scaled to reflect signal per silicon nucleus and normalised with respect to a zircon standard. The margin for error in signal measurements is estimated at $\pm 10\%$.

peaks can only be seen when a minimum of between 50 and 75% of the optimum amount of vanadium source is added, which is in agreement with the X-ray data. The 25 and 50% samples show a broad peak centred around -100 ppm which can be attributed to glassy silica which has reacted to form another phase, and has not reverted back into the original SiO_2 form on cooling. In the 50% lineshape there is a small sharp peak convoluted in with the peak at -107 ppm which could be SiO_2 which has recrystallised into quartz[19]. The 125% sample shows some zircon formation and the glassy silica peak, so an excess of vanadium source inhibits zircon creation as well as not having enough V_2O_5 source. The 75% sample shows a hint of the glassy peak, however the 100% vanadium source sample shows only zircon along with two other peaks at -74 and -105 ppm. The sol-gel synthesised sample also shows no unreacted SiO_2 species, consistent with X-ray measurements which show complete zircon formation. This spectrum also shows two extra peaks at -74 and -105 ppm, however they are much smaller than are seen in the 100% ceramic sample.

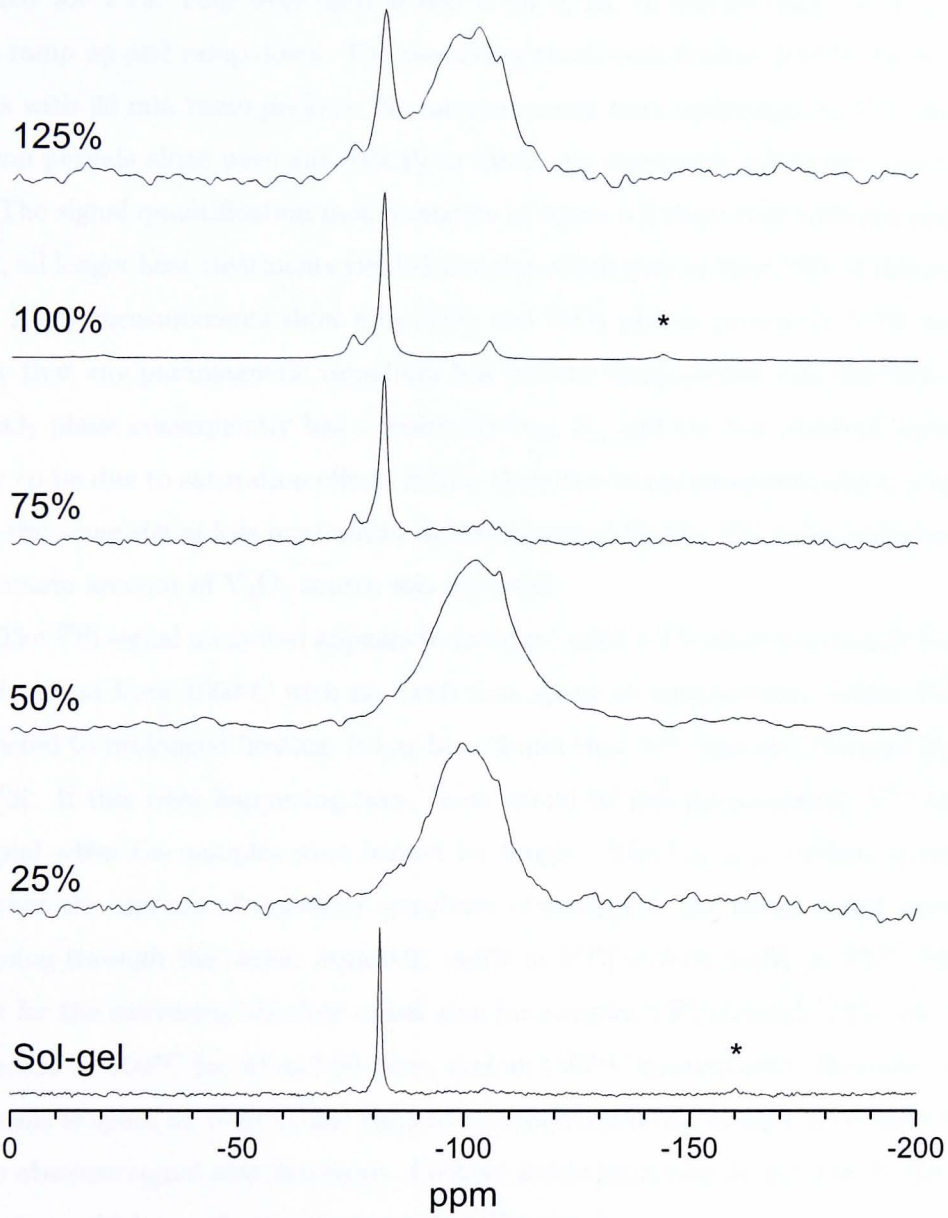

Figure 5.3: ^{29}Si spectra of five vanadium-doped zircons with varying amounts of V^{4+} source addition, and the sol-gel synthesised V-$ZrSiO_4$ pigment. The indicated amount is the relative proportion of V_2O_5 used in the ceramic samples, 100% being the amount used commercially ($\sim$ 3 mol%).

5.3.2 Different firing times

Seven samples were prepared using the optimum vanadium-content composition used previously for VV4. Four were fired at 860°C for 0, 10, 20 and 60 mins (VT1-4) with a 20 min ramp up and ramp down. The remaining three were fired at 1060°C for 0, 10 and 20 mins with 20 min ramp periods. No measurements were performed on VT1 since the two ramp periods alone were not enough to cause any observable solid state reaction.

The signal quantification measurements in figure 5.2 show that with the exception of VT2, all longer heat treatments yielded samples which gave at least 70% of the expected signal. X-ray measurements show only SiO_2 and ZrO_2 phases present in VT2, and it is unlikely that any paramagnetic vanadium has become incorporated into the SiO_2 phase. This SiO_2 phase consequently has a relatively long T_1, and the low absolute signal seen is likely to be due to saturation effects rather than due to paramagnetic signal screening. This is the same signal loss mechanism as was observed for the VV series samples where the optimum amount of V_2O_5 source was not used.

The ^{29}Si signal measured appears to increase, until VT5 where the sample has been ramped to and from 1060°C with no dwell time spent at temperature. When V-$ZrSiO_4$ is subjected to prolonged heating, it has been found that V^{4+} ions are liberated from the sample[3]. If this were happening here, there would be less paramagnetic V^{4+} to mask ^{29}Si signal when the samples were heated for longer. The $V_{chemical}$ column in table 5.1 shows that the amount of insoluble vanadium remaining in the sample after washing is lower going through the series, from 0.91 mol% in VT3 to 0.69 mol% in VT7. This can account for the increasing absolute signal seen for samples VT3 through VT5, which have been heated at 860°C for 20 and 60 mins, and at 1060°C momentarily. However, when a longer time is spent at 1060°C, the amount of vanadium in the sample is reduced further and the absolute signal also decreases. Another mechanism may be present at the higher temperature which is reducing the measured ^{29}Si signal.

Figure 5.4 shows the ^{29}Si spectra of the fired samples after washing. Spectra similar to VV4 are seen for all samples except VT2 which has only spent 10 mins at 860°C. Clearly VT2 has not yet had sufficient time at temperature to form V-$ZrSiO_4$. There is no broad glassy SiO_2 peak as was observed in figure 5.3, so if the SiO_2 has had the opportunity to react to form another phase, it has recrystallised upon cooling to leave the cristobalite

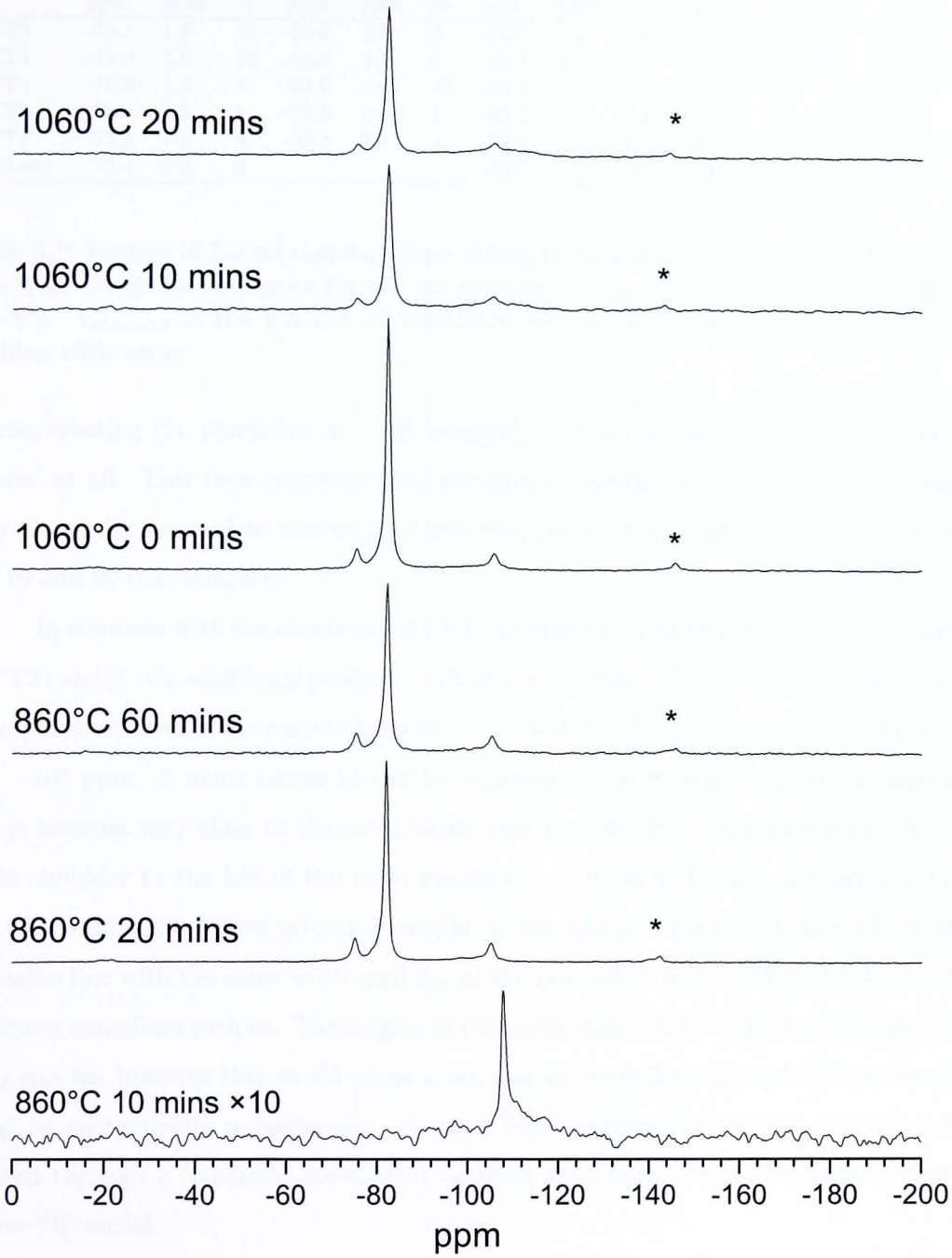

Figure 5.4: ^{29}Si spectra of the VT series of samples, VT2 is at the bottom running through to VT7 at the top. The optimum amount of V_2O_5 has been added, however the firing times and temperatures have been varied.

Sample	Line 1			Line 2			Line 3			Line 4			
	δ_{iso} ppm	Δ ppm	I %	δ_{iso} ppm	Δ ppm	I %	δ_{iso} ppm	Δ ppm	I %	δ_{iso} ppm	Δ ppm	I %	$V_{chemical}$ mol%
VT3	-75.1	1.7	10	-80.0	3.0	5	-82.0	1.2	65	-105.1	1.9	9	0.91
VT4	-75.2	1.6	10	-80.3	3.3	5	-82.1	1.2	63	-105.4	1.8	8	0.92
VT5	-75.3	1.8	8	-81.0	1.6	15	-82.2	1.1	55	-105.4	1.9	7	0.87
VT6	-75.4	1.5	5	-79.5	2.0	1	-82.2	1.1	62	-105.2	1.8	4	0.69
VT7	-75.3	1.5	5	-79.4	3.0	4	-82.2	1.1	62	-105.5	1.4	3	0.69
Sol-gel	-75.4	2.0	6				-82.2	1.1	80	-106.0	2.0	5	

Table 5.1: Results of Lorentzian lineshape fitting to vanadium-doped zircon ^{29}Si spectra. The error estimates and units for the parameters are $\delta_{iso} \pm 0.4$ ppm, $\Delta \pm 0.3$ ppm and $I \pm 4\%$. $V_{chemical}$ is the amount of vanadium remaining in the sample in mol% after washing with water.

species creating the resonance at -108 ppm[20]. It is more likely that the SiO_2 has not reacted at all. This then indicates that the zircon forming reaction takes < 10 mins to take place, since complete conversion from SiO_2 into zircon happens sometime between the 10 and 20 min samples.

In common with the spectrum of VV4, the spectra of all samples with the exception of VT2 exhibit two additional peaks at -75 and -105 ppm. Table 5.1 shows the results of fitting these spectra to Lorentzian lines at -81.6 ppm for the zircon resonance, and at -75 and -105 ppm. A much better fit can be achieved for all spectra if an extra Lorentzian line is inserted very close to the main zircon line at -80 ppm. This manifests itself as a slight shoulder to the left of the main resonance. This shoulder was not present in the ^{29}Si spectrum of the sol-gel prepared sample. It was usually necessary to also add a subtle Gaussian line with the same width and δ_{iso} as the glassy line seen in figure 5.3 for the non-optimum vanadium recipes. The origins of the Lorentzian lines could be attributed to Q^n SiO_2 species, however this would mean a mixture of crystalline Q^0 and Q^3 coordinations which is energetically unfavourable. A more likely explanation is that they have been created through a hyperfine interaction between vanadium within the sample, and the probe ^{29}Si nuclei.

5.3.3 Saturation recovery measurements

The presence of V^{4+} in the zircon lattice, and any paramagnetic contribution it may make to the spectrum prompted saturation recovery measurements to be performed, to calculate

Peak position (ppm ±0.4)	-81.6	-73.9	-80.0	-105.2
T_1 (s ±0.3)	1.8	1.0	(0.1)	0.8

Table 5.2: T_1 times calculated for the four ^{29}Si resonances in sample VT4 (washed).

the T_1 times of all four peaks observed. The magnet and probe setup used to acquire the VV and VT ^{29}Si spectra was employed, however a saturation recovery pulse sequence was used instead of a single pulse experiment. The sample investigated was VT4, and a train of 30 $\pi/2$ pulses, 20 ms apart were used to saturate the sample's magnetisation. Spectra were acquired with τ delay periods ranging from 5 ms to 10 s. Lorentzian lineshapes were then fitted to the spectra, and from a plot of line intensity vs τ, T_1 values for each site were calculated and are listed in table 5.2. Due to the low signal to noise measured in some of the shorter τ measurements, fitting of the -80 ppm resonance to the shoulder of the main zircon resonance could only give a rough estimate of the T_1 time for this resonance.

The T_1 time of the main zircon line is typically a factor of 2 greater than the other two well resolved lines. T_1 measurements performed on undoped zircons[21] indicate T_1 times of the order of 1000 s, three orders of magnitude longer than the 1.8 s T_1 time of zircon measured here. This means the paramagnetic V^{4+} present in the sample is clearly providing an efficient T_1 relaxation mechanism.

Figure 5.5 shows three spectra acquired with $\tau = 0.5, 0.8$ and 60 s. The bottom two spectra clearly show the presence of a line close to the zircon resonance with a much shorter T_1 relaxation time, so the fitting of a line at -80 ppm is justified.

5.3.4 Variable temperature NMR measurements

Variable temperature measurements were also performed on sample VT4. A strong temperature dependence of the position of the three extra lines would further indicate a paramagnetic shifting effect due to V^{4+} substitution within the sample. The spectra were acquired under similar MAS conditions to previous ^{29}Si spectra, however since the T_1 times were more accurately known for the sites, a recycle delay of 10 s was used along with a $\pi/2$ tip angle. Although this lead to an increased possibility of signal saturation,

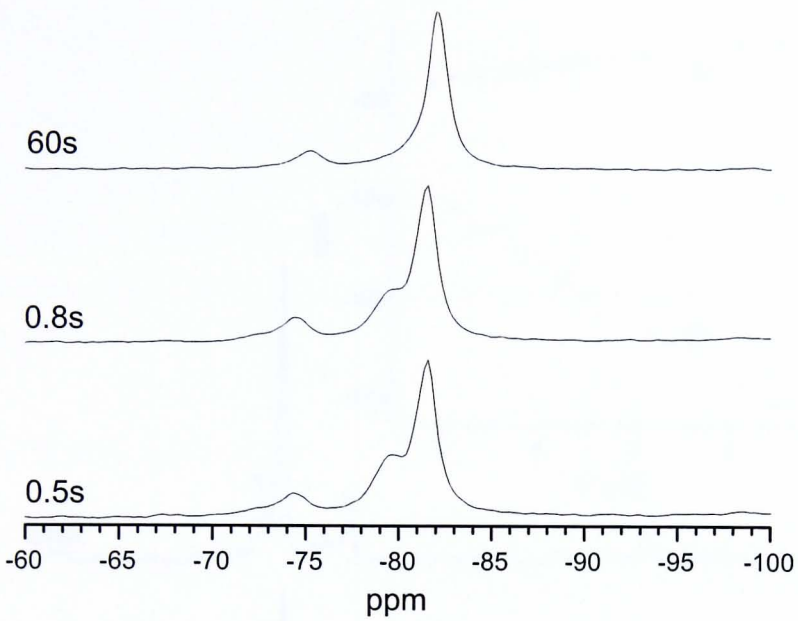

Figure 5.5: ^{29}Si saturation recovery measurements on VT4 using three different recovery delays.

it would not affect the position of the resonances which was the main property under investigation. Quicker data acquisition times were also necessary, since holding the probe temperature constant for long periods of time whilst the sample was spinning was technically challenging at lower temperatures. Measurements were acquired in the range 153 to 343 K, and spectra at three temperatures are shown in figure 5.6. Once again, due to the difficulty in acquiring sufficiently high signal-to-noise at different temperatures, fitting of the spectra to measure the -80 ppm resonance shift was not performed. The shifts of the remaining two contact shifted peaks, labelled A and B were measured and their linear T^{-1} dependence has also been plotted in figure 5.6.

The indication from the short T_1 times and temperature dependence of the extra peaks present, is that they have been created through a hyperfine interaction. To help elucidate this mechanism, bulk DC magnetic susceptibility measurements for VT4 were acquired at different temperatures at a field of 5000 Oe using a Quantum Design MPMS5 SQUID magnetometer. The results of the molar susceptibility χ measured for the sample at temperatures from 2 to 340 K have been plotted against T^{-1} in figure 5.7. The variation

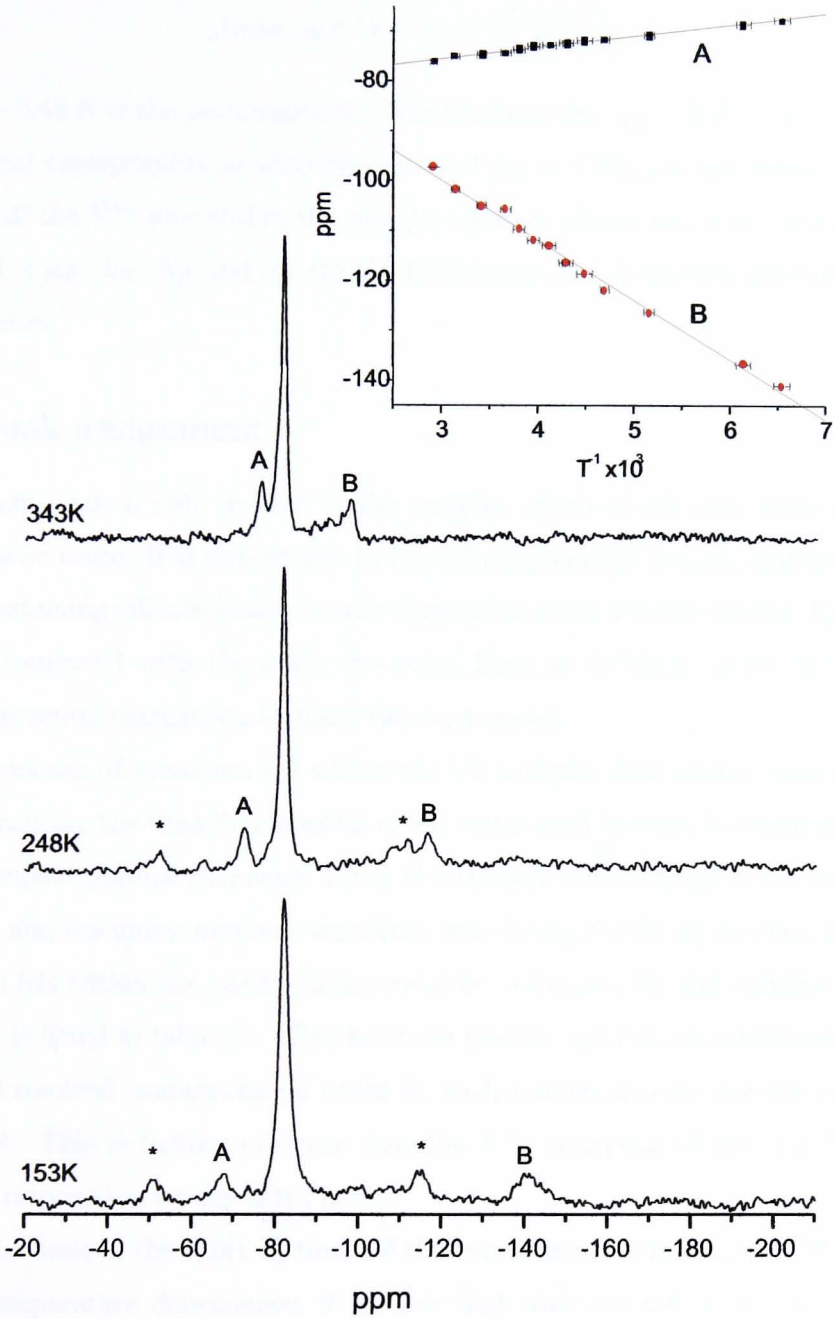

Figure 5.6: ^{29}Si MAS measurements of VT4 at three different temperatures where the two resolvable contact shifted lines have been labelled. The position of the resonances varying with T^{-1} has also been plotted (inset).

of χ with temperature follows a Curie-Weiss law, and can be fit using

$$\chi(\text{emu mol}^{-1}) = \chi_0 + \frac{p_{\text{eff}}^2 \mu_B^2 N_A}{3k_B(T-\theta)} \tag{5.1}$$

where $\theta = -0.43$ K is the paramagnetic Curie temperature, $\chi_0 = 9.96 \times 10^{-3}$ emu mol^{-1} is the residual susceptibility at absolute zero and $p_{\text{eff}} = 1.79\mu_B$ is the effective magnetic moment of all the V^{4+} ions within the sample, which is almost twice the free space value for V^{4+} of $1 \times \mu_B$. k_B, N_A and μ_B are the Boltzmann and Avogadro constants, and the Bohr magneton.

5.3.5 Peak assignment

The -80 ppm peak is only present in the samples which which have been synthesised using a ceramic route. It is not present in the sol-gel prepared sample, and so is likely to be a V^{4+}-containing silicate phase. It also appears to have a much shorter T_1 relaxation time when compared with the other two extra lines, so is likely to be experiencing a stronger interaction mechanism to these two resonances.

The amount of vanadium left within the VT samples after washing has been calculated by measuring the vanadium content of the water used to wash the samples using the inductive coupled plasma technique. Since the amount of vanadium in the initial recipe was known, and assuming minimal vanadium loss during the firing process, the amount of vanadium left within the zircon lattice could be calculated for the variable firing time zircons, and is listed in table 5.1. This has been plotted against the combined integral of the two well resolved contact shifted peaks for each sample, and the correlation is shown in figure 5.8. This is further evidence that the V^{4+} incorporated into the blue zircon pigments is responsible for the extra peaks.

On the basis of the short T_1 times of the two additional lines in the ^{29}Si spectrum, and their temperature dependence, it is clear that they are influenced by a hyperfine interaction. The correlation between the amount of vanadium within the zircon, and the combined integral of the extra lines suggests that the hyperfine interaction is caused by V^{4+} in the pigment. Since V^{4+} is only likely to be present at the SiO_4 and ZrO_8 cation sites, this strongly suggests that the extra lines are the main zircon resonance which has been shifted by the presence of V^{4+} nearby.

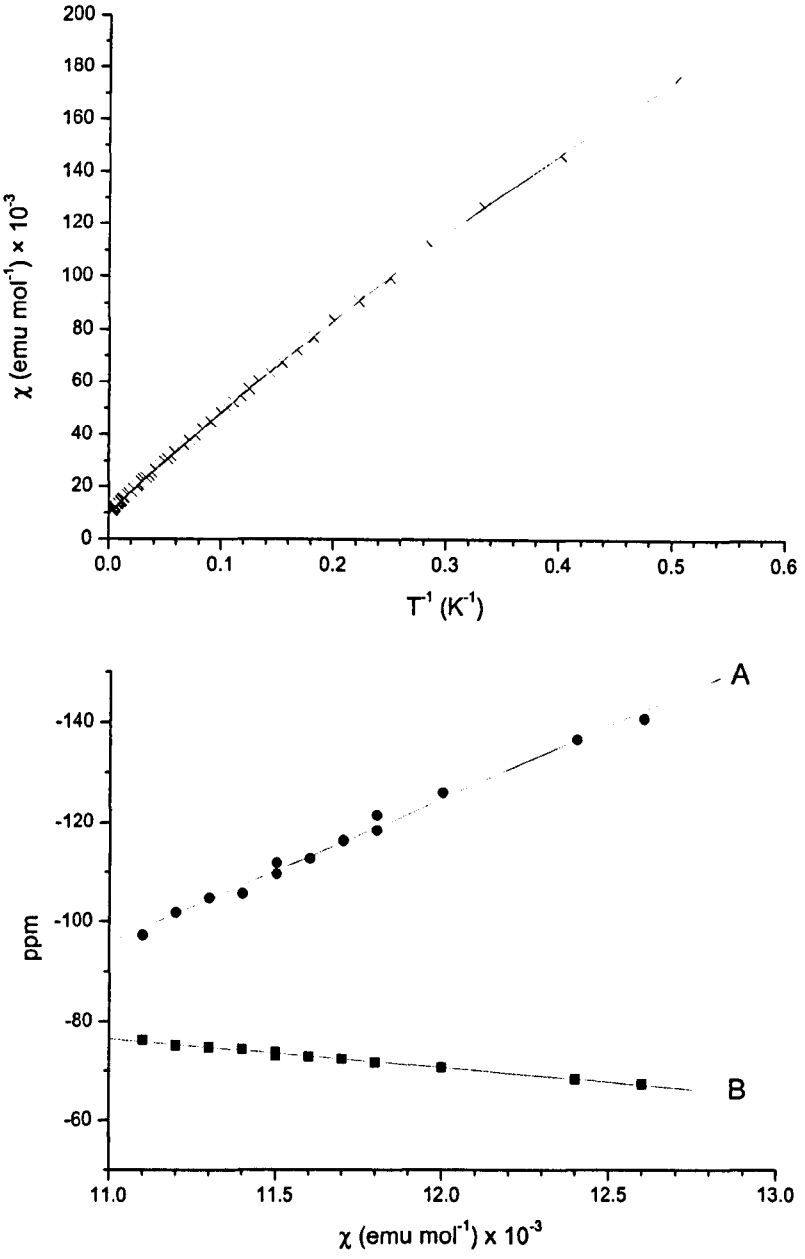

Figure 5.7: Magnetic susceptibility measured varying with T^{-1} fitted using equation 5.1 (top), and the shift of the two contact shifted resonances plotted against the susceptibility at the temperature of the experiment (bottom).

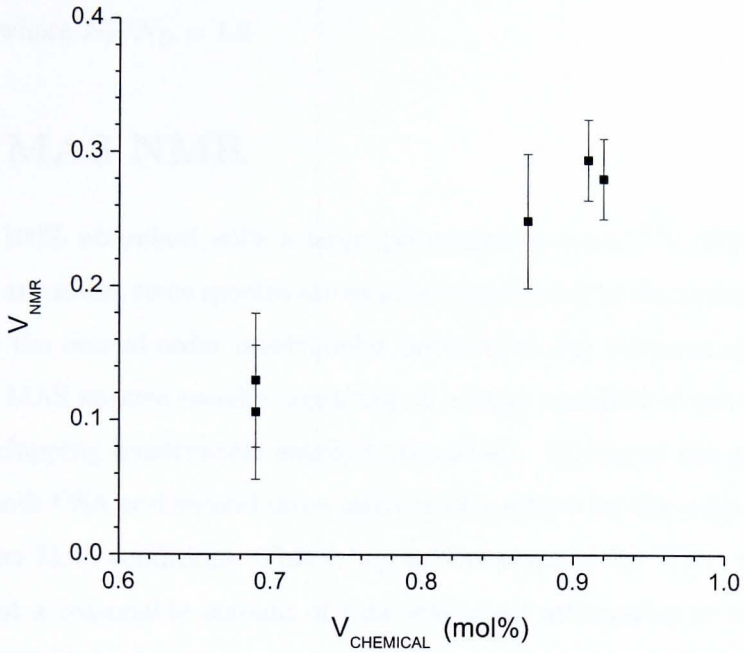

Figure 5.8: Variation of the combined integral of the two well resolved peaks with the amount of vanadium left encapsulated within the zircon sample deduced from chemical analysis.

The χ-ppm relationships of the two well resolved sites in figure 5.7 shows that the slopes of the two different sites have different signs. This probably indicates that the shifts are caused by a transferred hyperfine interaction mediated by the intermediate electrons. The substitution of V^{4+} at different cation sites will then be via one intermediate oxygen when at the ZrO_8 site (V-O-Si), or via two intermediate oxygens when at the SiO_4 site (V-O-Zr-O-Si). This can easily change the sign of the transferred hyperfine field. Although this field will not have the same distance dependence as a through space field, the effect of the transferred field will decay with distance. Since V^{4+} substituting at a ZrO_8 site is only one coordination sphere (3.00 or 3.63Å) from the probe nucleus, it will shift the signal the most and could be responsible for the -104.8 ppm resonance. V^{4+} substituting at a further away SiO_4 site (5.58 or 6.61Å) will not induce as large a shift and could be responsible for the -75.2 ppm peak. The ratio of the hyperfine fields calculated from the gradient of the shift vs χ is ~ 5, which is in the range expected for r^3. This means that the ratio of tetrahedral to dodecahedral sites occupied in this series of samples can be

calculated to be $N_T/N_D = 1.2 \pm 0.2$. This supports the recent EXAFS findings performed by Ocaña[17], where $N_T/N_D = 1.6$.

5.4 ^{51}V MAS NMR

Despite being 100% abundant with a large gyromagnetic ratio, ^{51}V NMR has received relatively little attention, since spectra are usually complicated by the presence to a similar degree of both the second-order quadrupolar interaction and chemical shift anisotropy. This results in MAS spectra usually consisting of a large manifold of spinning sidebands containing overlapping quadrupolar satellite transitions. Fitting of the spectra requires simulation of both CSA and second-order quadrupolar effects for the central and satellite transitions under MAS conditions. This is beyond the scope of the Winfit fitting software used, and whilst a reasonable amount of time was spent attempting to use the recently released SIMPSON[22] software to simulate the interactions, only limited fitting could be achieved.

^{51}V NMR has mainly been used over the last ten years to look at vanadium containing catalysts where the CSA interaction usually dominates[23, 24]. There have also been some reports where custom written software has been used to simulate the spinning sideband manifolds in crystalline vanadium compounds[25].

5.4.1 Variable vanadium content

^{51}V NMR was performed on the VV set of variable vanadium content zircons at a field of 8.45 T, using a Bruker 4 mm double bearing probe with the sample spinning at 10 kHz. A quadrupolar echo sequence was used consisting of two 0.75 μs pulses placed a rotor period apart.

Figure 5.9 shows the effect of the different V_2O_5 content on the ^{51}V MAS NMR spectra. The spectra are of the samples before they were washed. When the fired samples had been washed, the only vanadium remaining within the sample should be V^{4+} at SiO_4 and ZrO_8 sites in the zircon, and as the extra V^{4+}-containing silicate phase. A number of washed V-$ZrSiO_4$ samples were examined, however no ^{51}V signal was observed in any samples, since the paramagnetic moment of the V^{4+} is likely to be broadening any signal

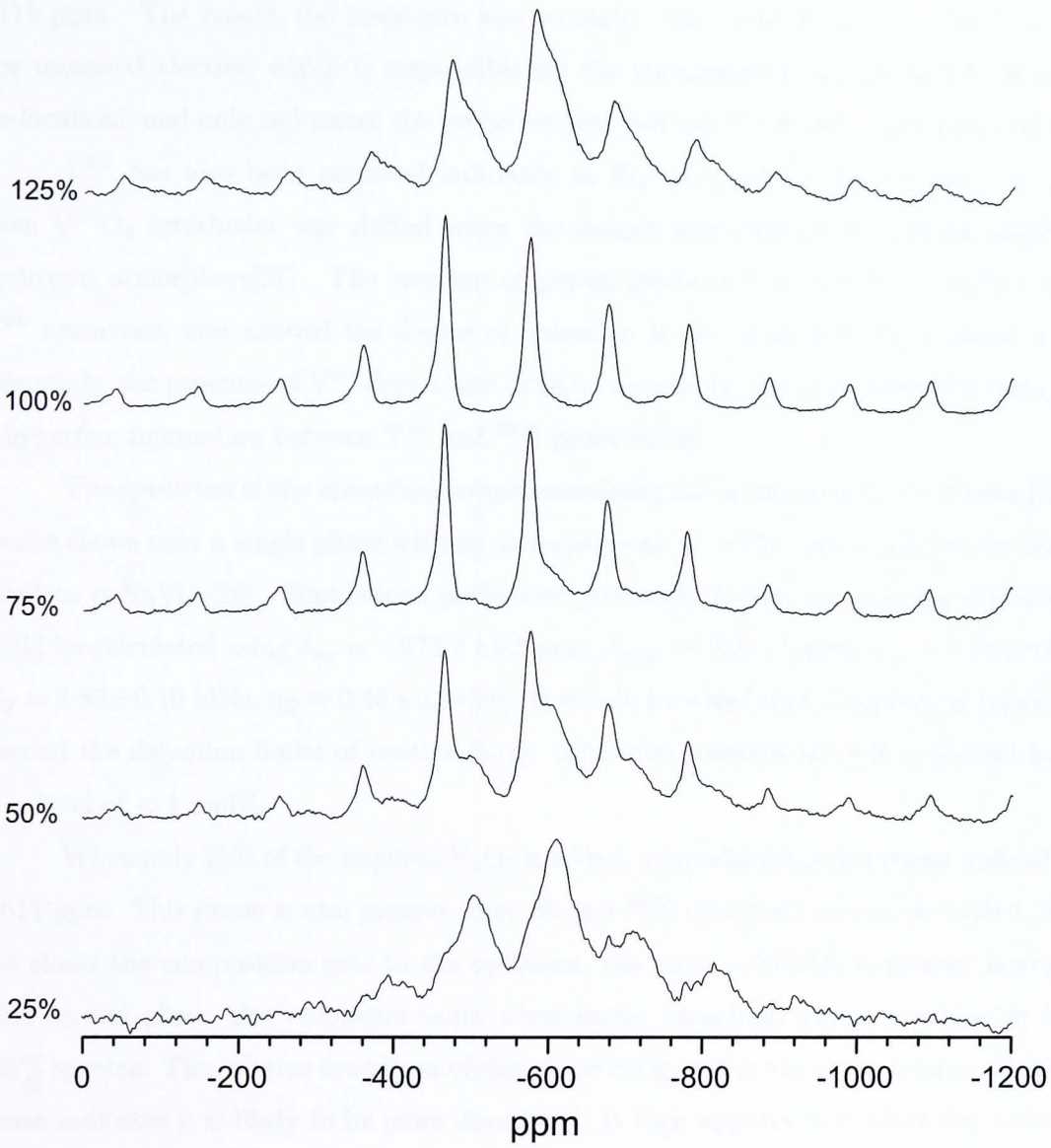

Figure 5.9: ^{51}V MAS NMR spectra at 8.45 T of the variable vanadium content V-$ZrSiO_4$.

beyond detection. V^{4+} has proved an elusive species to observe using ^{51}V NMR, however it has recently been directly observed in β-VO_2[26]. The vanadium in β-VO_2 is thought to exist as either V^{4+}, or as a mixture of V^{3+} and V^{5+} states. Since the group only observed one resonance, this was assigned to a single V^{4+} site and contained a Knight shift of 2115 ppm. The reason the resonance was so easily observable is likely to be because the unpaired electron which is responsible for the paramagnetic nature of V^{4+} is now de-localised, and only influences the probe nucleus through the Knight shift interaction.

V^{4+} has also been observed indirectly in $Bi_4V_2O_{11}$ where the resonance signal from $V^{5+}O_4$ tetrahedra was shifted when the sample was reduced by heating under a hydrogen atmosphere[27]. The creation of paramagnetic $V^{4+}O_6$ octahedra shifted the V^{5+} resonance, and allowed the degree of reduction to be quantified. In common with this study, the presence of V^{4+} doped into $ZrSiO_4$ can only be observed indirectly through a hyperfine interaction between V^{4+} and ^{29}Si probe nuclei.

The spectrum of the unwashed sample containing the optimum amount of vanadium source shows only a single phase with an isotropic peak at -570 ppm which can be identified as α-$NaVO_3$[28]. Simulations performed previously found the spinning sidebands could be calculated using $\delta_{iso} = -572.7 \pm 0.5$ ppm, $\delta_{aniso} = 259 \pm 5$ ppm, $\eta_{cs} = 0.76 \pm 0.03$, $C_Q = 3.80 \pm 0.10$ MHz, $\eta_Q = 0.46 \pm 0.04$[28]. It should be noted that this phase is typically beyond the detection limits of routine X-ray diffraction methods since it is present here at a level of < 1 mol%.

When only 25% of the required V_2O_5 is added, a broader phase is present instead at -611 ppm. This phase is also present when 50 and 75% vanadium source are added, but the closer the composition gets to the optimum, the more α-$NaVO_3$ is present instead. This second phase also reappears again when excess vanadium source is added in the 125% spectra. The relative broadness of this phase compared to the crystalline $\alpha-NaVO_3$ phase indicates it is likely to be more disordered. It then appears that when the amount of vanadium added is not close to the optimum amount, zircon cannot form and V^{4+} does not enter the zircon lattice, instead creating another more disordered vanadium phase. ^{51}V MAS NMR was performed on V_2O_5, and the apparent isotropic shift and manifold of spinning sidebands were different to the unidentified phase seen here.

5.4.2 Variable firing conditions

^{51}V NMR was performed on the VT set of variable firing time zircons at a field of 8.45 T, using a Doty 4 mm DB DD probe with the sample spinning at 16 kHz. Although the same amplifier power output settings were used as for the VV series of samples, a quadrupolar echo sequence consisting of two shorter 0.65 μs pulses (a rotor period apart) achieved the same effective magnetisation tip angle.

Figure 5.10 shows the effect of the different firing times on the ^{51}V spectra of the unwashed samples. All the spectra are identical, showing a single α-$NaVO_3$ phase at -570 ppm, so there appears to be no firing time dependence of the α-$NaVO_3$ phase formed. However, these spectra appear different to the spectrum of the optimum V_2O_5 content sample VV4 in figure 5.9. This is because the spinning speed is faster for this series of samples, so the different partitioning of the signal into sidebands at the two speeds causes the different appearance of the spectra. At the slower spinning speed, the isotropic peak at -570 ppm is not actually the peak with the highest intensity, however this is the case once the spinning speed is increased sufficiently. The firing time dependence of these spectra is different to the ^{29}Si spectra of these samples in figure 5.6. The ^{29}Si spectra of VT2 which only spent 10 mins at 860°C was very different from the remaining spectra where complete conversion from SiO_2 and ZrO_2 to zircon had taken place. This indicates that the conversion of V_2O_5 and NaF/NaCl to α-$NaVO_3$ occurs before SiO_2 and ZrO_2 form $ZrSiO_4$.

As with the variable V_2O_5 composition samples, no ^{51}V signal could be measured after sample washing as the only observable V^{5+} phase has been removed from the sample by the washing.

5.5 ^{23}Na MAS NMR

Solid state ^{23}Na MAS NMR was used to investigate the roles of the NaCl and NaF mineralisers in the reaction. MAS NMR measurements were performed at 14.1 T using a Varian 3.2 mm T3 MAS probe. ^{23}Na is 100% abundant, has a large gyromagnetic ratio and since $I = \frac{3}{2}$, less signal is taken up by the satellite transitions compared to the ^{51}V measurements where $I = \frac{7}{2}$. Because of the high resonant frequency of 158.7 MHz, and

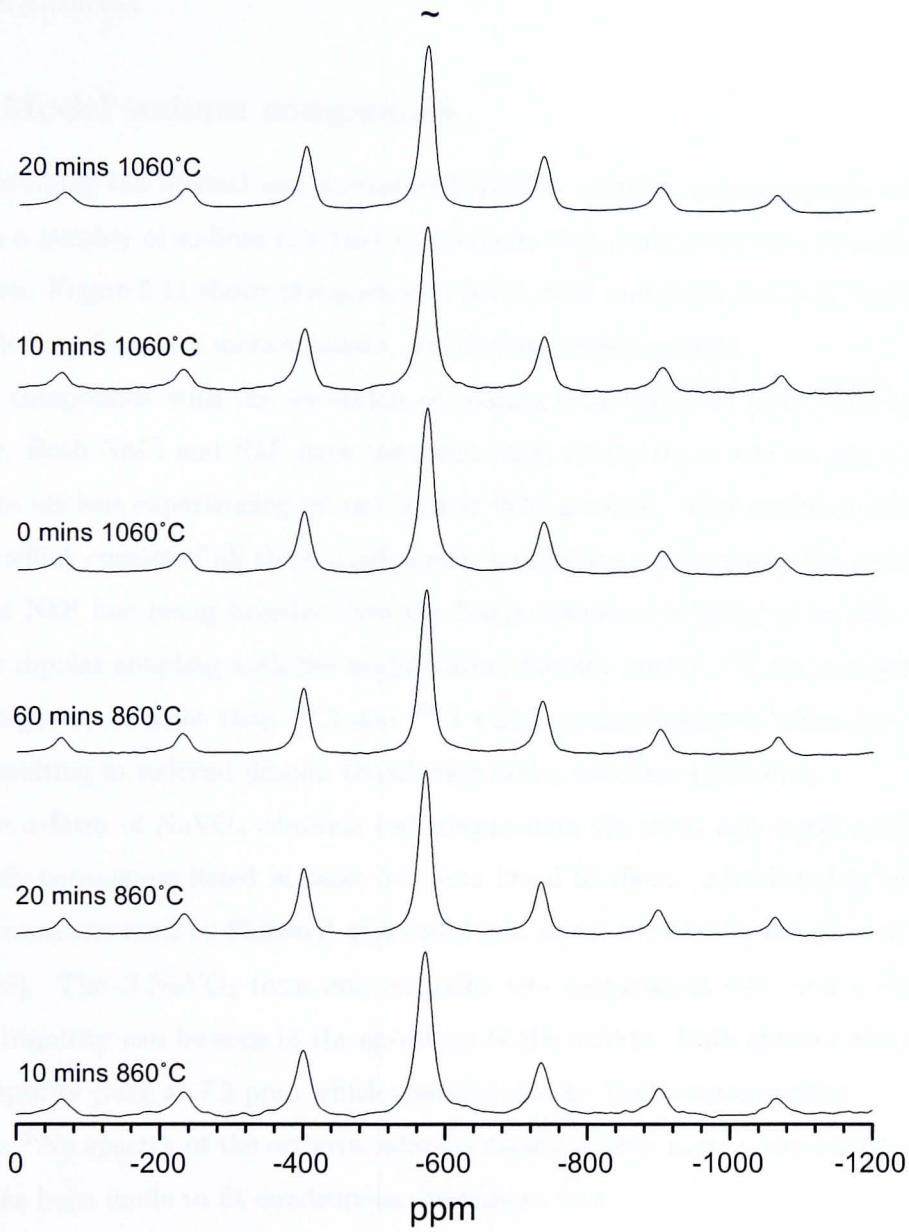

Figure 5.10: ^{51}V MAS NMR spectra at 8.45 T of V-$ZrSiO_4$ fired at different temperatures for different durations. $\sim$ signifies the isotropic peak.

since the typical ^{23}Na shift range is quite narrow, a single pulse approach was sufficient to acquire undistorted spectra. A pulse length of 0.95 μs was used (half the length of a solution 90° pulse) and a very small deadtime of 6 μs meant only one datapoint needed to be back predicted.

5.5.1 Model sodium compounds

Before examining the washed and unwashed V-$ZrSiO_4$ samples, measurements were performed on a number of sodium reference compounds that could have been formed during the reaction. Figure 5.11 shows the spectra of NaCl, NaF and three forms of $NaVO_3$: the α- and β-forms of sodium metavanadate, and sodium orthovanadate.

All compounds with the exception of sodium orthovanadate have been reported previously. Both NaCl and NaF have the same cubic symmetry at the Na site resulting in the ^{23}Na nucleus experiencing no net electric field gradient. This results in the sharp lines seen which consist of all three quadrupolar transitions overlapping. The mechanism behind the NaF line being broader than the NaCl resonance is likely to be due to heteronuclear dipolar coupling with the neighbouring fluorine nuclei. ^{19}F has a much larger nuclear magnetic moment than ^{35}Cl and ^{37}Cl which posses moments which are $\sim \times 10$ smaller, resulting in reduced dipolar broadening and a narrower resonance.

The α-form of $NaVO_3$ contains two inequivalent Na sites, and quadrupolar lineshapes with parameters listed in table 5.3 were fitted to them. Also listed in table 5.3 are the parameters used by Skibsted who could just about resolve the two lines at a field of 7.1 T[28]. The β-$NaVO_3$ form only contains one inequivalent site, and a degree of β-$NaVO_3$ impurity can be seen in the spectrum of the α-form. Both spectra also exhibit a small impurity peak at 7.2 ppm which could be due to NaCl contamination.

The ^{23}Na spectra of the orthovanadate is clearly a little more complicated, and no attempt has been made to fit quadrupolar lineshapes to it.

5.5.2 Na_2XF_6 (X = Zr, Si, Ti)

Na_2SiF_6 was another compound that was considered as a possible reaction product. Though not strictly relevant from the doped zircon point of view, the ^{23}Na MAS spectra were also acquired for two related compounds, Na_2TiF_6 and Na_2ZrF_6 which are shown in

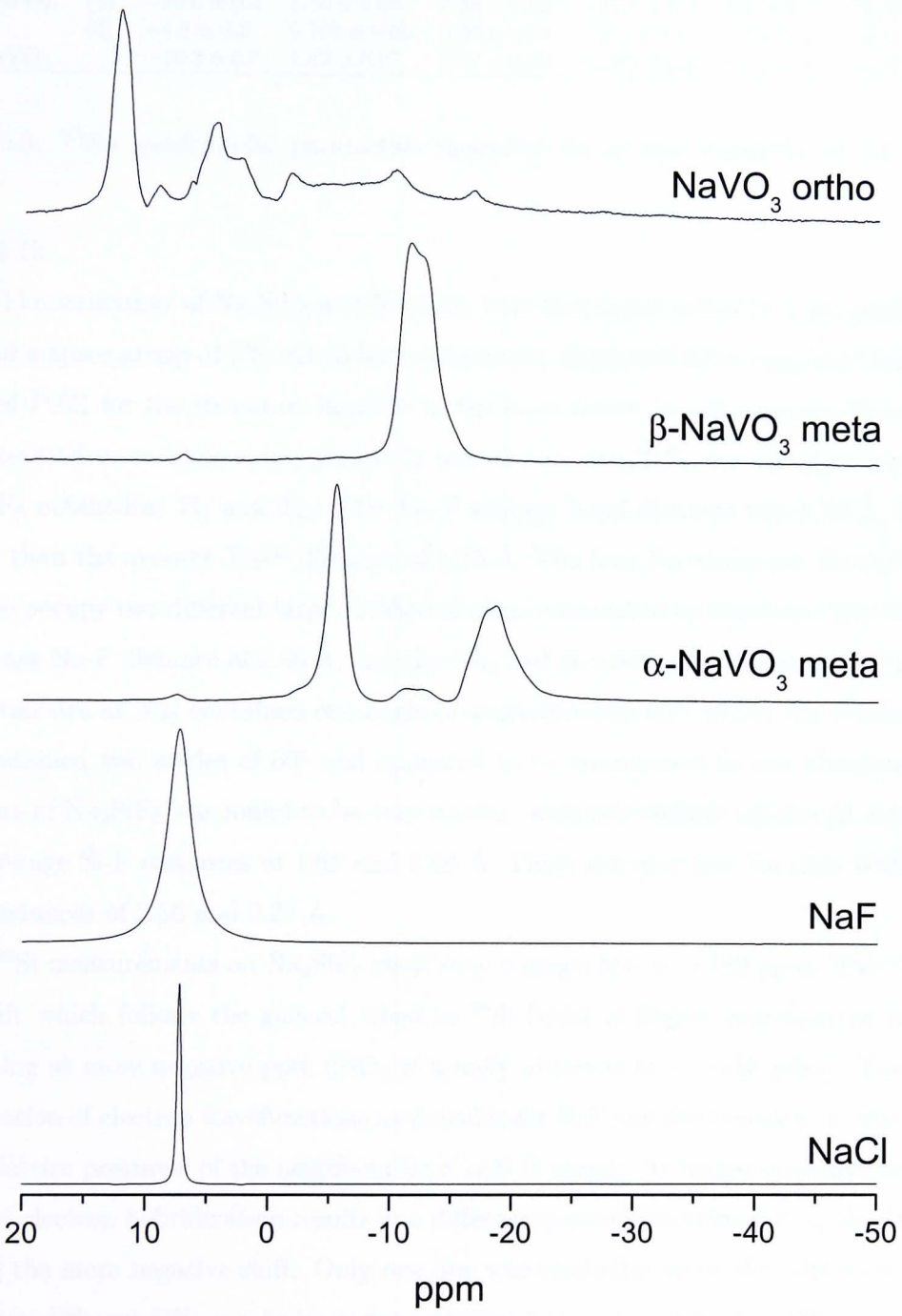

Figure 5.11: ^{23}Na MAS NMR at 14.1 T of sodium reference compounds that may be created during the zircon-forming reaction.

Compound		7.1 T by Skibsted [28] δ_{iso} (ppm)	C_Q (MHz)	η_Q	Work performed here at 14.1 T δ_{iso} (ppm)	C_Q (MHz)	η_Q
α–$NaVO_3$	(1)	-15.6 ± 0.5	1.50 ± 0.05	0.58 ± 0.02	-15.9 ± 0.4	1.5 ± 0.1	0.58 ± 0.1
	(2)	-4.8 ± 0.2	0.765 ± 0.02	0.06 ± 0.02	-5.0 ± 0.4	0.8 ± 0.1	0.31 ± 0.1
β–$NaVO_3$		-10.3 ± 0.3	1.42 ± 0.02	0.27 ± 0.02	-10.1 ± 0.4	1.4 ± 0.1	0.27 ± 0.1

Table 5.3: ^{23}Na quadrupolar parameters measured for α and β-$NaVO_3$ at 7.1 T and 14.1 T.

figure 5.12.

The structures of Na_2SiF_6 and Na_2TiF_6 were first investigated by Cipriani[29] who assigned a space group of $P3/m1$ to both structures. Zalkin[30] later suggested the space group of $P321$ for the structure, however in the most recent investigation by Schäfer[31] the C-centred monoclinic space group $C2$ was chosen. Na_2TiF_6 was found to consist of two TiF_6 octahedra, Ti_1 and Ti_2. The Ti_1-F average bond distance was 1.70 Å, slightly shorter than the average Ti_2-F distance of 1.75 Å. The four Na atoms per unit cell were found to occupy two different large octahedral sites surrounded by fluorines. Site Na_1 had an average Na-F distance of 2.36 Å, and site Na_2 had an average Na-F distance of 2.29 Å. The octahedra at Na_1 contained one angle of approximately 60°, whilst the octahedra at Na_2 contained two angles of 60° and appeared to be compressed in one direction. The structure of Na_2SiF_6 was found to be very similar, with two slightly smaller Si octahedra with average Si-F distances of 1.68 and 1.69 Å. There are also two Na sites with mean Na-F distances of 2.36 and 2.27 Å.

^{29}Si measurements on Na_2SiF_6 show only a single line at -189 ppm. This is large ^{29}Si shift which follows the general trend in ^{29}Si NMR of higher coordination silicates resonating at more negative ppm (SiO_4 is usually observed at ~ -110 ppm). The linear combination of electron wavefunctions responsible for Si-F and Si-O bonding is dependant on the lattice positions of the neighbouring F and O atoms. At higher coordinations, the different electron hybridization results in a different electron wavefunction at the nucleus, causing the more negative shift. Only one line was resolvable since the difference in size of the two different SiF_6 octahedra is not sufficient to cause enough of a shift between the two resonances for them to be resolvable at 7.05 T.

The ^{23}Na spectra of Na_2SiF_6 and Na_2TiF_6 both show two resonances. The shift range is wider for Na_2SiF_6 than for Na_2TiF_6, since the two sodium environments are less

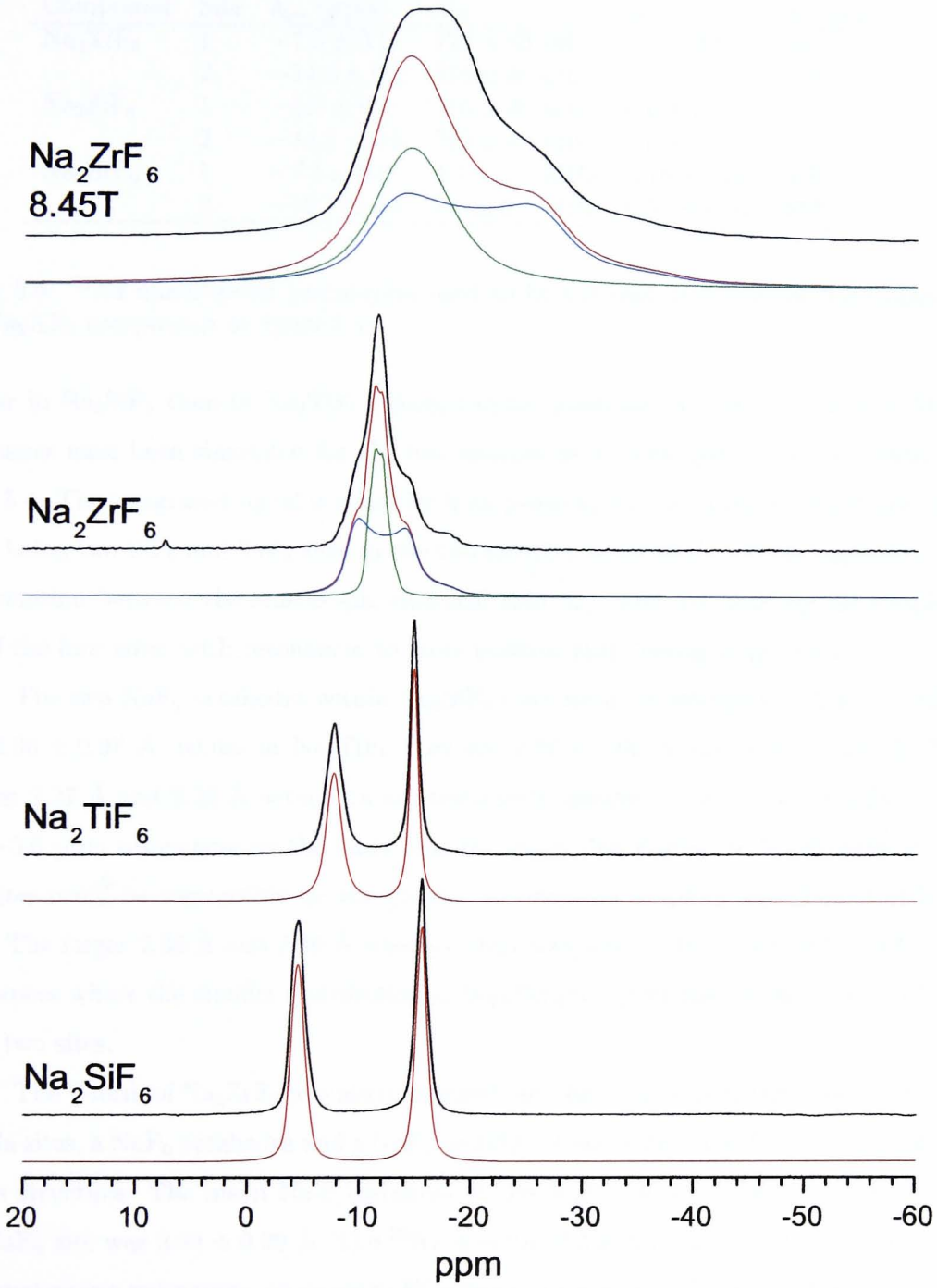

Figure 5.12: ^{23}Na MAS NMR spectra of Na_2XF_6 (X=Zr, Si, Ti) at 14.1 T, and Na_2ZrF_6 at 8.45 T. Two quadrupolar central transition lineshapes have been fitted to both sites in every sample, and the parameters are listed in table 5.4.

Compound	Site	δ_{iso} (ppm)	C_Q	η_Q	Integral
Na_2TiF_6	1	-7.0 ± 0.2	770 ± 50 kHz	0.6 ± 0.1	50%
	2	-14.5 ± 0.2	515 ± 40 kHz	1.0 ± 0.1	50%
Na_2SiF_6	1	-3.6 ± 0.2	915 ± 40 kHz	0.6 ± 0.1	50%
	2	-14.9 ± 0.2	710 ± 40 kHz	1.0 ± 0.1	50%
Na_2ZrF_6	1	-7.5 ± 0.2	2.1 ± 0.1 MHz	0.15 ± 0.05	60%
	2	-10.7 ± 0.4	1.1 ± 0.1 MHz	0.50 ± 0.05	40%

Table 5.4: ^{23}Na quadrupolar parameters used to fit the central transition lineshapes of the Na_2XF_6 compounds in figure 5.12.

similar in Na_2SiF_6 than in Na_2TiF_6. Second-order quadrupolar central transition MAS lineshapes have been simulated for the two resonances in both spectra and are listed in table 5.4. The integrated signal is equal for both peaks in the two spectra, consistent with there being two SiF_6 and TiF_6 sites in the two samples respectively. There appears to be a correlation between the anisotropic chemical shift δ_{iso}, and the quadrupolar coupling C_Q of the four sites, with resonances to more positive ppm having larger C_Qs.

The two NaF_6 octahedra within Na_2SiF_6 have mean bondlengths of 2.27 ± 0.09 Å and 2.36 ± 0.07 Å, whilst in Na_2TiF_6 they are 2.29 ± 0.06 Å and 2.36 ± 0.05 Å. The smaller 2.27 Å and 2.29 Å octahedra are tentatively assigned to the more positive -7.0 and -3.6 ppm resonances on the basis that the larger distribution in bondlength at the two sites could be responsible for the greater quadrupolar coupling experienced at both sites. The larger 2.35 Å and 2.36 Å sites are then assigned to the -14.9 and -14.5 ppm resonances where the smaller distribution in bondlengths gives rise to the smaller C_Q at these two sites.

The γ-form of Na_2ZrF_6 was also examined, and the crystal structure again contains two Na sites, a NaF_6 octahedra and a NaF_7 unit[32]. A space group of $P21/c$ was assigned to the structure. The mean Na-F distances at the NaF_7 site was 2.38 ± 0.15 Å and at the NaF_6 site was 2.34 ± 0.08 Å. The ^{23}Na spectra of Na_2ZrF_6 at 14.1 T shows at least two overlapping resonances, so an extra ^{23}Na experiment was performed at 8.45 T to help elucidate the lines. Simulation of the lineshapes at both fields was possible using purely second-order quadrupolar central transition lineshapes (figure 5.12), and the quadrupolar parameters used are listed in table 5.4. The two spectra clearly show the advantage of employing higher magnetic fields to increase resolution in quadrupolar lineshapes.

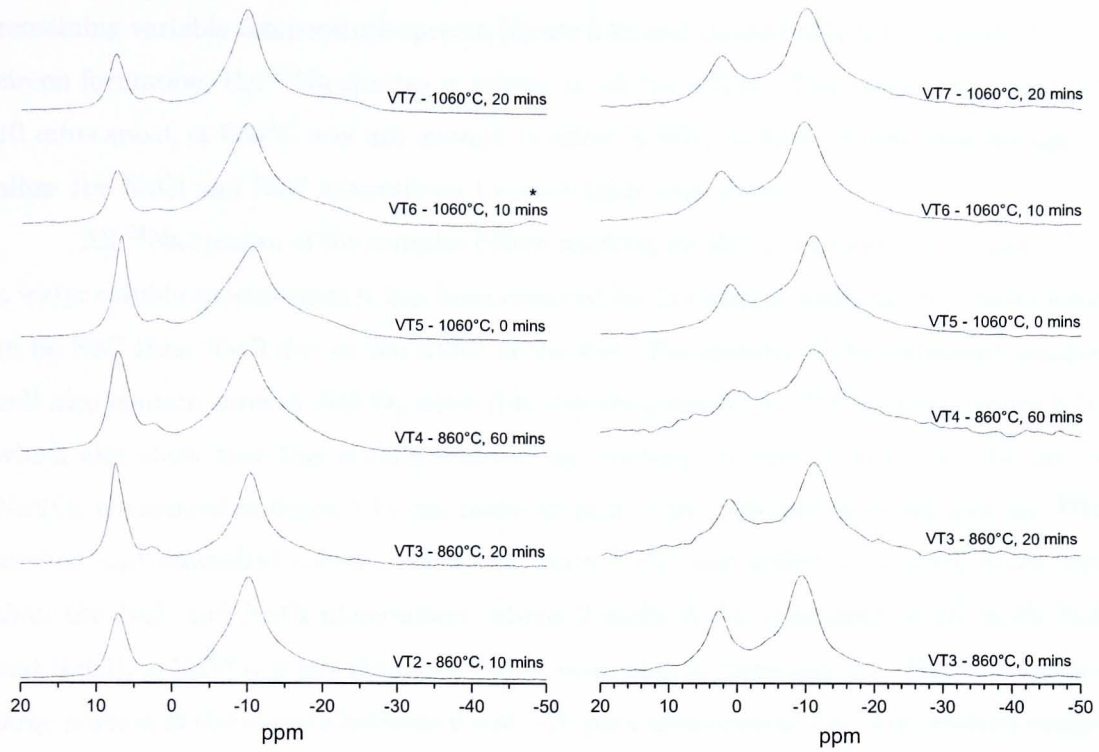

Figure 5.13: ^{23}Na spectra of vanadium-doped zircons fired under different conditions before washing (left) and after washing with water (right).

The average Na-F bond distance at both sites is quite similar and this is reflected in the similarity between δ_{iso} for the two resonances. On the basis of the NaF_7 site having a greater distribution in bond length, this site is tentatively assigned to the higher C_Q resonance at -7.5 ppm. The -10.7 ppm site must then be due to the NaF_6 site. The integrated signal for both sites is slightly short of the expected 1:1 ratio for the two sites. This is unlikely to be due to preferential excitation of the two quadrupolar broadened resonances since the lower C_Q -10.7 ppm resonance would then exhibit the greater signal.

5.5.3 The effect of variable firing times

Figure 5.13 shows the MAS ^{23}Na spectra of the variable firing time V-$ZrSiO_4$ samples acquired at 14.1 T under the same conditions as the reference compounds. The spectra have not been scaled to reflect the reduction in ^{23}Na signal measured after firing. It is

interesting to note that although the ^{29}Si spectrum for VT2 was very different than the remaining variable temperature spectra (figure 5.4) and showed only SiO_2 species with no zircon formation, the ^{23}Na spectra is similar to all the others. This means that although 10 mins spent at 860°C was not enough to allow $ZrSiO_4$ to form, it was long enough to allow the NaCl and NaF mineralisers to reach their final state.

All ^{23}Na spectra of the samples before washing exhibit a resonance at 7.2 ppm. It is a water soluble species since it has been removed by the sample washing. It is more likely to be NaF than NaCl due to the width of the line. The spectra of the unwashed samples will also contain some α-$NaVO_3$ since this was observed in the ^{51}V spectra (figure 5.10) which also show that this is then removed by washing. It can be seen that the two α-$NaVO_3$ resonances in figure 5.11 can make up part of the difference between any two ^{23}Na washed and unwashed spectra. However, since V_2O_5 was added at a much lower level than the NaF and NaCl mineralisers (about 3 mol% V_2O_5 compared to 10 mol% NaF and NaCl), α-$NaVO_3$ is not the main ^{23}Na species seen in these spectra. This still leaves a large portion of the spectra between 0 and -20 ppm unaccounted for. Any washed-sample spectrum cannot contain any V^{5+}-containing sodium species since none are observed in the washed ^{51}V spectra, and because vanadium is added at a much lower level than the sodium. Another set of species that could be created are sodium silicates, however these have only been observed in the 8 to 23 ppm region [33, 34], and do not manifest themselves in the ^{29}Si spectra.

Although it has not been possible to completely deconvolve the ^{23}Na spectra here, it can be seen that NaF is certainly formed, and that the same set of relatively disordered sodium species are created, independent of firing time and temperature. It can also be seen that even though the sample was thoroughly washed with water, some insoluble sodium species are still left within the pigment.

5.6 ^{17}O enriched vanadium doped sol-gel

The ^{17}O MAS NMR spectra of sol-gel formed V-$ZrSiO_4$ before firing is shown at applied magnetic fields varying from 5.6 to 14.1 T in figure 5.14. The resonances are best resolved at high field and four sites can be readily distinguished. At the highest field, the peaks at

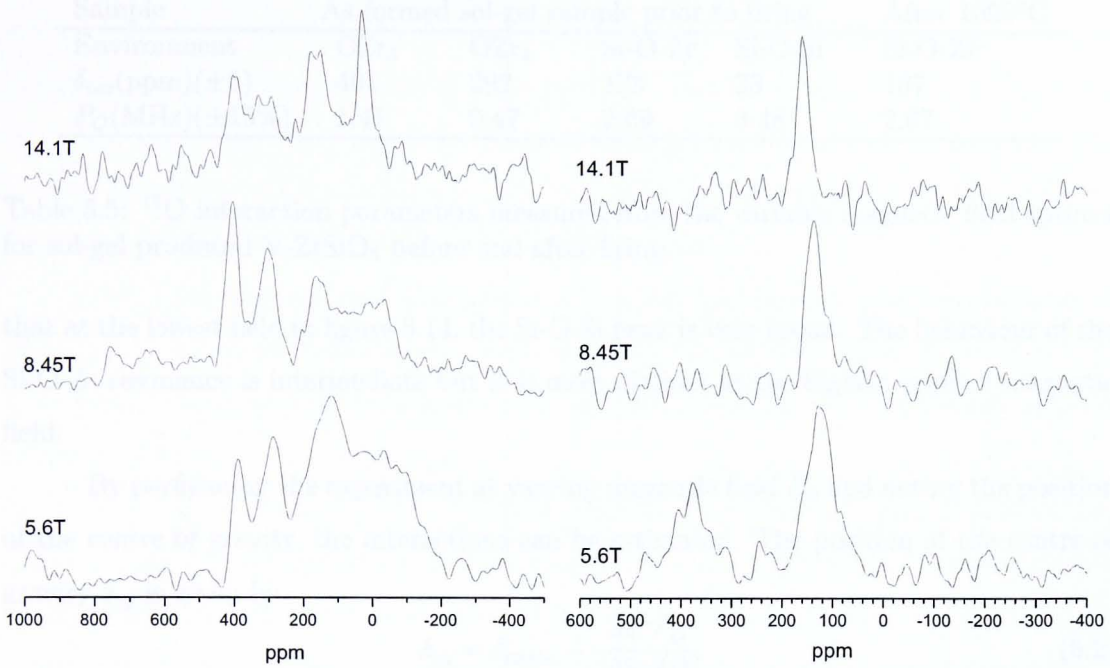

Figure 5.14: ^{17}O spectra of 10% ^{17}O enriched vanadium-doped zircon sol-gel at multiple fields before firing (left) and after firing at 1000°C for 30 mins (right).

400 and 310 ppm correspond to OZr_3 and OZr_4 environments respectively[35, 36]. The resonance at 30 ppm has been seen in other mixed gels and is due to Si-O-Si[37] and the 160 ppm resonance is from crosslinking between Zr and Si to give Zr-O-Si bonds[38, 39]. All the peaks shift to lower ppm at decreasing field strength, since the effect of the contribution from the second-order quadrupolar induced shift to the observed peak position is greater at lower field. The spectra change their superficial appearance as the applied magnetic field varies because the dominant line-broadening interactions of the different environments are not the same. In such materials it is generally found that in ^{17}O MAS NMR spectra, the two residual line-broadening mechanisms tend to be chemical shift dispersion and second-order quadrupole effects. In the more ionic environments of the OZr_3 and OZr_4, chemical shift dispersion dominates. This scales (in Hz) directly with the applied magnetic field, and these peaks become better defined at lower magnetic fields. The Si-O-Si ^{17}O NMR signal is dominated by second-order quadrupolar effects, and the linewidth (in Hz) scales inversely with the applied magnetic field. It can be seen

Sample	As formed sol-gel sample prior to firing				After 1000°C
Environment	OZr_3	OZr_4	Si-O-Zr	Si-O-Si	Si-O-Zr
δ_{iso}(ppm)(±5)	401	292	173	33	167
P_Q(MHz)(±15%)	1.41	0.47	2.69	3.48	2.67

Table 5.5: ^{17}O interaction parameters measured from the variable magnetic field spectra for sol-gel produced V-$ZrSiO_4$ before and after firing.

that at the lowest field in figure 5.14, the Si-O-Si peak is very broad. The behaviour of the Si-O-Zr resonance is intermediate but it is most distinct at the highest applied magnetic field.

By performing the experiment at varying magnetic field B_0 and noting the position of the centre of gravity, the interactions can be estimated. The position of the centre of gravity δ_{cg} is given by

$$\delta_{cg} = \delta_{cs,iso} - \frac{3\pi^2 P_Q^2}{125\gamma^2 B_0^2} \tag{5.2}$$

where P_Q, the quadrupole effect parameter defined as

$$P_Q = C_Q\sqrt{1+\frac{\eta^2}{3}} \tag{5.3}$$

where C_Q is the quadrupole coupling constant and η is the quadrupole asymmetry parameter. When the lineshape cannot be observed, only the combination of C_Q and η can be deduced. Using the variable applied magnetic field data the isotropic chemical shift δ_{iso} and P_Q can be estimated (table 5.5). The expected decrease of P_Q with increasing ionicity is observed. The ^{17}O NMR data clearly shows a highly disordered structure in the initial gel with all possible linkages present. The other implication of this data is that the Zr-O-Zr present have shifts consistent with the local environment being monoclinic-like. Monoclinic structures contain both OZr_3 and OZr_4 environments close to the shifts observed in the ratio 1:1. This is not necessarily implying that there are regions that could be detected for example by diffraction as monoclinic. However, the very local electron density in the bonds means that the oxygen is monoclinic-like. This is a common observation of gel formed zirconia-containing samples that the initial amorphous gel contains monoclinic-like Zr-O-Zr bonds[36, 40].

The ^{17}O-enriched sample was then heated in air at 1000°C for 30 minutes. The NMR spectrum at various fields is plotted in figure 5.14 which shows a single peak,

although the amount of signal from the sample is reduced since some of the ^{17}O in the sample has exchanged with ^{16}O in the air during firing. From XRD measurements, all the ZrO_2 and SiO_2 have reacted to leave $ZrSiO_4$. This is confirmed by the ^{17}O NMR spectrum where only the peak at $\sim$ 160 ppm corresponding to Si-O-Zr crosslinking can be seen. Since the amount of vanadium in the lattice is quite small, there is insufficient intensity to be able to directly detect V-O-(Si,Zr) bonds.

^{29}Si measurements were also performed on the fired sample, and the spectrum is identical to the usual zircon spectra with three contact shifted peaks (figure 5.3). So after firing, the same V-$ZrSiO_4$ system has been produced as that synthesised through the ceramic route.

The ^{17}O spectrum of fired V-$ZrSiO_4$ performed at 5.6 T in figure 5.14 also contains an extra, broad resonance at 400 ppm. This is not present at higher fields since the interaction giving rise to the width of the line is likely to be due to chemical shift anisotropy. At higher fields, the range of frequencies this lineshape covers becomes wider, making detection harder. This is a good example of a lower magnetic field being more suitable for acquiring spectra of CSA-dominated lineshapes, and higher magnetic fields being suitable for observing second-order quadrupolar broadened resonances.

5.7 ^{19}F NMR

The role of the NaF mineraliser was further investigated by performing ^{19}F MAS NMR on a V-doped zircon. Although ^{19}F is a very receptive nucleus, homonuclear dipolar coupling between ^{19}F nuclei causes line broadening, a similar problem to that encountered in solid state ^{1}H NMR. This has prevented the solid state study of ^{19}F becoming a routine experiment, however the NMR literature on ^{19}F has been reviewed by Miller[41] and Harris[42].

Since a number of plastic components commonly used in solid state NMR probes contain ^{19}F, a probe designed for ^{19}F NMR study, which has a lower ^{19}F background signal was used. This still yielded spectra with a smaller background ^{19}F signal, so an experiment on an empty rotor also needed to be performed to measure the background signal, which was then subtracted from spectra.

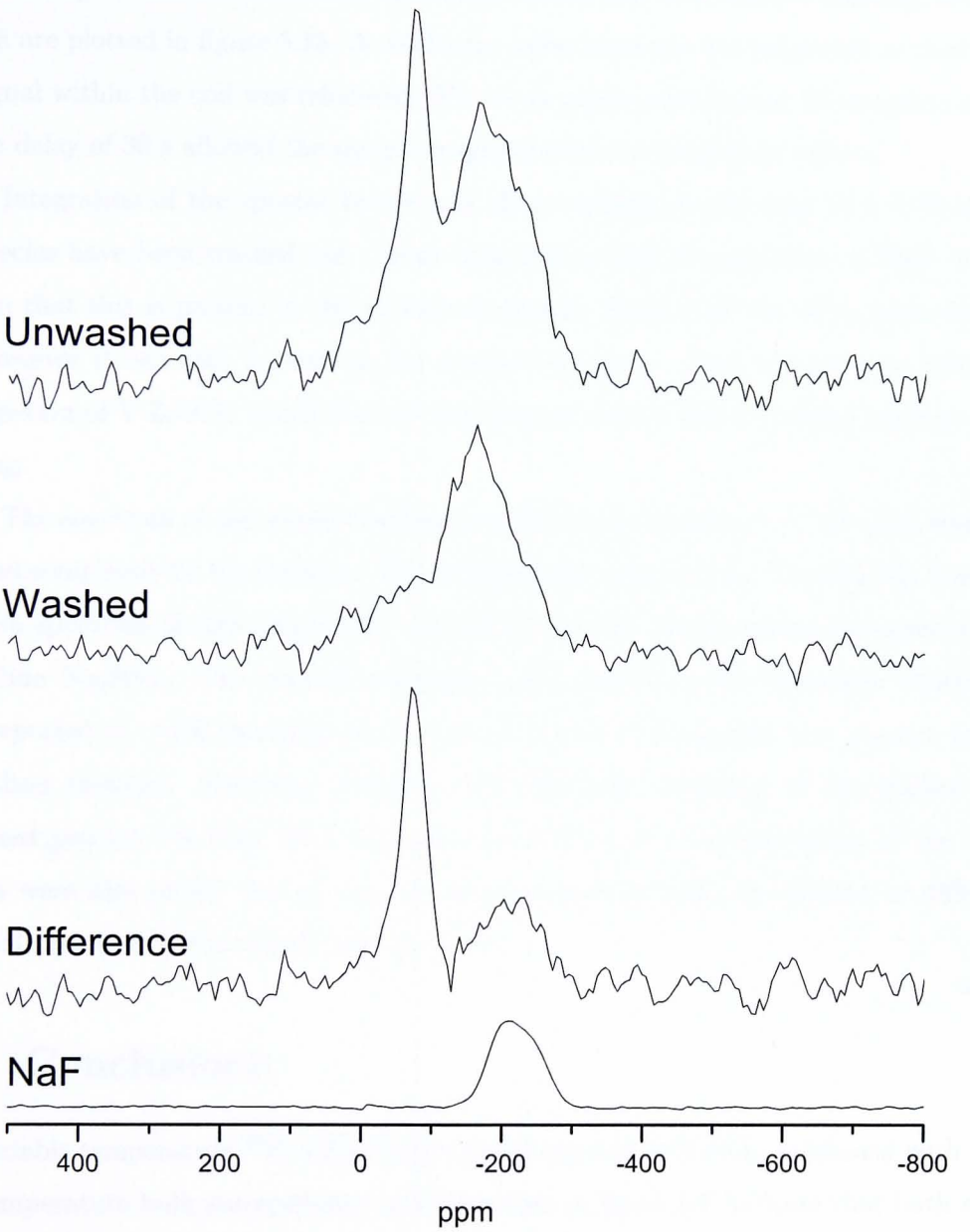

Figure 5.15: ^{19}F MAS NMR measurements performed at 8.45 T on V-$ZrSiO_4$. Plotted are the spectra before and after sample washing, and the difference between the two spectra to help elucidate the species which have been removed by washing. Also plotted is a separate spectra of crystalline NaF for comparison.

Figure 5.15 shows the ^{19}F spectra acquired for a typical V-$ZrSiO_4$ pigment, sample VT4 which had the commercially used optimum amount of V_2O_5 pigment source. Experiments were performed at 8.45 T on the sample before and after sample washing, and the spectra are plotted in figure 5.15. A solid echo pulse sequence was employed so that only ^{19}F signal within the coil was refocused. Two 8 μs pulses were spaced 10 μs apart, and a recycle delay of 30 s allowed the sample magnetisation to completely recover.

Integration of the spectra before and after washing reveals that 44 ± 5 % of the ^{19}F species have been washed out. From comparison with the spectrum of NaF, it can be seen that this is present in the unwashed sample. Some NaF has then been washed out, however it can still be seen in the washed spectrum. This is consistent with the ^{23}Na spectra of V-$ZrSiO_4$ which showed NaF present before, and a reduced amount after washing.

The spectrum of the washed sample contains a main peak at ~ -150 ppm which is removed completely by the washing. This shift has been reported for Na_2SiF_6[43], however the ^{23}Na spectrum of this sample did not exhibit the two sharp resonances expected for crystalline Na_2SiF_6. The washed spectrum could contain a KF resonance which has been reported at -133 ppm[44], since a small source of potassium was present in the mineraliser mixture. However, complete unambiguous elucidation of the washed and unwashed spectra has only been partially successful here. Deconvolution of the ^{23}Na spectra were also partly due to the complication arising from the number of different chemical phases that the mineralisers can exist in.

5.8 Conclusions

The variable temperature ^{29}Si MAS NMR experiments on V-$ZrSiO_4$, combined with variable temperature bulk susceptibility measurements in figure 5.7 indicate that both additional peaks in the ^{29}Si spectra are shifted via a through-space Fermi contact mechanism. The strongly shifted -105 ppm resonance is likely to be due to V^{4+} substituting at a ZrO_8 site, so the hyperfine interaction is transferred via a single intermediate oxygen (Si-O-V). The weakly shifted line is then due to V^{4+} at a Si site, since three intermediate sites are required to transfer the interaction (V-O-Zr-O-Si). This assignment supports the doping

of V^{4+} at both ZrO_8, and the smaller SiO_4 sites. Of the wide variety of experiments which have previously been performed to elucidate the nature of V^{4+} doping in V-$ZrSiO_4$, MAS NMR provides a unambiguous method of quantifying V^{4+} occupation at the two cation sites. From measuring the integrals of the two contact shifted peaks, $N_T/N_D = 1.2 \pm 0.2$. This is in best agreement with the recent EXAFS experiments performed by Ocaña[17], where $N_T/N_D = 1.6$.

The gradients of the lines fitted in figure 5.7 correspond to the hyperfine field at the V^{4+} site. The origin of the difference in the signs of the two hyperfine fields is unclear. One possibility is that it is an effect resulting from the crystal structure of zircon, and the different orientations of the SiO_4 and ZrO_8 sites with respect to the probe ^{29}Si site.

Figure 5.3 of the ^{29}Si MAS NMR spectra of V-$ZrSiO_4$ produced using varying amounts of V_2O_5 source shows that complete zircon formation only occurs when a very precise amount of V_2O_5 is present. ^{51}V MAS NMR of the same samples also indicate that when the optimum amount of V_2O_5 is used, only a single α-Na_2VO_3 V^{5+}-containing phase is observed. Either side of this equilibrium amount, another unidentified vanadium containing phase is also produced. This effect is likely to be due to the role of V_2O_5 as a fluxing agent as well as a pigment source. When it is not present in the equilibrium amount, the different chemistry of the system means that it cannot act as a flux, and so firing the sample at 860°C is insufficient for the reaction to complete.

The ^{51}V MAS NMR spectra in Figure 5.10 indicate that α-Na_2VO_3 is present in V-$ZrSiO_4$ at a dilute level, undetectable by routine X-ray diffraction. Since α-Na_2VO_3 is present only in the ^{51}V MAS NMR spectra of V-$ZrSiO_4$ before sample washing, it is being completely removed by sample washing with water.

From the ^{23}Na MAS NMR of the V-$ZrSiO_4$ samples before and after washing in figure 5.13, it can be seen that NaF is present in the V-$ZrSiO_4$ samples before washing. Most NaF is then removed by sample washing, and this is confirmed by the ^{19}F measurements in figure 5.15. However, the chemical shift range of ^{23}Na does not appear to be sensitive enough to allow elucidation any other sodium containing species.

References

[1] M. Llusar, J. B. Vicent, J. Badenes, M. A. Tena and G. Monrós, Environmental optimisation of blue vanadium zircon ceramic pigment, *Journal of the European Ceramic Society*, **19** 2647 (1999).

[2] C. A. Seabright, United States Patent 2441447 (1948).

[3] V. I. Matkovich and P. M. Corbett, Formation of zircon from zirconium dioxide and silicon dioxide in the presence of vanadium pentoxide, *Journal of the American Ceramic Society*, **44** 130 (1960).

[4] J. B. Vicent, J. Badenes, M. Llusar, M. A. Tena and G. Monrós, Differentiation between the green and Turkish blue solid solutions of vanadium in a zircon lattice obtained by the sol-gel process. *Journal of Sol-Gel Science and Technology*, **13** 347 (1998).

[5] T. Demiray, D. K. Nath and F. A. Hummel, Zircon-Vanadium Blue Pigment, *Journal of the American Ceramic Society*, **53** 1 (1970).

[6] S. Di Gregorio, M. Greenblatt, J. H. Pifer and M. D. Sturge, An ESR and optical study of V^{4+} in zircon-type crystals, *Journal of Chemical Physics*, **76** 2931 (1982).

[7] H. Xiaoyu, B. Gui-ru and Z. Min-guang, The study of the optical and the EPR spectra of V^{4+} in zircon-type crystals, *Journal of Physical Chemistry in Solids*, **46** 719 (1985).

[8] K. B. Lyons, M. D. Sturge and M. Greenblatt, Low-frequency Raman spectrum of $ZrSiO_4$:V^{4+}: An impurity-induced dynamical distortion, **30** 2127 (1984).

[9] D. de Waal, A. M. Heyns, G. Pretorius and R. J. H. Clark, Raman spectroscopic investigations of $ZrSiO_4$:V^{4+}, the blue vanadium pigment, *Journal of Raman Spectroscopy*, **27** 657 (1996).

[10] P. Chandley, R. J. H. Clark, R. J. Angel and G. David Price, Site Preference of Vanadium doped into $ZrSiO_4$ and $ZrGeO_4$ and of Terbium doped into $ZrGeO_4$, *Journal of the Chemical Society Dalton Transactions*, **9** 1579 (1992).

[11] A. Beltrán, S. Bohm, A. Flores-Riveros, J. A. Igualada, J. Andrés, V. Luaña and A. Martín Pendás, Ab initio cluster-in-the-lattice description of vanadium-doped zircon. Analysis of the impurity centres V^{4+}:$ZrSiO_4$, *Journal of Physical Chemistry*, **97** 2555 (1993).

[12] G. Monros, J. Carda, P. Escribano and J. Alarcon, Synthesis of V-$ZrSiO_4$ solid solutions, *Journal of Materials Science Letters*, **9** 184 (1990).

[13] P. Tartaj, C. J. Serna and M. Ocaña, Preparation of Blue Vanadium-Zircon Pigments by Aerosols Hydrolysis, *Journal of the American Ceramic Society*, **78** 1147 (1995).

[14] C. Valentín, M. C. Muñoz and J. Alarcón, Synthesis and characterization of vanadium-containing $ZrSiO_4$ solid solutions from gels, *Journal of Sol-Gel Science and Technology*, **15** 221 (1999).

[15] F. Jose Torres, J. M. Amigó and J. Alercón, Rietveld Refinement of Tetragonal V^4-ZrO_2 Solid Solutions Obtained from Gels by X-Ray Powder Diffraction, *Journal of Solid State Chemistry*, **163** 33 (2002).

[16] C. Valentín, J. V. Folgado and J. Alarcón, Low-temperature metastabilization of tetragonal V^{4+}-containing ZrO_2 solid solutions, *Materials Research Bulletin*, **36** 1615 (2001).

[17] M. Ocaña, A. R. Gonzàlez-Elipe, V. M. Ocera, P. Tartaj and C. J. Serna, Spectroscopic studies of the localization of vanadium(IV) in vanadium-doped zircon pigments, *Journal of the American Ceramic Society*, **81** 395 (1998).

[18] L. Rubio-Puzzo, M. C. Caracoche, M. M. Cervera, P. C. Rivas, A. M. Ferrari and F. Bondioli, Hyperfine characterization of pure and doped zircons, *Journal of Solid State Chemistry*, **150** 14 (2000).

[19] J V. Smith and C. S. Blackwell, Nuclear magnetic resonance of silica polymorphs. *Nature*, **303** 223 (1983).

[20] M. Mägi, E. Lippmaa, A. Samoson, G. Engelhardt and A. R. Grimmer, Solid-state high resolution silicon-29 chemical shifts in silicates, *Journal of Physical Chemistry*, **88** 1518 (1984).

[21] I. Farnan and E. K. H. Salje, The degree and nature of radiation damage in zircon observed by ^{29}Si nuclear magnetic resonance, *Journal of Applied Physics*, **89** 2084 (2001).

[22] M. Bak, J. T. Rasmussen and N. C. Nielsen, SIMPSON: A general simulation program for solid-state NMR spectroscopy, *Journal of Magnetic Resonance*, **147** 296 (2000).

[23] H. Eckert and I. E. Wachs, Solid-state V-51 NMR structural studies on supported vanadium(V) oxide catalysts-vanadium-oxide surface-layers on alumina and titania supports, *Journal of Physical Chemistry*, **93** 6796 (1989).

[24] F. D. Hardcastle, I. E. Wachs, H. Eckert and D. A. Jefferson, Vanadium(V) environments in bismuth vanadates - a structural investigation using Raman-spectroscopy and solid-state V-51 NMR. *Journal of Solid State Chemistry*, **90** 194 (1991).

[25] J. Skibsted, C. J. H. Jacobsen and H. J. Jakobsen, ^{51}V Chemical Shielding and Quadrupolar Coupling in Ortho- and Metavanadates from ^{51}V MAS NMR Spectroscopy, *Inorganic Chemistry*, **37** 3083 (1998).

[26] U. G. Nielsen, J. Skibsted and H. J. Jakobsen, $\beta-VO_2$ - a V(IV) or mixed-valence V(III)-V(V) oxide - studied by ^{51}V MAS NMR Spectroscopy, *Chemical Physics Letters*, **356** 73 (2002).

[27] F. Delmaire, M. Rigole, E. A. Zhilinskaya, A. Aboukaïs, R. Hubaut and G. Mairesse, ^{51}V magic angle spinning solid state NMR studies of $Bi_4V_2O_{11}$ in oxidized and reduced states, *Physical Chemistry Chemical Physics*, **2** 4477 (2000).

[28] J. Skibsted, N. C. Nielsen, H. Bildsøe and H. J. Jakobsen, Magnitudes and Relative Orientation of ^{51}V Quadrupole Couplings and Anisotropic Shielding Tensors in Metavanadates and KV_3O_8 from ^{51}V MAS NMR Spectra. ^{23}Na Quadrupole Coupling Parameters form $\alpha-$ and $\beta-NaVO_3$, *Journal of the American Chemical Society*, **115** 7351 (1993).

[29] C. Cipriani, Richerche strutturistiche e cristallochimiche sul fluotitanto di sodio, *Period. Mineral*, **24** 361 (1955).

[30] A. Zalkin, J. D. Forrester and D. H. Templeton, The crystal structure of sodium fluorosilicate, *Acta Crystallographica*, **17** 1408 (1964).

[31] G. F. Schäfer, The crystal structures of Na_2TiF_6 and Na_2SiF_6. Pseudotrigonal polar phases in double hexafluorides of the type $(Me^I)_2Me^{IV}F_6$, *Zeitschrift für Kristallographie*, **175** 277 (1986).

[32] G. Brunton, The crystal structure of $\gamma-Na_2ZrF_6$, *Acta Crystallographica B*, **25** 2164 (1969).

[33] X. Y. Xue and J. F. Stebbins, Na-23 NMR chemical-shifts and local Na coordination environments in silicate crystals, melts And glasses *Physics and Chemistry of Minerals*, **20** 297 (1993).

[34] H. Koller, G. Engelhardt, A. P. M. Kentgens and J. Sauer, Na-23 NMR-spectroscopy of solids - Interpretation of quadrupole interaction parameters and chemical-shifts, *Journal of Physical Chemistry*, **98** 1544 (1994).

[35] O. B. Lapina, V. M. Mastikhin, A. A. Shubin, V. N. Krasilnikov and K. I. Zamaraev, V-51 Solid state NMR studies of vanadia based catalysts, *Progress in Nuclear Magnetic Resonance Spectroscopy*, **24** 457 (1992).

[36] T. J. Bastow and S. N. Stuart, O-17 NMR in simple oxides, *Chemical Physics*, **143** 459 (1990).

[37] T. J. Bastow, M. E. Smith and H. J. Whitfield, Characterisation of zirconia gels by O-17 nuclear magnetic resonance, *Journal of Materials Chemistry*, **2** 989 (1992).

[38] O-17 and Si-29 solid-state NMR-study of atomic-scale structure in sol-gel-prepared TiO_2-SiO_2 materials, P. J. Dirken, M. E. Smith and H. J. Whitfield, *Journal of Physical Chemistry*, **99** 395 (1995).

[39] P. J. Dirken, R. Dupree and M. E. Smith, Structural role of zirconium in SiO_2-ZrO_2 gels - Evidence from O-17 NMR, *Journal of Materials Chemistry*, **5** 1261 (1995).

[40] D. M. Pickup, G. Mountjoy, G. W. Wallidge, R. J. Newport and M. E. Smith, Structure of $(ZrO_2)_x(SiO2)_{(1-x)}$ xerogels (x=0.1, 0.2, 0.3 and 0.4) from FTIR, Si-29 and O-17 MAS NMR and EXAFS, *Physical Chemistry Chemical Physics*, **1** 2527 (1999).

[41] J. M. Miller, Fluorine-19 magic-angle spinning NMR, *Progress in NMR Spectroscopy*, **28** 255 (1996).

[42] R. K. Harris and P. J. Jackson, High-resolution Fluorine-19 magnetic resonance of solids, *Chemical Reviews*, **91** 1427 (1991).

[43] J. F. Stebbins and Q. Zeng, Cation ordering at fluoride sites in silicate glasses: a high-resolution ^{19}F NMR study, *Journal of Non-Crystalline Solids*, **262** 1 (2000).

[44] T. Schaller, D. B. Dingwell, H. Keppler, W. Knoller, L. Merwin and A. Sebald, Fluorine in silicate-glasses - a multinuclear nuclear-magnetic-resonance study, *Geochimica et Cosmochimica Acta*, **56** 701 (1992).

Chapter 6

Silver compounds and glasses

6.1 Introduction

6.1.1 Silver glasses

Silver glasses are used commercially for enamel decoration. A glass is prepared by heating various oxides, typically containing SiO_2, Na_2O, B_2O_3 and Al_2O_3 and a small quantity of ($\sim$ 5 mol%) of AgO, to 1500°C. Once these have melted, the mixture is quenched in water to lock in the glass structure. This glass is then ground and mixed with a pigment material, before being mixed with a suitable carrier medium. The ink produced is then either screen-printed directly onto glass, or indirectly via a transfer to tableware. Upon firing, the glass melts and flows around the pigment to form an enamel coating. The resulting decoration will be a pink colour, and is mainly used for providing durable decorations for tableware[1].

6.1.2 ^{109}Ag NMR

There has been little ^{109}Ag solution or solid state NMR performed despite the ^{107}Ag and ^{109}Ag isotopes being 52% and 48% abundant (table 3.2). The main experimental difficulty is that both isotopes have low gyromagnetic ratios, and at a field of 8.45 T will resonate at only 14.57 and 16.75 MHz respectively. The low gyromagnetic ratios compromise sensitivity since the receptivity scales as γ^3, and there is also the added complication of longer probe coil ringdown times at lower frequencies ($t_{dead} \sim Q/\pi\nu_0$, where ν_0 is the

carrier frequency). Broader resonances will suffer signal distortion resulting from the experimental deadtime t_{dead} at the beginning of the acquisition. The two isotopes are both spin $I = \frac{1}{2}$ and T_1 relaxation is through CSA, dipolar and thermal mechanisms. The ^{109}Ag isotope was usually examined as the gyromagnetic ratio is slightly higher than for ^{107}Ag.

Solid state ^{107}Ag and ^{109}Ag NMR reported to date has recently been reviewed by Smith[2, 3]. One of the first ^{109}Ag solid state NMR studies was performed by Looser[4] who measured the chemical shifts of four silver halides. Measurements were also performed on superionic conductors, and it is fast ion conductors which have received the most attention in the literature since. This is partly because of the current level of scientific interest in ionic conductors, and it is also because relaxation of the mobile Ag ions in these systems can lead to much quicker T_1 times of less than 1 second[5, 6]. These systems are then not hampered by one of the main experimental difficulties in performing ^{107,109}Ag NMR which is the long T_1 times involved.

Silver is a heavy metal which causes it to have a large chemical shift range of about 1000 ppm, and has the potential to be a sensitive indicator of local environment. The ^{109}Ag chemical shift has been used in some silver glass systems to find out which elements the silver is bonded to[7]. The ^{109}Ag powder pattern for other glass systems has also been used to investigate the degree of crystallisation[8].

6.2 Silver reference compounds

Before attempting ^{109}Ag NMR on silver glasses, preliminary NMR studies were conducted at 8.45 T. A Bruker 7 mm DB low-γ probe was used to perform experiments at this field, and an extra capacitance of 60 pF needed to be added in parallel with the tuning variable capacitor to tune the probe to 16.75 MHz. The coil in this probe was constructed from silver so the probe could not be used to observe metallic silver within samples. A separate probehead was constructed for a Bruker static probe which had a coil made from copper. Again, extra capacitance needed to be added to the probehead to enable it to tune to both silver isotopes, and a Q of 390 was measured for it. Background measurements with no sample revealed no metallic silver signal for this probe.

Sample	δ_{iso} (ppm)	Δ (ppm)	Other reports (ppm)	Reference
$AgNO_3$ solution	0	3.2 ± 0.5		
$AgNO_3$ powder	-97 ± 0.5	0.8 ± 0.2	-87	[9]
Ag_2SiO_3	309 ± 7	90 ± 20		
Ag_2CO_3	346 ± 1	9 ± 3		
AgI	760 ± 3	15 ± 3	710 ± 15, 680, 728	[4] [8] [10]
Silver metal	5224 ± 10	12 ± 2	5253	[9]

Table 6.1: Summary of ^{109}Ag shifts and linewidths observed at 8.45 T.

Since the primary reference compound, aqueous $AgNO_3$ has a T_1 time of $\sim$ 300 s, 90° pulse measurements were conducted using the ^{39}K resonance of KBr which has a similar γ to ^{109}Ag, resonating at 16.76 MHz at a field of 8.45 T.

Figure 6.1 shows the initial ^{109}Ag NMR performed at 8.45 T on a variety of silver compounds. All samples were spun at 4.5 kHz in the Bruker 7 mm probe with the exception of (a) aqueous $AgNO_3$ solution, which was static. All spectra were acquired using a single 3 μs pulse to tip the magnetisation 30°, and a recycle delay of 5 mins. The peak positions of all the lines are listed in table 6.1 along with any shifts already reported for these lines in the literature. The metallic silver resonance was acquired using the modified static probe and a $4 - \tau - 8$ μs echo sequence. Since the Knight shift interaction provides an efficient means of T_1 relaxation, a pulse delay of 1 s was sufficient for complete relaxation. The resonance is not plotted in figure 6.1 as the contribution from the Knight shift interaction has moved it far away from the remaining resonances.

The $AgNO_3$ powder line is in reasonable agreement with the only other measurement performed. The solid line is much narrower than the solution line. This could be due to the room temperature shims not being optimally setup for the 7 mm probe. The solid line is then likely to be narrower since the sample spinning has partially averaged out the field inhomogeneities due to the shimming.

The crystal structure of Ag_2SiO_3 has been determined to contain two inequivalent Ag sites, with space group P 21 21 21[11]. The Ag_2SiO_3 spectra took ten days to acquire since the line is 90 ppm wide, and it is not possible to resolve the two inequivalent sites. This is likely to be because the sample is relatively amorphous, and only a faint XRD signal was measured for the sample. The shift of 309 ppm is similar to the only

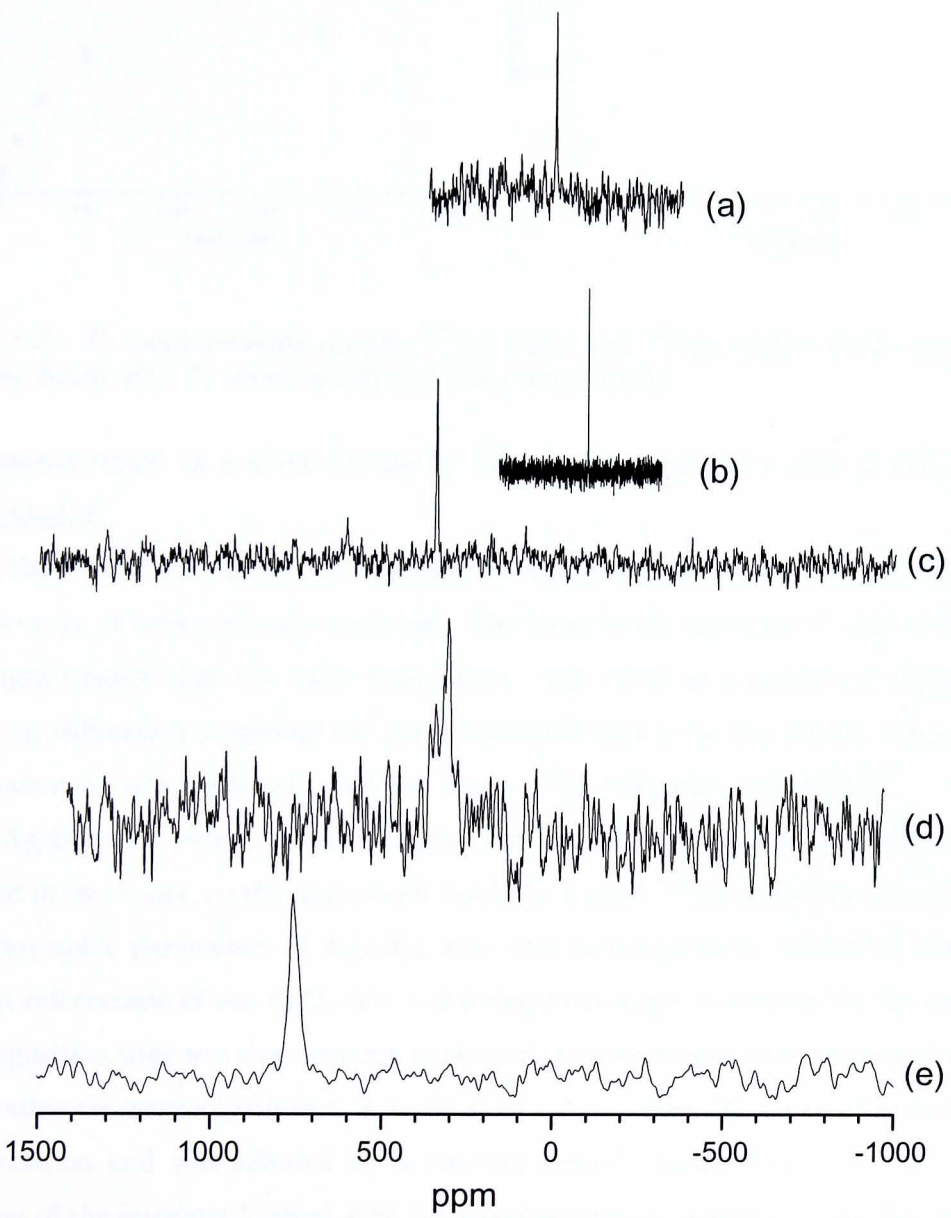

Figure 6.1: ^{109}Ag MAS NMR performed at 8.45 T on a variety of silver containing compounds, spinning at 4.5 kHz. The compounds are: a) $AgNO_3$ aqueous solution (static), b) $AgNO_3$ powder, c) Ag_2CO_3, d) Ag_2SiO_3 and e) AgI.

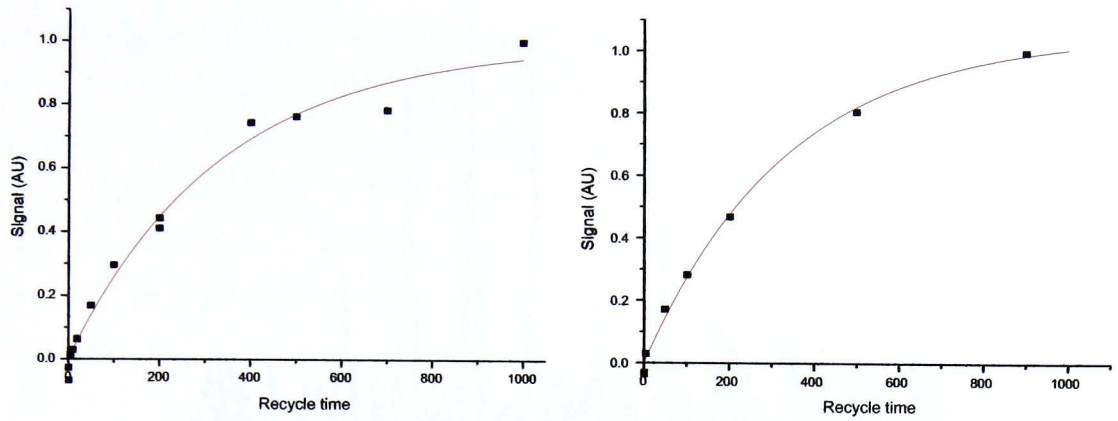

Figure 6.2: T_1 measurements on the ^{107}Ag (left) and ^{109}Ag (right) NMR isotopes in Ag_2CO_3, fitted with T_1 times of 335 and 336 s respectively.

other measurement on a silver silicate by Jansen who measured a shift of 320 ppm for $Ag_{10}Si_4O_{13}$[12].

There have been a number of studies on AgI and the resonance measured here was outside range of values already measured. The most recent value for $\beta-$AgI of 680 ppm is 80 ppm smaller than the value found here. AgI exists as a number of polymorphs, and X-ray diffraction confirmed the phase examined here to be the β-form. This has one inequivalent Ag site, consistent with the single ^{109}Ag resonance observed[13].

Ag_2CO_3 is a very crystalline sample and a reasonable quality spectrum could be acquired in two hours, so this compound would be a good ^{109}Ag secondary reference. The crystallographic parameters of Ag_2CO_3 were first investigated by Masse[14] who found the unit cell consists of one AgO_4 site, and a single resonance is observed in the spectrum. The acquisition time was short enough to allow T_1 measurements to be performed through a saturation recovery experiment. A train of 10×9 μs pulses, 25 ms apart saturated the magnetisation and was followed by a recovery period ranging from 1 to 900 s. The variation of the integrated signal with the recovery time is plotted in figure 6.2, and a T_1 time of 335 s has been determined.

The 7 mm probe was further modified by adding additional capacitance to enable it to tune to the ^{107}Ag isotope. A train of 20×12 μs pulses, 200 μs apart, followed by recovery periods ranging from 1 to 900 s were then used to measure the T_1 time for

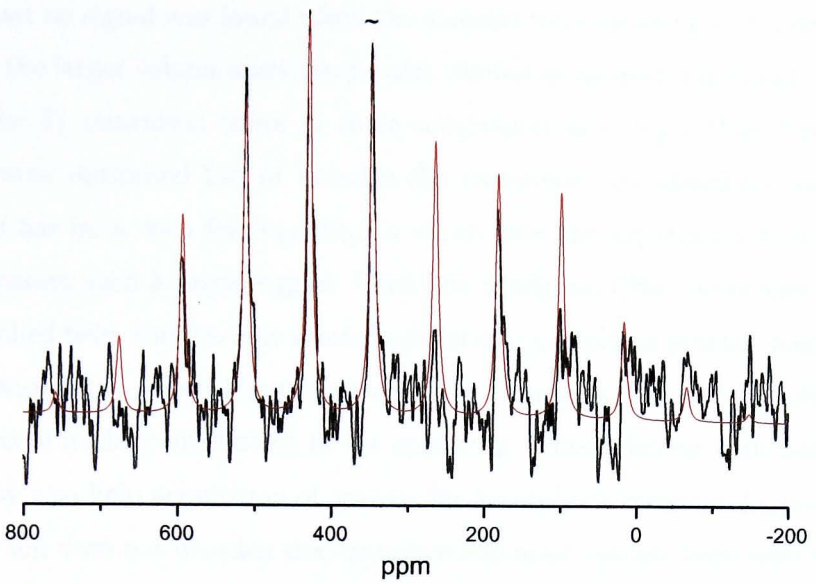

Figure 6.3: Fitting of slow spinning (1 kHz) Ag_2CO_3 using a CSA manifold of spinning sidebands. $\sim$ is the isotropic resonance.

this isotope as well. Figure 6.2 also shows the integrated signal for this isotope and a T_1 time of 336 s is fitted to it. If the dominant relaxation mechanism is through dipolar coupling between ^{109}Ag and ^{109}Ag nuclei, and between ^{107}Ag and ^{107}Ag nuclei, term B in equation 2.16 would describe the relaxation rate. T_1 would then be proportional to r^6/γ^4 since the relaxation rate between a pair of spins is proportional to the square of the interaction Hamiltonian[15]. This means T_1 would be $\times 1.7$ longer for ^{107}Ag than for ^{109}Ag, and since the measured times are almost identical, another relaxation mechanism must be dominant.

The CSA parameters for the site were measured by spinning the sample at 1 kHz, much slower than previous experiments. The manifold of spinning sidebands can be seen in figure 6.3 and were fit using the winfit software from which values of $\Omega = 685 \pm 50$ ppm and $\kappa = -0.08 \pm 0.14$ were calculated. Attempts were made to record the static CSA powder pattern using the modified static probe together with an echo sequence. The poor signal-to-noise and response of the probe at the low frequency meant that no reasonable lineshape could be measured.

^{109}Ag solid state NMR measurements were also attempted on $Ag_2B_4O_7$ and Ag_2WO_4

compounds and no signal was found when the samples were spinning at 5 kHz. Echo experiments on the larger volume static probe also yielded no measurable signal. This could be because the T_1 relaxation times in these compounds are longer than the 300 s the experiments were optimised for, or because the resonances are dispersed over a broad shift range as has been seen for Ag_2SiO_3, in which case the experiment is not sensitive enough to measure such a broad signal. Since the dominant CSA interaction scales linearly with applied field, there is only limited advantage to applying greater magnetic fields to enhance sensitivity. Another approach could be to use an even greater volume rotor so there are more nuclei contributing to the spectrum. Dilute doping with paramagnetic impurities may also help acquisition of spectra for amorphous compounds, providing the paramagnetic ion does not broaden the resonance too much, as has been seen in chapters 4 and 5. The effect of doping yttrium silicon oxynitride compounds with lanthanides has been found to increase relaxation rates of ^{89}Y and ^{29}Si resonances[16].

A silver/gold alloy was also prepared to attempt to observe any change in Knight shift with alloying, however no paramagnetic signal was observed for the alloy. The characteristic skin depth d of a conducting material is a measure of the distance into the conductor that an electric field will be reduced to $1/e$ of its free-space value, and is given by

$$d = \frac{1}{\sqrt{\mu_0 \mu_r \rho \pi f}} \tag{6.1}$$

where ρ is the conductivity of the material, f is the frequency of the radiation and μ_r is the permittivity relative to μ_0, the permittivity of free space. For metallic silver, $d = 15.5$ μm for ^{109}Ag at 8.45 T. Since the alloy particle size was $\sim 200 - 500$ μm, a large proportion of the bulk Ag nuclei were not close enough to the surface skin depth region to be able to contribute any signal.

6.3 Silver glasses

A silver glass was prepared by mixing the oxides SiO_2, Na_2O, B_2O_3 and Al_2O_3 in close to equimolar ratio. Ag_2O was then added at a level of ~ 5 mol%. The mixture was heated to 1500°C for 60 mins, and quenched in water. Three portions were then heated to 400, 800 and 1200°C so that the effect of extra heat treatments on the glass could be investigated.

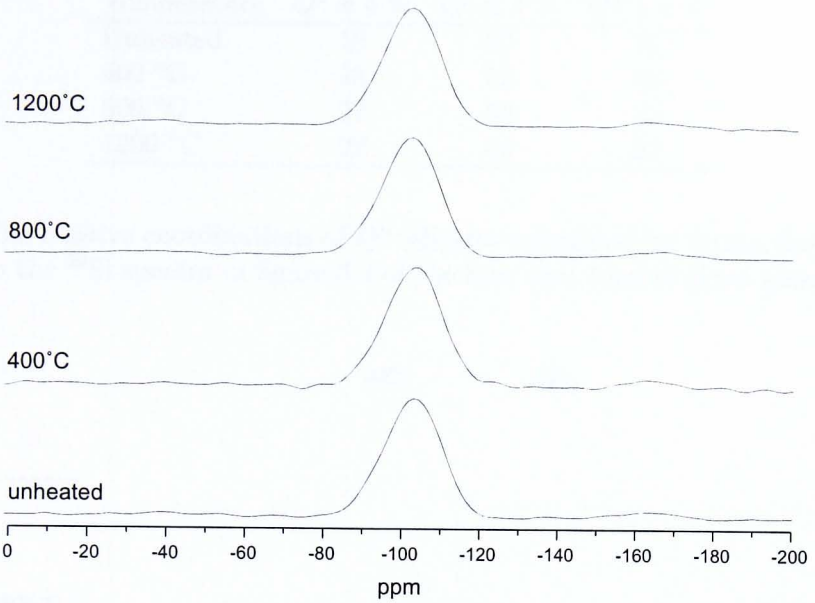

Figure 6.4: ^{29}Si MAS NMR performed at 8.45 T on Ag glass spinning at 4.5 kHz.

After much searching, no ^{109}Ag metal or diamagnetic signal could be measured for any of the four samples. One of the aims of the extended heat treatments was that it would cause precipitation of silver into a metallic phase which could be detected by ^{109}Ag NMR, however it is likely that the low concentrations of Ag present in the initial oxide mixture are too dilute to measure. If a silver metal precipitate formed which was concentrated into relatively large regions, ^{109}Ag signal would be lost due to the finite skin-depth which can be measured. If the metallic silver formed small enough particles, surface dispersion effects could also cause signal loss through line broadening. This is because surface-induced spatial variations in the density of the Fermi-level electrons cause the surface signal to be broader than the bulk signal[17]. ^{109}Ag NMR has been performed on systems of suspended silver particles [9, 18, 19], however, this broadening mechanism meant that the smallest particle size measured was 50 nm.

Instead of pursuing any further ^{109}Ag NMR studies on this system, the effect of the heating on the ^{11}B, ^{23}Na, ^{27}Al and ^{29}Si nuclei was investigated instead. ^{29}Si MAS NMR was performed at a field of 8.45 T. A 7 mm Bruker DB probe was used to spin the silver glasses at 4.5 kHz. A 1 μs pulse was used to induce a $\pi/6$ magnetisation tip, and a

Temperature	$Q^2 \pm 4$ %	$Q^3 \pm 4$ %	$Q^4 \pm 4$ %
Unheated	18	52	30
400 °C	18	52	30
800 °C	22	56	22
1200 °C	22	56	22

Table 6.2: The relative coordinations of Q^n silicates calculated by fitting three Gaussian lineshapes to the ^{29}Si spectra in figure 6.4 of the four heat treated silver glasses.

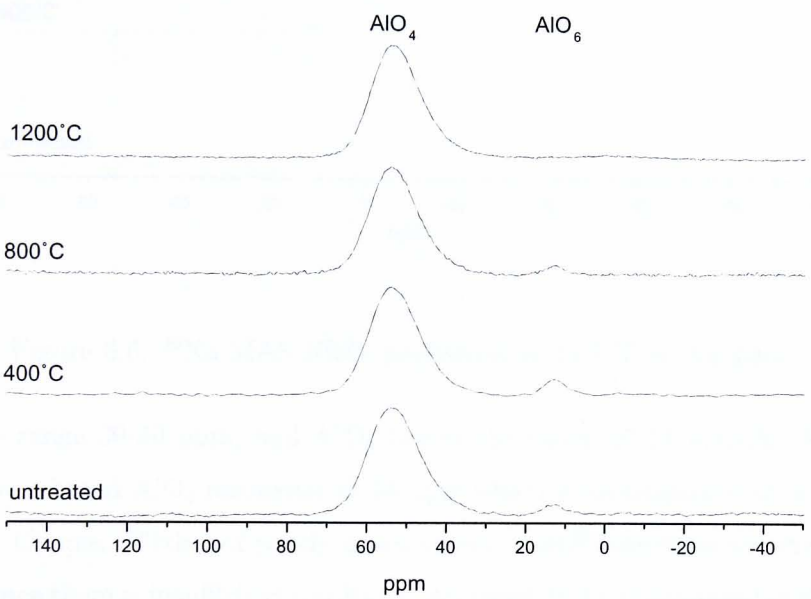

Figure 6.5: ^{27}Al MAS NMR performed at 14.1 T on Ag glass.

recycle delay of 60 s ensured the ^{29}Si signal was not saturated. The spectra acquired are plotted in figure 6.4. Deconvolution of the spectra was performed in the same manner as for the ^{29}Si spectrum of the zircon precursor in figure 4.2. Gaussian lineshapes 11 ppm wide were fitted at $\delta_{iso} = -93, -101$ and -108 ppm to simulate Q^2, Q^3 and Q^4 silicate species. The results of the deconvolutions are listed in table 6.2, and within error limits, all show that Si exists in Q^2, Q^3 and Q^4 coordinations in the ratio 20:54:26. There does not appear to be any change in silicon coordination after extra heat treatments.

Figure 6.5 shows the ^{27}Al spectra of the four samples. ^{27}Al is a commonly used NMR isotope and the shift range a resonance resides in gives an idea of the coordination AlO_x. AlO_4 tends to lie in the range 50-80 ppm, AlO_5 is quite uncommon but can be

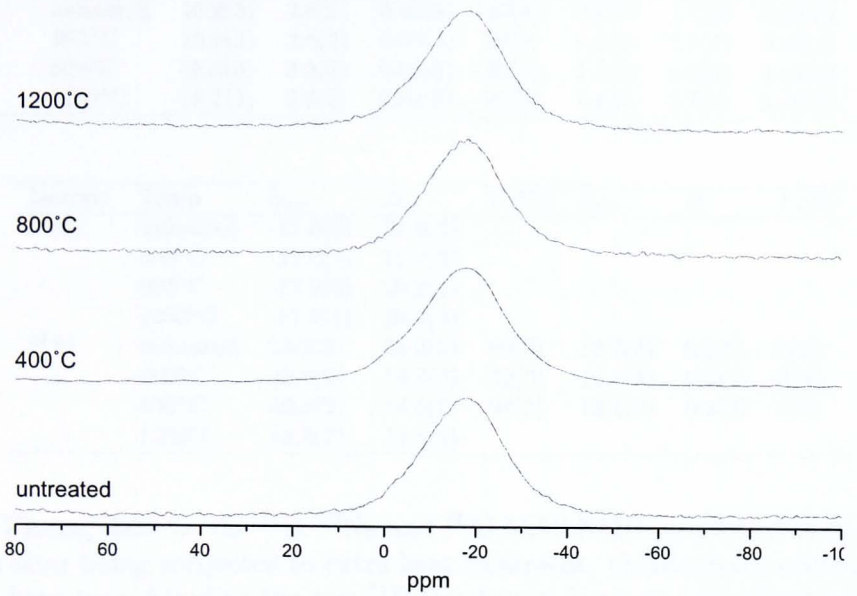

Figure 6.6: ^{23}Na MAS NMR performed at 14.1 T on Ag glass.

found in the range 30-40 ppm, and AlO_6 lies in the range 10-15 ppm[3]. Figure 6.5 is dominated by a broad AlO_4 resonance at 53 ppm which is accompanied by a minor AlO_6 resonance at 13 ppm. Fitting of purely quadrupolar central transition lineshapes was not attempted since there is insufficient resolvable structure in the lineshapes for unambiguous fitting. The linewidths, shifts and integrals of the lineshapes are listed in table 6.3. There is little variation in any of the parameters with extra heat treatment, however the amount of AlO_6 present is reduced with respect to AlO_4.

The ^{23}Na spectra for the various heat treatments are shown in figure 6.6. All spectra are identical and show a broad line at -17 ppm (table 6.3). The position of this line is in the region where disordered sodium species were observed when looking at sodium containing fluxing agents in V-$ZrSiO_4$. Further calcining appears to have no effect on the local Na environment.

^{11}B spectra for the heat treatments are shown in figure 6.7, and in common with the ^{23}Na spectra, the ^{11}B local environment is not influenced by extra sample heating. This is confirmed by the consistency of the quadrupolar parameters which can be used to fit the spectra (table 6.3).

Isotope	Temp	δ_{iso}	C_Q	η_Q	I (%)	δ_{iso}	C_Q	η_Q	I (%)
^{11}B	unheated	16.9(3)	2.6(2)	0.60(5)	32(5)	0.9(3)	1.7(2)	0.43(5)	68(5)
	400°C	15.9(3)	2.6(2)	0.60(5)	28(5)	0.9(3)	1.7(2)	0.43(5)	72(5)
	800°C	15.9(3)	2.5(2)	0.60(5)	30(5)	1.1(3)	1.7(2)	0.40(5)	70(5)
	1200°C	16.2(3)	2.6(2)	0.60(5)	29(5)	1.2(3)	1.7(2)	0.40(5)	71(5)

Isotope	Temp	δ_{iso}	Δ	I (%)	δ_{iso}	Δ	I (%)
^{23}Na	unheated	-17.3(3)	21.0(3)				
	400°C	-17.0(3)	22.2(3)				
	800°C	-17.3(3)	20.2(3)				
	1200°C	-17.2(3)	20.9(3)				
^{27}Al	unheated	53.2(2)	15.0(2)	93(3)	12.7(2)	9.2(2)	7(3)
	400°C	52.8(2)	14.8(2)	92(3)	12.4(2)	9.2(2)	8(3)
	800°C	52.9(2)	14.5(2)	94(3)	13.1(2)	9.2(2)	6(3)
	1200°C	52.8(2)	14.8(2)				

Table 6.3: Fitting data for the ^{11}B, ^{23}Na and ^{27}Al MAS NMR performed at 14.1 T for the silver glass after being subjected to extra heat treatment. Quadrupolar central transition lineshapes have been fitted to the two ^{11}B lineshapes, however only Gaussian lineshapes have been fitted to the remaining isotopes. δ_{iso} and Δ are in units of ppm, and C_Q is in MHz.

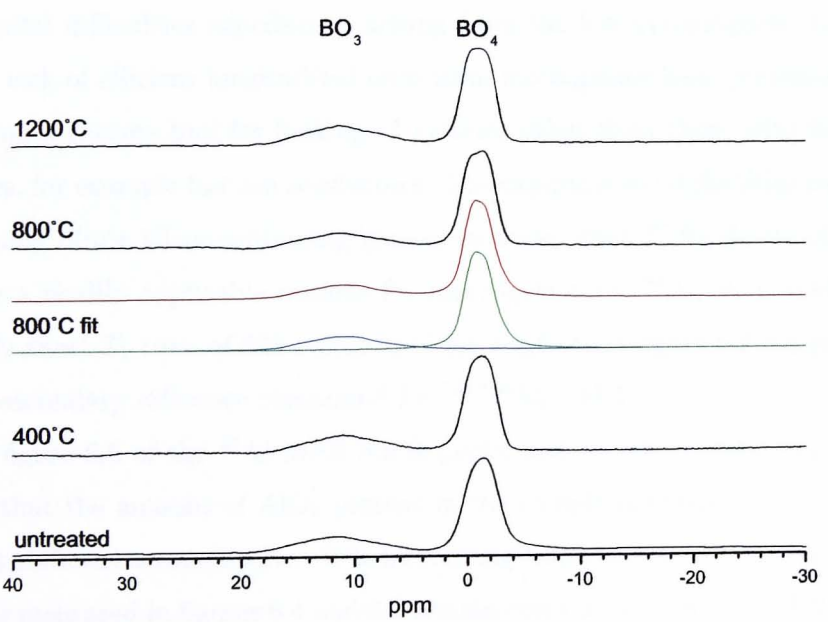

Figure 6.7: ^{11}B MAS NMR performed at 14.1 T on Ag glass. Quadrupolar central transition lineshapes have been simulated for the 800°C heat treatment.

^{11}B spectra reflect the coordination at BO_x sites in a similar manner to ^{27}Al spectra. Tetrahedral BO_4 sites will typically be in the range 2 to -4 ppm. Trigonal BO_3 can be found in the range 19 to 12 ppm, and because of the planar arrangement of oxygen around the ^{11}B nucleus, this site tends to have a much larger C_Q than the BO_4 site[3]. A recent study concentrating on three-coordinated boron found that when studied at a high enough field ($\sim$ 14.1+ T), the shift of the three-coordinated peak was well enough resolved that it was possible to observe an increase in shift when bridging oxygens were replaced by nonbridging oxygens[20]. However, no net shift is observed in the BO_3 peak here. The data obtained here also shows that the ratio of BO_4/BO_3 does not change with extra heat treatment.

6.4 Conclusions

The chemical shifts measured for the silver reference compounds in figure 6.1 range from 760 ppm for AgI to -97 ppm for $AgNO_3$ powder. This large chemical shift range indicates that ^{109}Ag is potentially a very sensitive probe of local environment. However, the experimental difficulties experienced arising from the low gyromagnetic ratio of the nucleus, and lack of efficient longitudinal relaxation mechanisms have prevented this nucleus becoming a routine tool for looking at systems other than those with intrinsically short T_1 times, for example fast ion conductors. The experimental difficulties encountered when examining dilute silver-containing glasses indicates that ^{109}Ag does not currently appear to be a readily applicable nucleus for investigation of ^{109}Ag local environments. The relatively short T_1 time of 335 s measured for Ag_2CO_3 in figure 6.2 suggests that it is a suitable secondary reference compound for ^{107,109}Ag NMR.

From figure 6.5 of the ^{27}Al MAS NMR performed on silver-containing glasses, it can be seen that the amount of AlO_6 present in the sample decreases when the sample is calcined at different temperatures. It is interesting that the relative silicon and boron coordinations measured in figures 6.4 and 6.7 remain constant throughout additional heat treatment. These species appear to have found their equilibrium ratios during sample firing, unlike the AlO_4 and AlO_6 coordinations, which depend on extra sample firing time.

References

[1] J. Booth, Johnson Matthey, Private Communication (2002).

[2] M. E. Smith, Recent Progress in Solid-State NMR of Low-γ Nuclei, *Annual Reports on NMR Spectroscopy*, **43** 121 (2001).

[3] K. J. D. MacKenzie and M. E. Smith, *Multinuclear Solid-state NMR of Inorganic Materials*, Pergamon (Amsterdam), 2002.

[4] H. Looser and D. Brinkmann, ^{109}Ag Chemical Shifts in Some Solid Compounds, *Journal of Magnetic Resonance*, **64** 76 (1985).

[5] M. Tansho, H. Wada, M. Ishii and Y. Onada, Mobility of Silver Ions in Silver Ion Conductor Ag_7NbS_6 Studied by Ag and Nb NMR, *Journal of Physical Chemistry B*, **102** 5047 (1998).

[6] M. Tansho, H. Wada, M. Ishii and Y. Onada, Silver ionic conductor Ag_9GaSe_6 studied by Ag and Ga NMR, *Solid State Ionics*, **86-88** 155 (1996).

[7] S. H. Chung, K. R. Jeffrey, J. R. Stevens and L. Borjesson, Dynamics of silver ions in $(AgI)_x$-$(Ag_2O$-$Nb_2O_3)_{1-x}$ glasses - A Ag-109 nuclear-magnetic-resonance study, *Physical Review B*, **41** 6154 (1990).

[8] P. Mustarelli, C. Tomasi, E. Quartarone, A. Magistris, M. Cutroni and A. Mandanici, Structural and cation dynamics in the system AgI:Ag_2MoO_4: A ^{109}Ag study, *Physical Review B*, **58** 9054 (1998).

[9] J. K. Plishke, A. J. Benesi and M. A. Vannice, Solid-State ^{109}Ag NMR Characterization of Silver Dispersed on Oxide Supports, *Journal of Physical Chemistry*, **96** 3799 (1992).

[10] K. D. Becker and E. Von Goldammer, NMR chemical shifts in the silver halides, *Chemical Physics*, **48** 193 (1990).

[11] M. Jansen, K. Heidebrecht, R. Matthes and W. Eysel, On silver(I)-catena-polysilicate, crystal-growth, and structure determination, *Zeitschrift fuer Anorganische und Allgemeine Chemie*, **601** 5 (1991).

[12] M. Jansen, Homoatomic d^{10}-d^{10} interactions: Their effects on structure and chemical and physical properties., *Angew. Chem. International Edition*, **26** 1098 (1987).

[13] H. J. Berethold and P. M. Kasse, Anharmonische Verfeinerung der thermischen parameter des beta - AgI bei 294K und 400K, *Zeitschrift fuer Kristallographie*, **186** 38 (1989).

[14] P. R. Masse, J. C. Guitel and A. Durif, Structure du Carbonate d'Argent, *Acta Crystallographica B*, **35** 1428 (1979).

[15] I. Solomon, Relaxation processes in a system of two spins, *Physical Review*, **99** 559 (1955).

[16] R. H. Meinhold and K. J. D. MacKenzie, Effect of lanthanides on the relaxation rates of ^{89}Y and ^{29}Si in yttrium silicon oxynitride phases, *Solid State Nuclear Magnetic Resonance*, **5** 151 (1995).

[17] J. Bardeen, Theory of the work function. II. The surface double layer, *Physical Review*, **49** 653 (1936).

[18] V. M. Mastikhin, I. L. Mudrakovsky, S. N. Goncharova, B. S. Balzhinimaev, S. P. Noskova and V. I. Zaikovsky, Observation of Ag-109 NMR-spectra of supported silver catalysts, *React. Kinet. Catal. Lett*, **48** 425 (1992).

[19] J. J. Bercier, M. Jirousek, M. Graetzel and J. J. van der Klink, Evidence from NMR for temperature-dependent Bardeen-Friedel oscillations in nanometer-sized silver particles, *Journal of Physics Condensed Matter*, **5** 75 (1993).

[20] S. Kroeker and J. F. Stebbins, Three-coordinated Boron-11 Chemical Shifts in Borates, *Inorganic Chemistry*, **40** 6239 (2001).

Chapter 7

Tin-Zinc-Titanium pigments

7.1 Introduction

7.1.1 Tin-zinc-titanium pigments

Tin-zinc-titanium (TZT) pigments were invented by Jenkins and Wolstenholme in 1983, and the only literature published on these are the original patent applications[1, 2]. TZT pigments are created by mixing TiO_2 and ZnO with either SnO, or SnO_2 and a reducing agent. It is important that these pigments are fired in an atmosphere that is neither reducing or oxidising for a colourful pigment to be created. The technique usually employed is to heat the reactants in a closed crucible to at least 850°C for 20 minutes. The resulting colour of the pigment depends on the ratio of the three oxides used, and figure 7.1 shows the perceived colour of the pigment created by mixing different mol% of the three oxides. The desirable orange/yellow colour is created by mixing a 1:1:2 mixture of ZnO, SnO and TiO_2, however TZT pigments have a large colour-space, and a wide variety of different shades of colour can be synthesised.

Although patented in 1983, TZT pigments have only been brought into mass production relatively recently. This is because alternative, well established yellow coloured cadmium- or antimony-containing pigments are more economical to produce. However, the toxicity of cadmium-containing pigments is increasingly a concern[3-5], and TZT pigments are an environmentally friendlier, non toxic alternative yellow pigment. TZT pigments can be used to colour plastics, and are typically blended into PVC at $\sim$ 180°C.

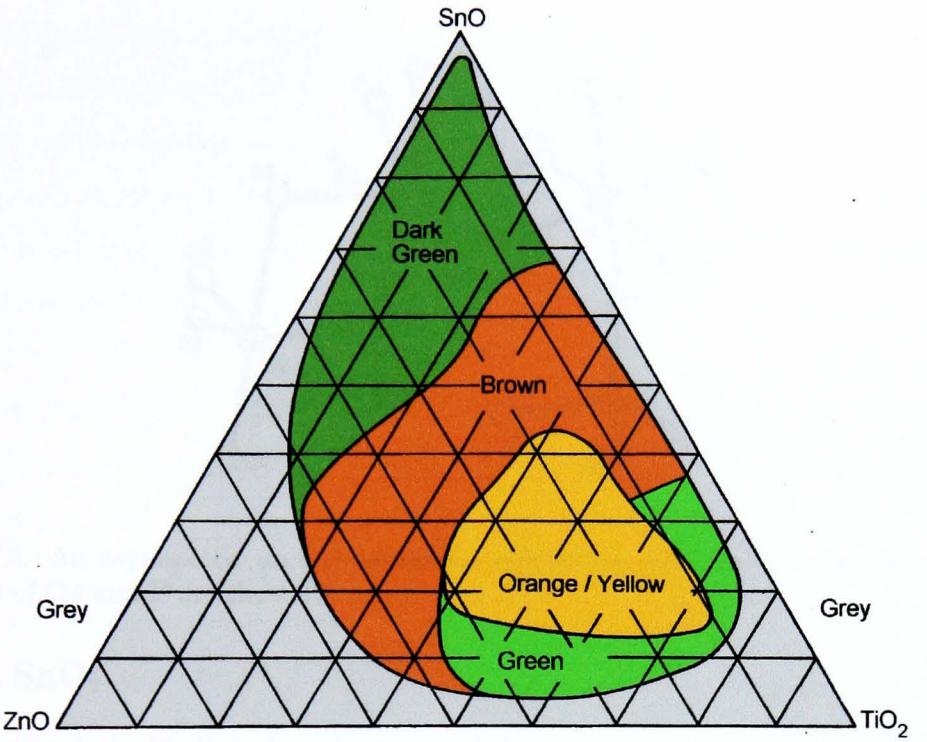

Figure 7.1: A ternary diagram correlating the composition of a pigment system (in divisions of 10 mol%) with the perceived colour of the complex[2].

TZT can also be used to colour paints where it can replace yellow nickel antimony titanate, and orange coloured bismuth vanadate pigments.

X-ray diffraction phase analysis on fired TZT pigments reveals that only one pigment phase is present. This structure has been identified as the crystal structure of murataite, a Y/Ti oxide mineral first discovered by Adams[6]. The crystal structure of this mineral was later resolved as having space group $F\bar{4}3m, a = 14.886$ Å, and consists of four cation sites, labelled M1, M2, X and T which are 6-, 5-, 8- and 4-coordinated respectively[7]. There have been no diffraction studies performed on the TZT form of murataite, so no site assignments are known for the Ti, Sn and Zn ions. A representative unit cell is shown in figure 7.2, where the F site would actually contain an oxygen atom since there is no fluorine source present during the TZT-forming reaction.

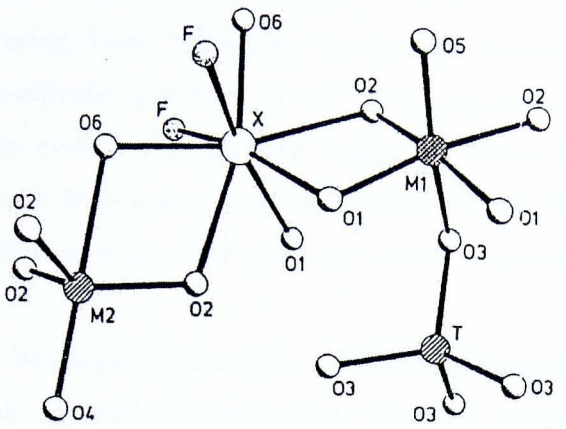

Figure 7.2: An asymmetric unit of Murataite polyhedra. For clarity, only the average positions of O4 and F are shown[7].

7.1.2 SnO_2

SnO_2 has many technological applications. It is used as a catalyst for oxidising CO to CO_2 with a very low minimum operating temperature of $< 150°C$[8]. It also finds applications in solid state gas sensors[9]. Thin SnO_2 films have optoelectronic applications in electrochromic displays and solar cells, since the films are transparent conductors which exhibit high chemical and mechanical stability even at high temperatures[10], especially when doped with fluorine[11].

SnO_2 exists at room temperature as casserite which has a rutile structure[12]. This has led to its use in reducing the anatase to rutile phase transition temperature of another technologically important material, TiO_2[13]. By synthesising $Sn_{1-x}Ti_xO_2$ compounds, the rutile structure of the SnO_2 component of the composite forces the TiO_2 crystal structure from the room temperature anatase form into rutile[14, 15].

The sol-gel technique for synthesising tin oxide ceramics is widely used[16]. It is particularly useful for manufacturing catalytic samples since when the solvent is extracted efficiently after gelling has occurred, a high surface area powder is left. It is also a novel technique for producing undoped[17] and doped[18] thin films for optoelectronic applications, since high quality films can be produced cost effectively through dip- or spin-coating.

The microstructure of SnO_2 has long been known to depend on its thermal history

[19-21]. In a recent study, the properties of a SnO_2 xerogel were examined after heating to various temperatures using X-ray diffraction, transmission electron microscopy (TEM), ultraviolet-visible-near-infrared spectroscopy and Raman spectroscopy[22]. It was found that the microstructure evolved through three stages. At below 300°C, extensive dehydroxylation occurred with little grain growth being observed by TEM. Between 300 and 500°C, extensive crystallisation occurred whilst above 700°C only extra grain growth was observed.

SnO_2 has been the subject of a number of ^{119}Sn NMR studies[15, 23-25]. Clayden found that the spinning sideband manifold of the ^{119}Sn MAS spectrum of SnO_2 could be fit using $\delta_{iso} = -604.3$ ppm, $\Omega = 125$ ppm and $\kappa = 1.0$[23]. The value of Ω measured was quite large even though the Sn atom sits at an octahedral site with six oxygens equidistant from the Sn. The slight distribution in O-Sn-O bond angles was thought to be responsible for Ω. Cossement subsequently refined these values to $\delta_{iso} = -603 \pm 2$ ppm, $\Omega = 136$ ppm and $\kappa = 0.66$[25]. Values of $\delta_{iso} = -208 \pm 2$ ppm, $\Omega = 1013$ ppm and $\kappa = 0.87$ were measured for SnO. In SnO, every Sn atom is located at the top of a square pyramid, with the four oxygens located in the [001] plane. The tenfold increase in Ω was attributed to the electronic density at the Sn nucleus being shifted towards other tin neighbours, and away from the planar arrangement of neighbouring oxygen atoms. This also caused J-coupling of 8286 ± 100 Hz between ^{119}Sn and ^{117}Sn nuclei, which was strong enough that it could be observed in MAS spectra of SnO.

7.2 TZT pigments

A number of different sets of pigments were produced. The effect of firing temperature was investigated for undoped TZT pigments, and pigments doped with Na_2CO_3. A set of variable Na_2CO_3-content pigments was also produced which was only fired at one temperature.

7.2.1 Undoped TZT

^{119}Sn NMR was initially performed on the undoped TZTs at a field of 5.6 T using a 4 mm Doty MAS probe spinning at 17 kHz. However, the volume of the 4 mm rotor allowed

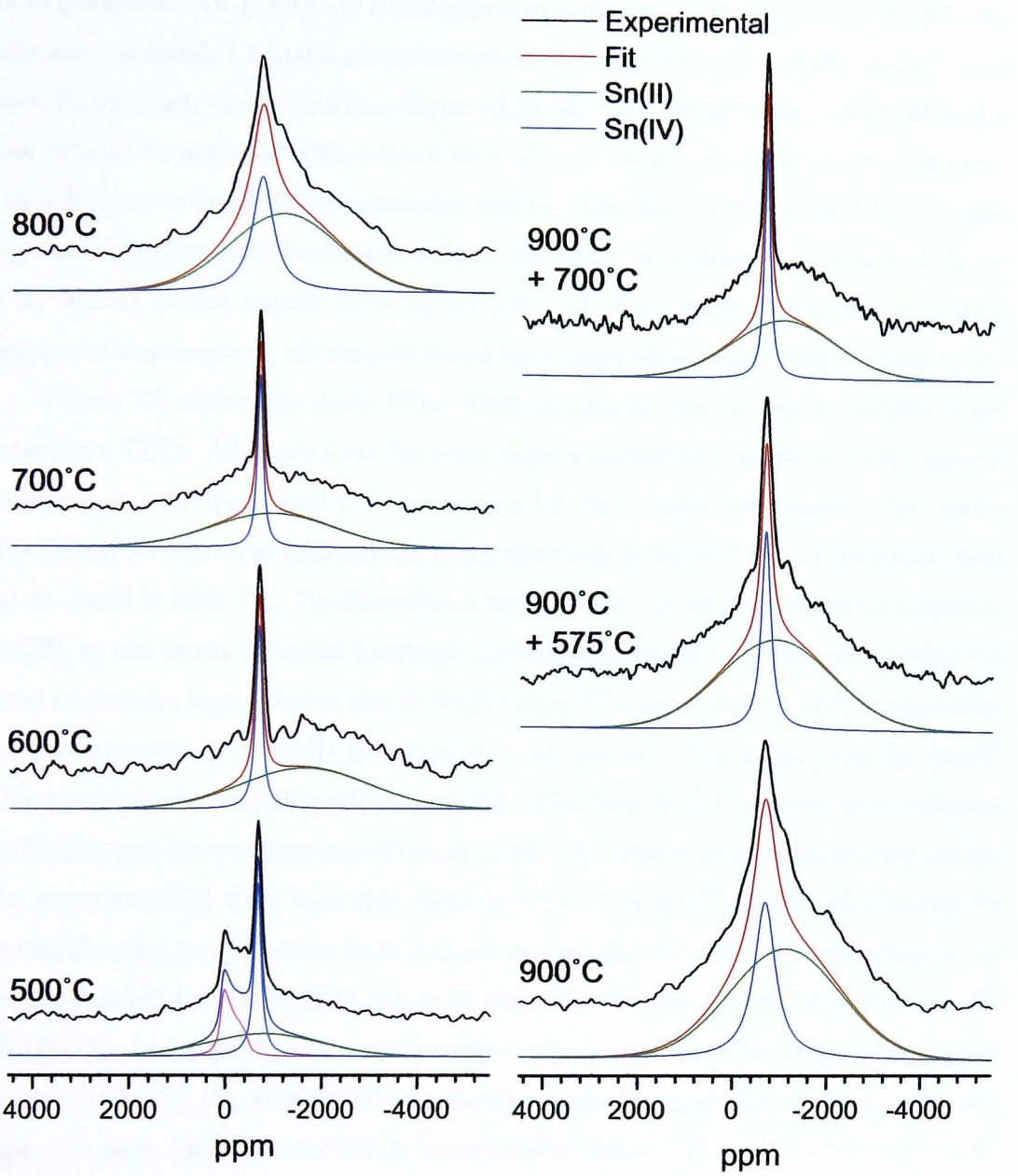

Figure 7.3: ^{119}Sn static NMR performed at 5.6 T on undoped-TZTs which have been fired for 18 mins at increasing temperatures to 900°C. Additional heat treatments have also been performed on the 900°C sample, where one portion was heated in an oxidising air environment at 575°C for a further 18 mins. A second portion was heated in air at 700°C for 18 mins.

only limited signal to be acquired, and the spinning speed was insufficient to provide any gain in resolution. An alternative static approach utilising a large sample volume 9.5 mm probe was employed. 1.5 and 3 μs pulses corresponding to tip angles of 30° and 60° were spaced 50 μs apart, and acquisition begun 20 μs after the second pulse, which allowed a whole echo to be acquired with a dwell time of 1 μs. A recycle delay of 10 s appeared to be sufficient to avoid signal saturation effects. The stated error of ± 15 % in signal integration measurements performed reflects the slight uncertainty in the actual T_1 for the Sn species (which appear to be of the order of 10 s), since performing saturation recovery measurements on all samples would have required excessive spectrometer time.

Figure 7.3 shows the static ^{119}Sn NMR spectra for the undoped, variable firing temperature TZTs. All spectra can be fitted using a Lorentzian lineshape for the narrow component at -600 ppm, and a Gaussian line for the broader component. The results of the fitting are shown graphically for every spectrum in figure 7.3, and the parameters used are listed in table 7.1. The linewidth is known to be a good indicator of Sn oxidation state[26], so the broad Gaussian lineshape has been attributed to Sn(II) sites, whilst the narrow Lorentzian component is due to Sn(IV) sites. This is because in oxide compounds, the local environment of Sn(II) nuclei tends to be much less symmetric than for Sn(IV) nuclei, giving rise to a significantly larger CSA interaction. Sn(II) has two more electrons than Sn(IV), and the wavefunction of this 5s orbital will tend to cause neighbouring cations to be accommodated away from this electron density. In Sn(II)O oxide, this causes the four neighbouring oxygen atoms to be located on one side of the Sn nucleus leading to the CSA linewidth Ω for the Sn(II)O site to be ten times that for the six-coordinate Sn site in Sn(IV)O_2. In Sn(IV)O_2, the neighbouring oxygens are free to be located equidistant from each other at the vertices of an octahedra centered upon the Sn atom. For this reason, the most likely site for Sn(II) in murataite (figure 7.2) is the 5-coordinated M2 site, since the neighbouring oxygens are arranged such that the 5s orbital can be located on the other side of the M2 site from the neighbouring oxygens.

The 500°C spectrum has an additional signal in the 200 to -500 ppm region which is not present for any samples heated to higher temperatures. This can be simulated using a static CSA lineshape with parameters $\delta_{iso} = -103 \pm 40$ ppm, $\Omega = 351 \pm 40$ ppm and $\kappa = 1.0 \pm 0.1$. However, this signal could also be formed as a composite lineshape made

Sample	Lorentzian Sn(IV)			Gaussian Sn(II)		
	δ_{iso} (ppm) ±15	Δ (ppm) ±60	% Sn ±15	δ_{iso} (ppm) ±200	Δ (ppm) ±400	% Sn ±15
500°C	−654	168	32	−805	2760	46
600°C	−649	162	25	−1612	3114	75
700°C	−648	143	27	−908	2951	73
800°C	−681	523	30	−1130	2683	70
900°C	−678	540	29	−1116	2763	71
Extra 575°C	−676	238	21	−896	2825	79
Extra 700°C	−671	153	26	−1024	2575	74

Table 7.1: Results of fitting a Lorentzian lineshape to the Sn(IV) resonance and a Gaussian lineshape to the Sn(II) resonance in the ^{119}Sn static spectra of the variable firing temperature pigments in figure 7.3.

up of Gaussian and Lorentzian lines from separate Sn species.

The ratio of Sn(II) to Sn(IV) in table 7.1 stays reasonably constant at about 3:1 after the various heat treatments. The linewidth of the Sn(IV) peak broadens from 143 ppm at 700°C to 523 ppm at 800°C, so some change in the environment that Sn(IV) resides in has occurred between 700°C and 800°C. The line also appears to shift slightly to more negative ppm after this chemical change. X-ray diffraction measurements on the 800°C sample indicates that significant murataite formation has occurred, with the 900°C sample showing only a single murataite phase. Since the ^{119}Sn line positions and widths measured for these two temperatures are very similar compared to the previous three temperatures, it can be assumed that the only Sn species observed in the 800°C and 900°C spectra are in the final murataite phase. This means that Sn exists in the murataite phase in both Sn(II) and Sn(IV) oxidation states. The linewidth of the Sn(IV) peak is larger for murataite than for the lower temperature TZTs where the main Sn-containing phase measured by X-ray diffraction was Sn(IV)O_2. The linewidth could be due to Sn(IV) being located at more than one of the four possible sites in murataite, with the total Sn(IV) linewidth being the sum of these component lineshapes. The linewidth could also be due to a large CSA interaction arising from the asymmetric arrangement of neighbouring oxygens at a single Sn(IV) site.

The Sn(II) Gaussian peak position fluctuates much more than the Sn(IV), indicating that it could be composed of two or more component Sn(II) lineshapes. However,

extra crystallographic information would be needed as a basis on which to deconvolve this lineshape into component peaks.

A region of the ^{119}Sn spectrum outside the normal spectral window employed, at 6800 ppm was also investigated since this is where metallic Sn is expected[27]. A Doty 4 mm MAS probe was used, and a single pulse of 1 μs tipped the magnetisation 30°. A short recycle delay of 0.1 s was sufficient since the interaction of the conduction electrons with the probe nucleus provides a very efficient relaxation mechanism.

Figure 7.4 shows the ^{119}Sn NMR spectrum of the 700°C sample which has been spun at four different spinning speeds. When performing MAS experiments on a sample at varying speeds, all spinning sidebands will move further away from the isotropic resonance when the speed is increased. This isotropic resonance should stay at a constant shift, and so the isotropic resonance for a sample composed of many spinning sidebands can be identified by spinning at more than one speed. In figure 7.4, there is no single line whose shift is independent of spinning speed, however by spinning the sample sufficiently fast at 15 kHz it is clear that the line at 6769 ± 20 ppm is the isotropic one. This shifts 25 ± 3 ppm to more negative ppm when the sample is spun at 8 kHz. At higher spinning speeds, the sample temperature is likely to be higher due to frictional heating effects between the bearing gas and the rotor. The shift interaction can have a temperature dependant contribution which could be responsible for this shift, and this effect has been used previously specifically to measure sample temperature as a function of spinning speed in ^{119}Sn NMR[28]. Also displayed in figure 7.4 are simulated shift anisotropy dominated spinning sideband manifolds for two of the spinning speeds. Both use parameters of $\Omega = 432 \pm 5$ ppm and $\kappa = -1.0 \pm 0.1$, which are reasonably consistent with values previously found for metallic Sn of $\delta_{iso} = 6707$ ppm, $\Omega = 494$ ppm and $\kappa = -1.0$[27].

Metallic ^{119}Sn measurements were also performed on the other firing temperature samples, and are shown in figure 7.4. All samples were weighed after acquisition, so providing the metallic Sn exists as small enough particles that skin-depth effects do not cause signal loss, quantitative comparison of the spectra can be performed. Metallic Sn appears to have begun to precipitate out of the sample when heating to 500°C, and reaches a maximum at 700°C. After this temperature, no metallic Sn signal can be measured at all. It is this 700°C to 800°C transition that caused the Sn(IV) line in the diamagnetic

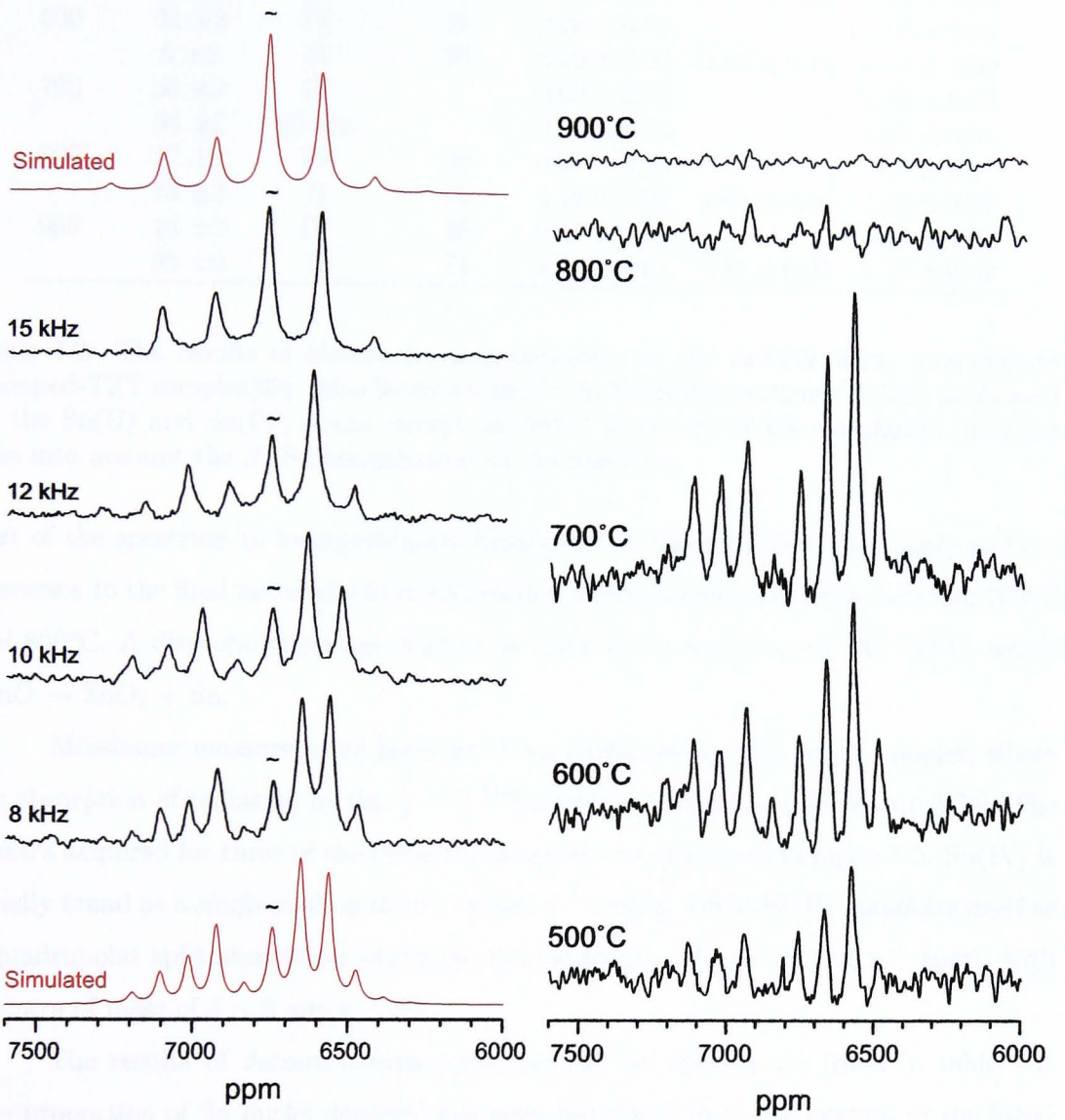

Figure 7.4: ^{119}Sn MAS NMR at 5.6 T of the metallic tin area of the 700°C sample spinning at several different speeds (left), and a shift anisotropy dominated manifold of spinning sidebands has been simulated for the slowest and fastest spinning speeds (parameters used are in the text). Also plotted are the spectra for the other firing temperature TZTs (right) which were acquired at 8.45 T, spinning at 12 kHz.

T (°C)	% Sn	Oxidation	% NMR	δ	ΔE_Q	Γ
500	49 ±2	IV	32	0.04 ± 0.01		1.39 ± 0.02
	51 ±2	II	46	2.72 ± 0.01	1.45 ± 0.02	1.32 ± 0.03
600	94 ±2	IV	25	0.06 ± 0.01		1.59 ± 0.01
	6 ±2	II	75	3.10 ± 0.08	0.93 ± 0.11	1.04 ± 0.09
700	36 ±2	IV		0.03 ± 0.01		1.56 ± 0.05
	64 ±2	(β-Sn)		2.68 ± 0.02		1.41 ± 0.01
800	27 ±2	IV	30	0.07 ± 0.01		1.2 ± 0.1
	73 ±2	II	70	3.12 ± 0.01	1.66 ± 0.04	1.43 ± 0.02
900	18 ±2	IV	29	0.13 ± 0.01		1.11 ± 0.01
	82 ±2	II	71	3.06 ± 0.01	1.67 ± 0.01	1.17 ± 0.02

Table 7.2: The results of Mössbauer measurements on the variable firing temperature undoped-TZT samples[29]. Also listed are the ^{119}Sn NMR integrations (±15%) performed on the Sn(II) and Sn(IV) peaks, except at 700°C where the NMR calculation does not take into account the $\beta-$Sn contribution to the spectrum.

part of the spectrum to be significantly broadened, so metallic Sn is then likely to be a precursor to the final murataite forming reaction which occurs somewhere between 700°C and 800°C. A disproportionation reaction is likely to be occurring at 500-700°C, where $2SnO \rightarrow SnO_2 + Sn$.

Mössbauer measurements have also been performed on this set of samples, where the absorption of radiation by the $\frac{1}{2} \rightarrow \frac{3}{2}$ ^{119}Sn nuclear transition was measured[29]. The spectra acquired for three of the firing temperatures are displayed in figure 7.5. Sn(IV) is usually found as a single peak in the $\delta \sim 0$ mm s^{-1} region, whilst Sn(II) manifests itself as a quadrupolar split absorption where the two peaks are $\Delta E_Q \sim 1.2$ mm s^{-1} apart, with a centre of mass of $\delta \sim 3$ mm s^{-1}[29].

The results of deconvolutions performed on the spectra are listed in table 7.2. The proportion of Sn nuclei detected has been calculated from the integral of the fitted lineshapes by dividing it by the appropriate Lamb-Mössbauer factor f. Values used were $f(SnO) = 0.35$[30], $f(SnO_2) = 0.52$[31, 32] and $f(\beta\text{-Sn}) = 0.04$[33].

In all ^{119}Sn NMR experiments performed on the samples, the ratio of Sn(II):Sn(IV) was 1:3, however the Mössbauer results only complement these findings at 800°C and 900°C. Although there is a discrepancy between the two techniques at lower sample temperatures, the agreement at high temperature confirms that in the murataite phase, Sn is very likely to exist as Sn(II) and Sn(IV) in the ratio 1:3.

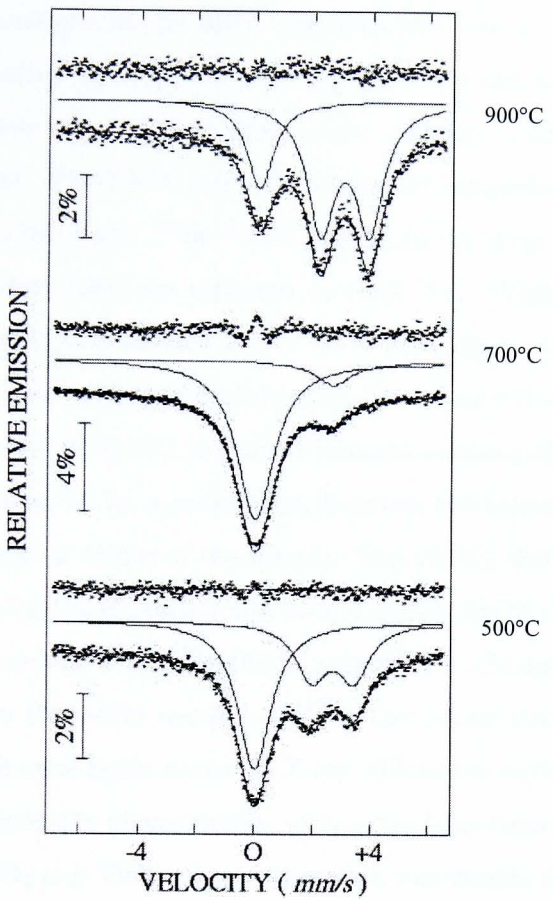

Figure 7.5: ^{119}Sn Mössbauer spectra for three of the undoped TZT heat treatments[29].

Metallic tin was only detected by Mössbauer spectroscopy in the 700°C sample where it was found to be present in the largest quantity by ^{119}Sn NMR. ^{119}Sn NMR is clearly the more sensitive technique here for quantifying metallic Sn species. This is partly because the Knight shift interaction moves the signal away from the diamagnetic region of the spectrum, so that deconvolution is not usually required to resolve the signal, whereas it is required in the ^{119}Sn Mössbauer spectra. It is also because any Mössbauer β-Sn signal is attenuated by a factor $f = 0.04$, so has to be present in quite high concentrations before any Mössbauer absorption can be detected. Conversely, since the T_1 relaxation times of resonances shifted by the Knight shift interaction are typically very quick, acquisition of an NMR signal can be quicker than for purely diamagnetic resonances.

Since firing in an oxidising atmosphere has been found to comprimise colour for-

mation, the effect of subjecting the 900°C sample to extra heating in an air atmosphere was investigated. One sample of the 900°C pigment was heated in air at 575°C for an extra 18 mins, and another portion was fired at 700°C for the same time. The 575°C sample was a deep yellow colour before firing in air, and was a faint yellow colour after the extra heat treatment. The 700°C portion was almost completely white.

Figure 7.4 shows the static ^{119}Sn NMR performed on these two oxidised samples, and the fitting parameters used are reported in table 7.1. Whilst the position of the Sn(IV) line stays reasonably unchanged in the −670 ppm region, its linewidth Δ reverts from 540 ppm to 238 ppm after extra heating at 575°C, and finally to 153 ppm after heating at 700°C. The ratio of Sn(II) to Sn(IV) remains unchanged with extra oxidation, however there does appear to be a correlation between the linewidth Δ of the Sn(IV) resonance, and the perceived colour of the sample. The 500°C, 600°C and 700°C samples all appear as a dull grey coloured powder and have a narrow Sn(IV) linewidth. The 800°C sample is a dull orange colour whilst the 900°C sample is a vibrant orange pigment, and the linewidths exhibit a three-fold increase. When the colour starts to fade after extra oxidation, the linewidth once again narrows. X-ray diffraction experiments indicate that whilst there is still a murataite phase present after extra heat treatment, some murataite has degraded into $ZnTiO_4$ and TiO_2. X-ray diffraction was unable to detect any other Sn-containing phases, even though the ratio of Sn(IV) to Sn(II) as measured by ^{119}Sn NMR remains the same. The Sn leftover from the murataite degradation could have formed a non-crystalline phase undetectable by routine X-ray diffraction, or it could also have remained in the murataite phase taking the place of the liberated Zn and Ti. The reason for the loss of colour could then be due to either dilution of the murataite pigment in the newly created phases, or the extra Sn in the TZT phase could have upset the required Sn:Zn:Ti ratio needed for an orange coloured pigment (figure 7.1). The narrowing of the Sn(IV) lineshape means that it is more likely to be due to Sn(IV) in an extra phase, since if further sites were occupied in murataite, the lineshape would be expected to broaden.

Firing temp/ mol% Na_2CO_3	Lorentzian Sn(IV) δ_{iso} (ppm) ±15	Δ (ppm) ±60	Ratio ±15	Gaussian Sn(II) δ_{iso} (ppm) ±200	Δ (ppm) ±400	Ratio ±15
550°C	−650	159	31	−1150	3314	69
650°C	−651	133	32	−1114	3111	68
750°C	−648	226	27	−806	2693	73
850°C	−653	497	28	−1107	2763	72
1 mol%	−671	550	24	−1014	3286	76
2 mol%	−680	533	23	−869	3236	77
5 mol%	−660	517	35	−291	3131	65
10 mol%	−628	416	23	−408	3147	77
20 mol%	−598	274	15	−802	2985	85

Table 7.3: Results of fitting a Lorentzian lineshape to the Sn(IV) resonance and a Gaussian lineshape to the Sn(II) resonance in the ^{119}Sn static spectra of the variable firing temperature 5 mol% Na_2CO_3-doped pigments, and the variable Na_2CO_3-doped pigments heated to 850°C in figure 7.6.

7.2.2 Na_2CO_3 doped TZTs

^{119}Sn NMR

Static ^{119}Sn spectra performed on the variable firing temperature Na_2CO_3-doped TZTs and variable Na_2CO_3-content TZTs were acquired at 5.6 T in the same manner as for the undoped TZT pigments. Figure 7.6 shows the ^{119}Sn static NMR performed on TZT pigments produced using 5 mol% Na_2CO_3, which had been fired at four different temperatures. As before, a Gaussian lineshape has been fitted to quantify the amount of Sn(II) present, and a Lorentzian is fitted to quantify Sn(IV). The parameters used to fit the spectra are listed in table 7.3.

The width of the Sn(IV) lineshape broadens significantly when heated to 750°C from 130 ppm to 226 ppm, and is almost 500 ppm wide by 850°C. This is similar to the effect observed for the undoped TZTs, where the linewidth increased from 143 ppm at 700°C to 523 ppm at 800°C. The 750°C linewidth seen here is somewhere between these two extremes, so the transition from narrow to broad does not appear to be rapid, and so the murataite-forming reaction must also be reasonably slow. Once again, the width of the Sn(IV) resonance reflects the colour of the pigment since the 750°C sample is a faint yellow colour whilst the 850°C sample is a much fuller yellow since murataite formation

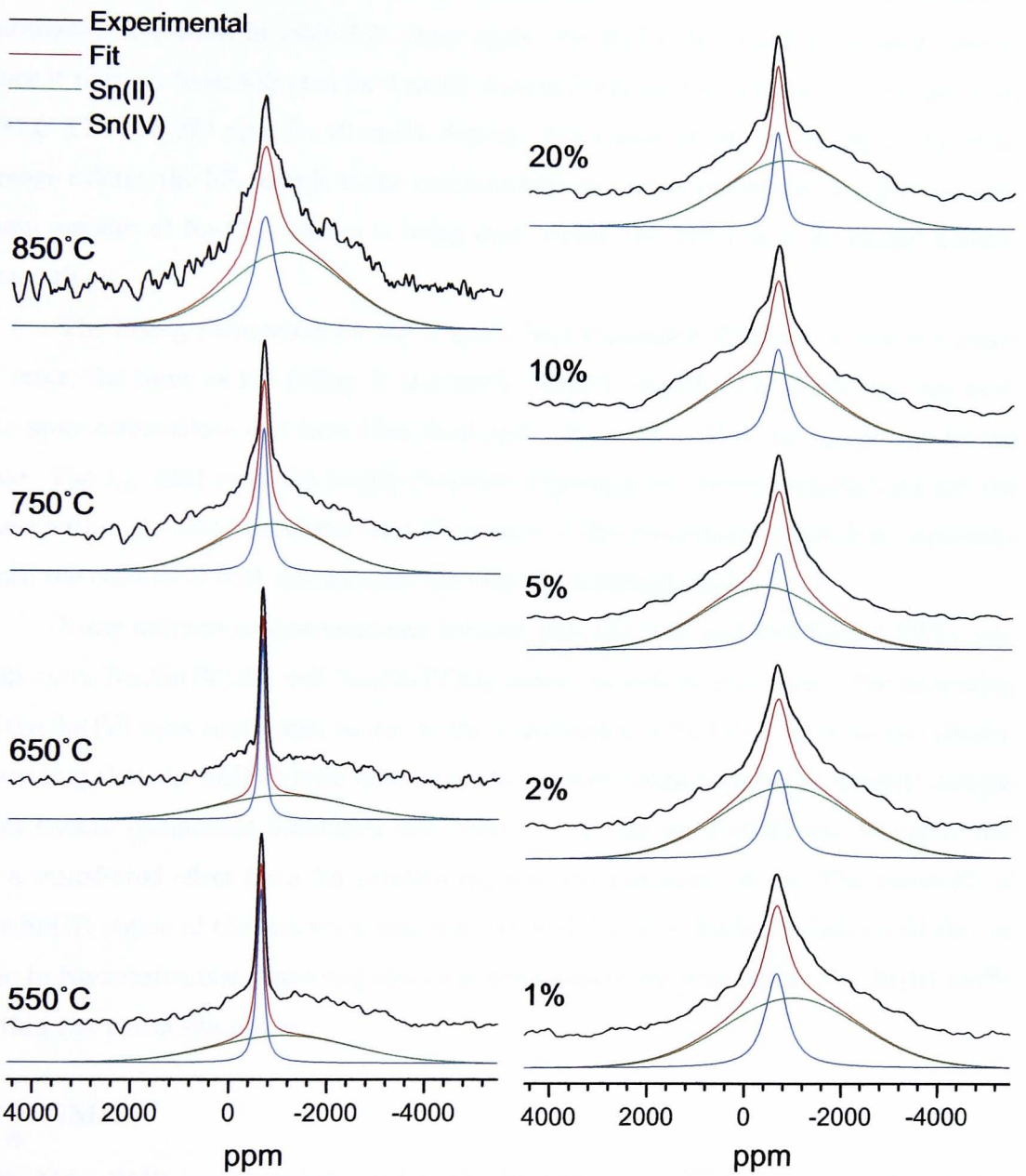

Figure 7.6: ^{119}Sn static NMR at 5.6 T of TZT doped with 5 mol% Na_2CO_3 which has been fired at different temperatures (left). Also plotted are the ^{119}Sn static NMR spectra of TZT doped with differing amounts of Na_2CO_3, fired at 850°C.

has been completed.

Also plotted in figure 7.6 are the variable Na_2CO_3 content TZTs, and the fitting parameters are listed in table 7.3. Once again, the Sn(IV) linewidth is of most interest since it narrows from 550 ppm for 1 mol% doping (compared to 540 ppm for the undoped 900°C TZT) to 274 ppm for 20 mol% doping. The colour of the 1%-doping is the usual orange colour, the 5% sample is the commercially marketed yellow colour since the optimum amount of Na_2CO_3 source is being used, whilst the 20% colour developed a slight green tinge.

The fitting parameters for the 5 mol% Na_2CO_3-loaded TZT are, within the limits of error, the same as the fitting of the 850°C Na_2CO_3 doped TZT. Since they are both the same composition and have been fired under the same conditions, this should be the case. The δ_{iso} used to fit the Sn(II) Gaussian lineshapes for the two samples are not the same within the error estimates, and the source of this discrepancy is unclear, especially since the colours of both the samples are visually indistinguishable.

X-ray diffraction measurements indicate that the 10% and 20%-loaded TZTs contain extra $Na_2Sn(IV)_2O_5$ and $Na_2Sn(IV)O_3$ phases as well as murataite. The narrowing of the Sn(IV) peak could then be due to the contribution of Sn(IV) from these two phases, providing that the Sn(IV) local environments in these compounds are symmetric enough that narrow component lineshapes are created. The narrowing could also be partly due to a transferred effect from Na substituting into the murataite phase. The linewidth of the Sn(II) region of the spectrum also narrows with Na_2CO_3-loading which could also be due to Na-substitution distorting the local environment experienced by the Sn(II) nuclei within the murataite phase.

^{23}Na NMR

^{23}Na MAS NMR was also performed on the Na_2CO_3-doped TZTs to investigate how the Na_2CO_3 dopant responded to the heat treatments. Before ^{23}Na spectra were acquired on the doped-TZTs, spectra were recorded at 8.45 and 14.1 T for a series of Na-containing compounds which could have formed during sample firing. The high field results are plotted in figure 7.7 where a single 0.95 μs pulse was employed with a 10 s recycle delay.

The crystal structure of the room-temperature β-phase of Na_2CO_3 has recently

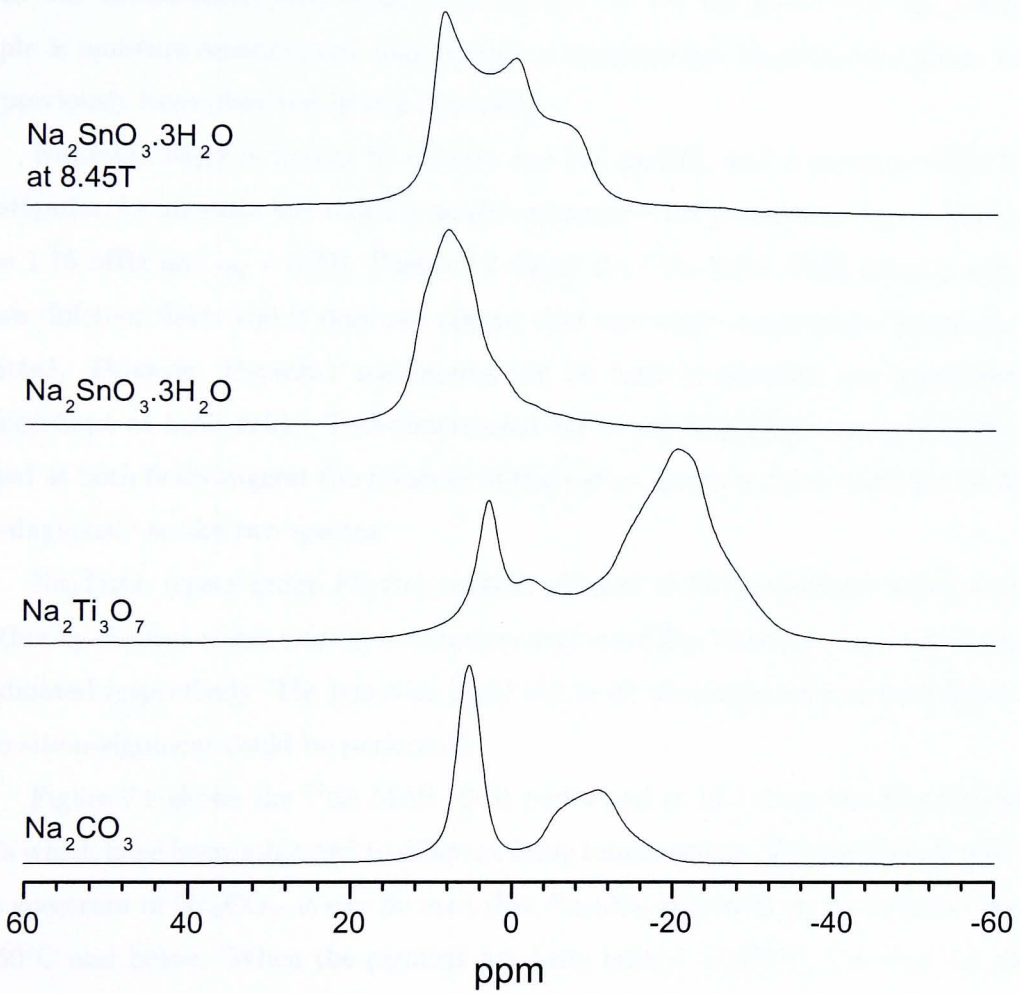

Figure 7.7: ^{23}Na MAS NMR at 14.1 T of Na-containing species that could have been formed during TZT firing. All samples are spinning at a minimum speed of 16 kHz.

been refined[34], and consists of two inequivalent NaO_6 octahedra and a much larger Na site. This latter site could be attributed to the resonance at 4 ppm which can be fit using the parameters $\delta_{iso} = 7.0$ ppm, $C_Q = 1.2$ MHz and $\eta_Q = 0.53$. These parameters were verified at a lower field where a consistent fit was achieved. The remaining two sites are then contained in the 0 to -20 ppm region. Fitting at multiple fields of this region was inconclusive, and could be hampered by the likelihood that the reference sample is moisture sensitive and may contain a monohydrate $Na_2CO_3.H_2O$ phase which has previously been observed in this region[35].

$Na_2SnO_3.3H_2O$ is known to contain one Na site[36], and a previous ^{23}Na NMR investigation by Hayashi has found a single resonance with parameters $\delta_{iso} = 12.8$ ppm, $C_Q = 1.76$ MHz and $\eta_Q = 0$[37]. Figure 7.7 shows the ^{23}Na MAS NMR spectra acquired at two different fields and it does not appear that one single quadrupolar lineshape can be fitted. However, Hayashi's parameters can be used to simulate one component of the lineshape at both fields. Two-dimensional $3Q \rightarrow 1Q$ MQMAS experiments[38] performed at both fields suggest the presence of three sites, however these could not be fitted unambiguously to the two spectra.

$Na_2Ti_3O_7$ (space group $P2_1/m$) consists of layers of TiO_6 octahedra which are held together by Na ions which exist in two inequivalent sites[39]. These are nine and sevenfold coordinated respectively. The two sites could not be fit unambiguously at both fields and so no site assignment could be performed.

Figure 7.8 shows the ^{23}Na MAS NMR performed at 14.1 T on the Na_2CO_3-doped TZTs which have been subjected to different firing temperatures. By comparison with the ^{23}Na spectrum of Na_2CO_3, it can be seen that Na_2CO_3 is present in the samples heated to 750°C and below. When the pigment has been heated to 850°C, the Na_2CO_3 phase is obscured by a broader peak at ~ -18 ppm, however some Na_2CO_3 is likely to remain since there is still a slight peak at 5 ppm in the 850°C sample. The broader peak could be Na which has been incorporated into the murataite phase, and it could also contain separate Na-phases which have formed from the Na_2CO_3. However, the ^{23}Na MAS NMR spectrum does not provide sufficient resolution to allow the final Na-containing phases to be unambiguously identified.

The ^{23}Na spectra for the variable Na_2CO_3-content TZTs are also plotted in fig-

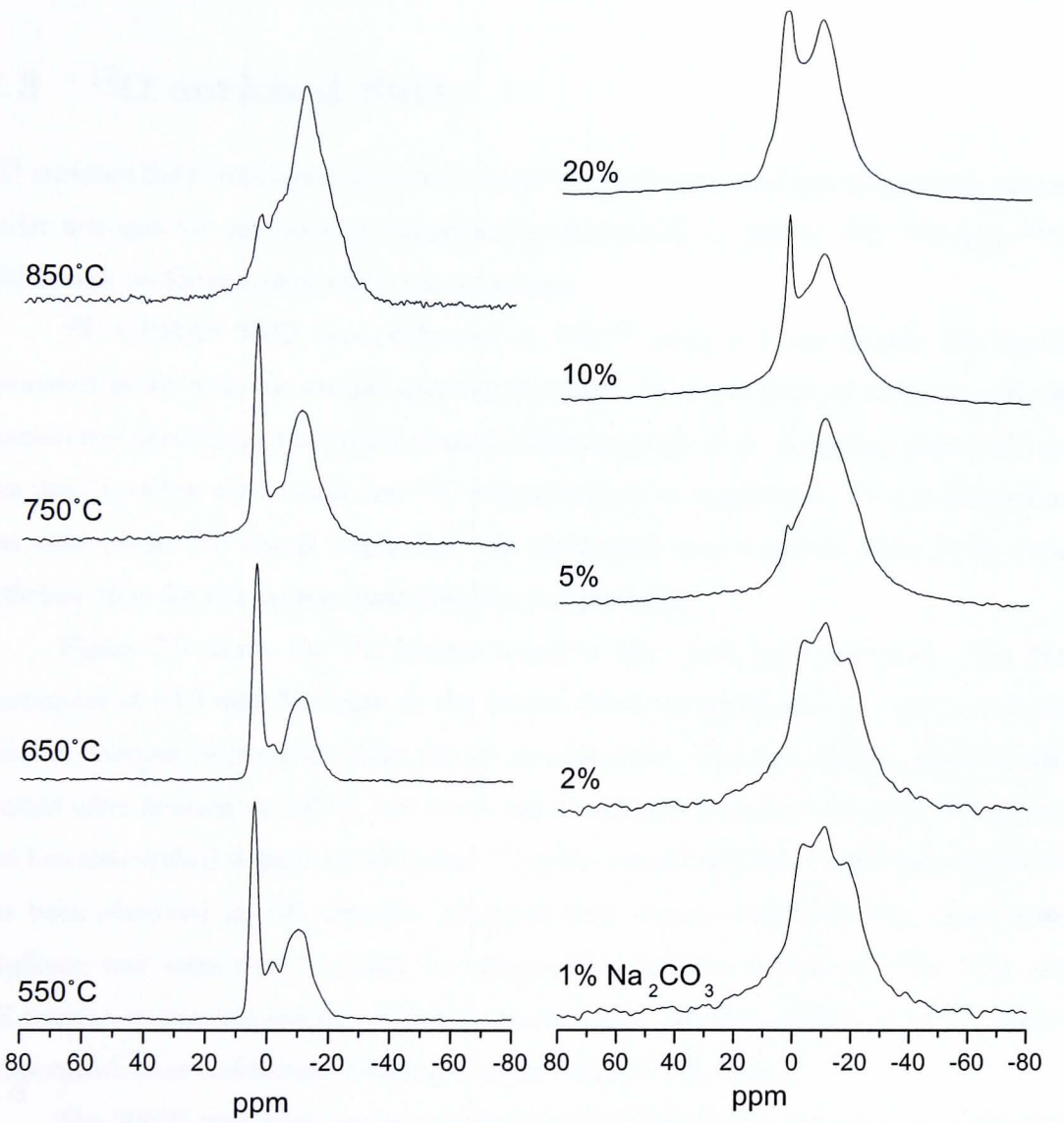

Figure 7.8: ^{23}Na MAS NMR performed at 14.1 T on Na_2CO_3-doped TZT fired at different temperatures (left), and variable Na_2CO_3 doped TZT fired at 850°C (right). All samples were spinning at 16 kHz.

ure 7.8, and the 5% spectrum is identical to the 850°C spectrum since they are both 5% Na_2CO_3 TZT which has been heated to 850°C. The 10% and 20% spectra appear to indicate that the excess Na_2CO_3 is remaining in the β-form which was measured in figure 7.7. The 1% and 2% samples do not contain the Na_2CO_3 singularity at -18 ppm.

7.3 ^{17}O enriched SnO_2

^{17}O enriched SnO_2 was manufactured through a sol-gel route, and was successively heated under nitrogen for one hour at temperatures of $150, 300, \ldots, 900$°C. ^{13}C, ^{17}O and ^{119}Sn NMR were performed after each heat treatment.

^{13}C CPMAS NMR was performed at 7.05 T using a 7 mm Bruker DB double resonance probe with the sample spinning at 4 kHz. An initial pulse of 12.5 μs on the H-channel was used to tip the proton magnetisation an angle of $\frac{\pi}{2}$. A contact period of 1 ms was used to allow the proton and ^{13}C magnetisation to equilibrate. Proton decoupling was used whilst ^{13}C signal acquisition was performed, and a recycle delay of 20 s was sufficient time for the proton magnetisation to fully relax.

Figure 7.9 shows the ^{13}C spectra acquired after each heat treatment. The two resonances at 64.3 and 24.9 ppm in the unfired SnO_2 gel correspond to middle and end member carbons respectively from the tin isopropoxide. The end member signal is also present after heating to 150°C, however it has broadened from $\Delta = 3.3$ ppm to 8.3 ppm, and has also shifted slightly to 24.9 ppm. This line broadening effect after heat treatment has been observed in SiC ceramics prepared from organic precursors[40]. The broad lineshape was attributed to being the compound lineshape created by CH_3, CH_2 and CH present within the sample. The broadening effect was then explained by the higher temperature heat treatments creating a wider range of CH_n species.

The 300°C spectrum contains another broad resonance at 130 ppm ($\Delta = 33$ ppm) which has two spinning sidebands associated with it. This is likely to be sp^2-hybridised carbon[41] and unsaturated carbon atoms[40]. The broad peak at 15 ppm ($\Delta = 30$ ppm) is still due to CH_n groups, and this resonance is now much broader than at 150°C. This signal is removed when the sample is heated to 450°C, and the sp^2-hybridised signal has now shifted slightly to more negative ppm, and no longer has any sidebands.

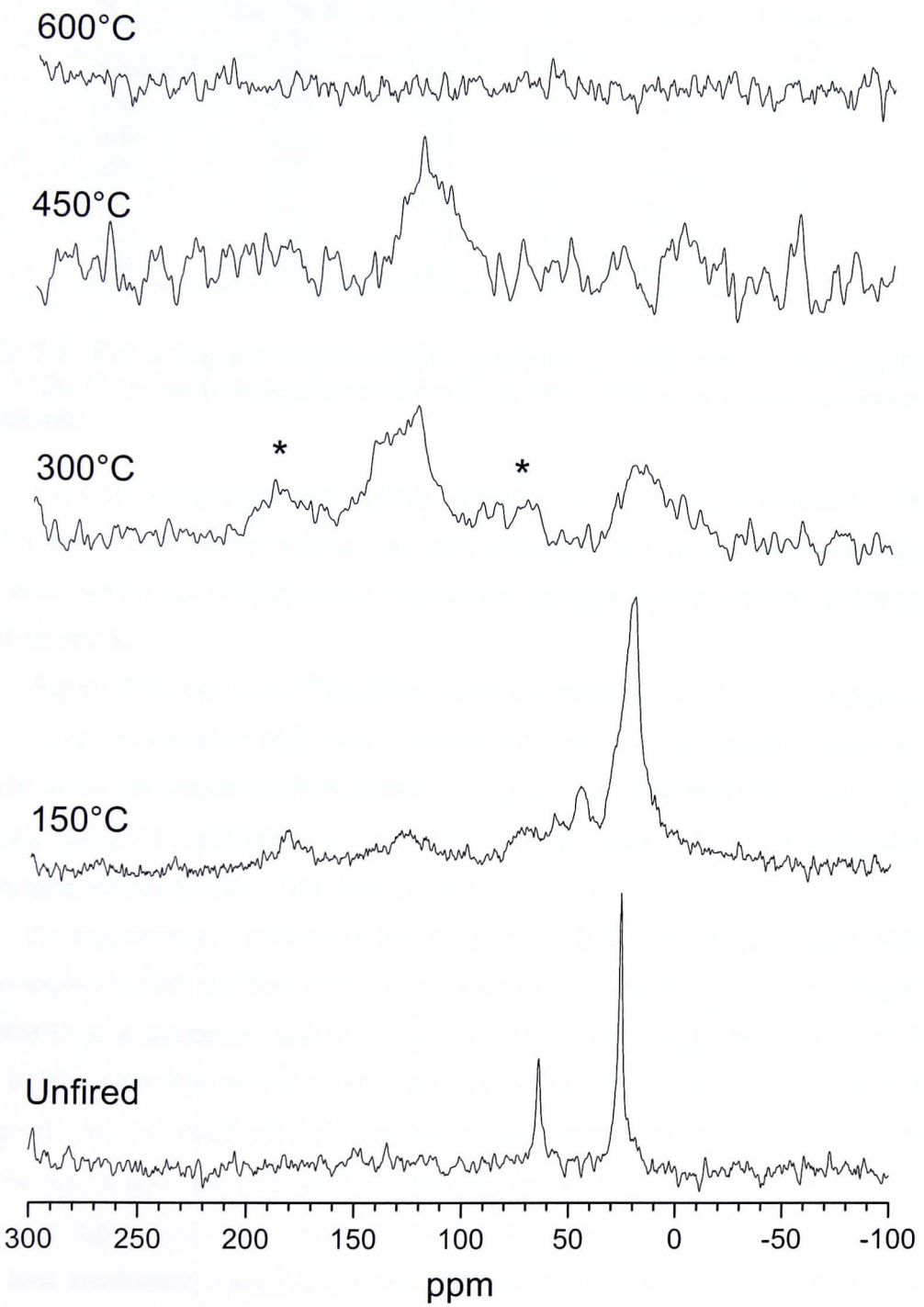

Figure 7.9: ^{13}C CPMAS NMR at 7.05 T of the SnO_2 sol-gel after successive heat treatments, spinning at 4 kHz.

°C	^{17}O at 8.45 T			^{119}Sn at 5.6 T	
	δ_{iso} (ppm) ±10	C_Q (MHz) ±0.4	η_Q ±0.2	δ_{iso} (ppm) ±2	Δ (ppm) ±4
unheated	125	5.8	0.2	−605	69
150	130	6.0	0.3	−606	70
300	120	6.0	0.2	−605	20
450	105	5.7	0.0	−606.6	16
600	111	5.9	0.0	−604.3	7
750	111	5.7	0.0	−604.5	5
900	100	5.7	0.0	−603.4	7

Table 7.4: The fitting parameters used to simulate ^{17}O MAS NMR at 5.6 and 8.45 T, and ^{119}Sn MAS NMR experiments at 5.6 T on the SnO_2 sol-gel, after successive heat treatments.

Once the sample has been heated to 600°C, no ^{13}C signal is measured. This indicates either that all the carbon has been removed, or that any carbon species still contained within the sample do not contain any protons, and so cannot be detected by CPMAS NMR.

Figure 7.10 shows the ^{119}Sn MAS NMR performed at 5.6 T on the sol-gel. Since only 1 g of ^{17}O enriched SnO_2 was synthesised, there was not enough sample to fill a 9.5 mm rotor for a static echo experiment. A Doty 4 mm DB DD MAS probe was used instead, and the sample was spun at 16 kHz. A single pulse of 1 μs was sufficient to tip the magnetisation $\frac{\pi}{6}$, and a recycle delay of 4 s was used.

A single resonance is observed for all heat treatments, and the position of −604 ppm is the expected shift for SnO_2[25]. X-ray phase analysis performed on the sample after the 900°C heat treatment indicated that the only crystalline phase present was SnO_2. The width of the line decreases after successive heat treatments which is likely to be due to the level of chemical shift dispersion being reduced as the SnO_2 gel crystallises. The linewidth has been measured for every temperature, and is listed in table 7.4 and plotted in figure 7.11. The linewidth is reduced the most by the 300°C firing, and further heat treatments narrow much less, with the width remaining reasonably constant after 600°C. These findings are consistent with a recent TEM study on sol-gel produced SnO_2 which found that extensive crystallisation occurred between 300°C and 500°C heat treatments[22].

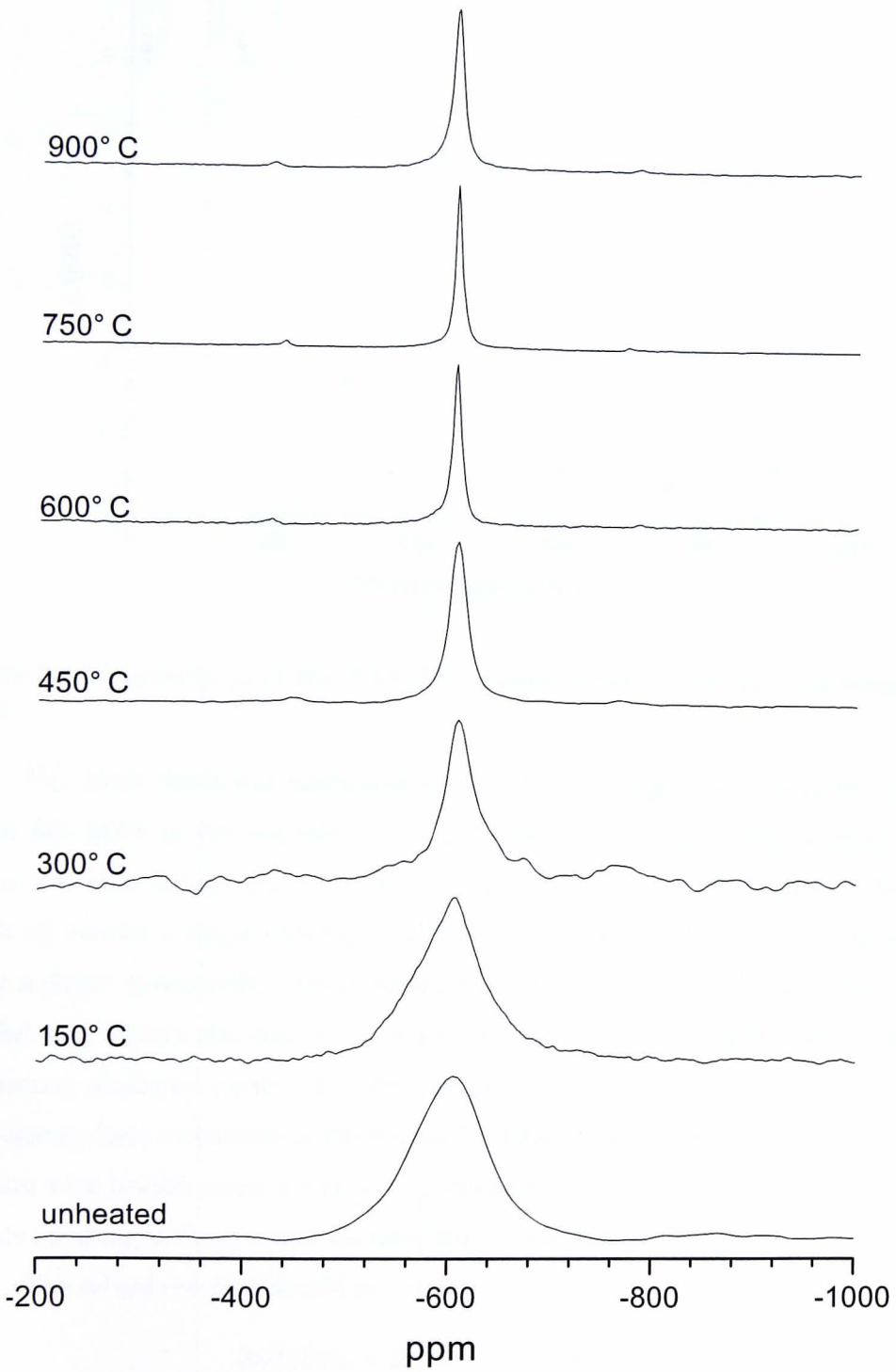

Figure 7.10: ^{119}Sn MAS NMR at 5.6 T of the SnO_2 sol-gel, spinning at 16 kHz.

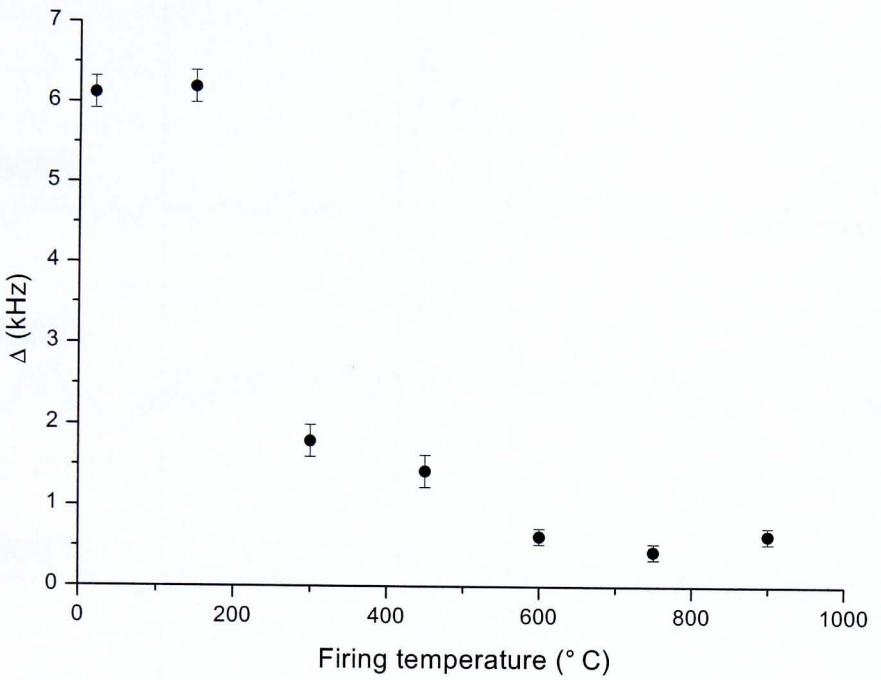

Figure 7.11: Linewidth Δ of the ^{119}Sn SnO_2 sol-gel linewidth varying with firing temperature.

^{17}O MAS NMR was performed at 8.45 T after each heat treatment. A Bruker 4 mm DB MAS probe was used to spin the sol-gel at 10 kHz, and a single pulse of 1.6 μs was used along with a 2 s recycle delay. The spectra are plotted in figure 7.12 which all exhibit a single lineshape. This has been simulated for every heat treatment using a single quadrupolar central transition lineshape, and every simulation has been verified with spectra also acquired at a field of 5.6 T to further constrain the quadrupolar parameters employed (table 7.4). The signal-to-noise ratio in the spectra of the higher temperature heat treatments is worse than for those at lower temperatures. Although the samples were heated under a nitrogen atmosphere, some ^{17}O has still been lost from the sample resulting in fewer nuclei contributing to the NMR experiment.

The sol-gel reaction should proceed as

$$Sn(OPr)_4 + 2H_2^{17}O \rightarrow Sn^{17}O_2 + 4PrOH \tag{7.1}$$

so the only ^{17}O enriched species should be SnO_2, unless ^{17}O has labelled any PrOH reaction products. The quadrupolar parameters used to simulate all spectra are very

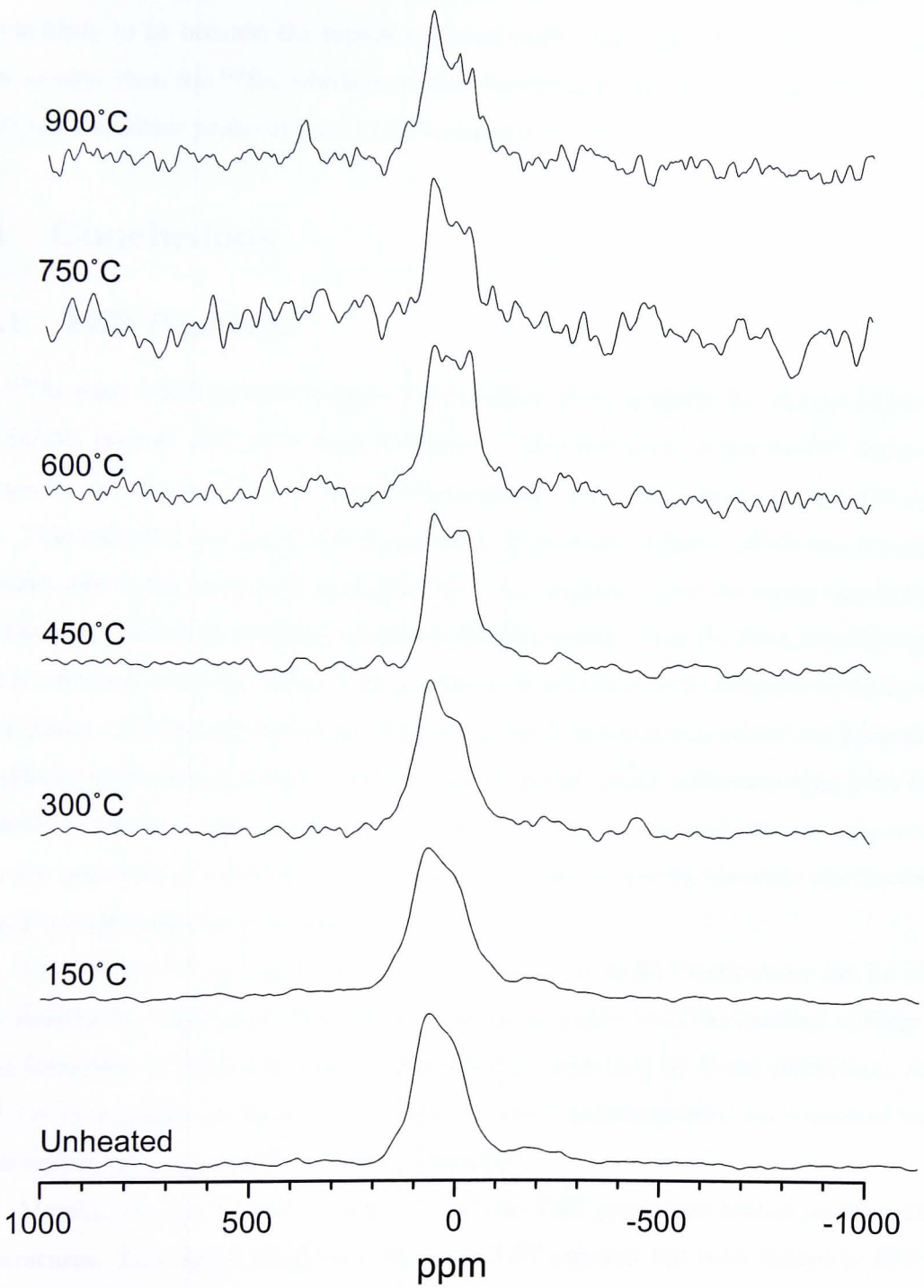

Figure 7.12: ^{17}O MAS NMR at 8.45 T of the SnO_2 sol-gel, spinning at 10 kHz.

similar within error estimates, so the ^{17}O resonances observed here are much less sensitive to the degree of crystallisation of the sample than the ^{119}Sn resonances in figure 7.10. This is likely to be because the typical chemical shift range experienced by ^{17}O nuclei is much smaller than for ^{119}Sn, which is a much heavier nucleus. This causes ^{119}Sn to be a much more sensitive probe of local order compared to ^{17}O.

7.4 Conclusions

7.4.1 TZT Pigments

The ^{119}Sn static NMR spectra in figure 7.3 can all be fit to quantify the amount of Sn(II) and Sn(IV) present after each heat treatment. The linewidth of the Sn(IV) region of the spectra is very sensitive to sample preparation, and below 700°C is only 150 ppm wide. This indicates that Sn(IV) is still present in the form of SnO_2, which has a narrow linewidth due to the symmetric arrangement of six oxygens about the probe tin nucleus. This linewidth broadens at higher temperatures which shows that the final murataite pigment has formed, since the probe ^{119}Sn nucleus is located in a more distorted environment in this phase. The linewidth then narrows when this is subjected to additional heating in an oxidising environment. This is because the murataite phase is decomposing back into the SnO_2 precursor. This shows that formation of the murataite phase can only occur when the reactants are heated in a closed environment to prevent tin-oxide species from forming in preference to murataite.

From figure 7.6 and table 7.3, the linewidth of the Sn(IV) component can be seen to be sensitive to Na_2CO_3-loading. The narrowing at higher Na_2CO_3-loadings is likely to be the formation of Na-Sn(IV)-oxides, which is also confirmed by X-ray diffraction. Any Sn(IV) in these oxides are likely to be in less distorted crystallographic environments than in murataite, resulting in a the narrower linewidth.

Metallic tin can be seen in figure 7.4 of the TZT precursors heated to increasing temperatures. This signal disappears when the TZT pigment has been heated to 800°C, which is the same temperature where Murataite formation is seen to commence. Upon sample firing, at lower temperatures SnO must degrade into Sn metal and SnO_2. These recombine at a temperature between 700 and 800°C to form the final murataite pigment.

To further interrogate the local structure of murataite, ^{17}O enrichment was attempted by synthesising TZT using ^{17}O-enriched TiO_2. The enrichment of TiO_2 was successful, however no coloured TZTs could be created. This could be due to the particle size distribution of the enriched TiO_2 not being optimised for ceramic manufacture. It could also be due to the sol-gel-produced TiO_2 containing organic impurities which upset the delicate non-oxidising environment required for TZT formation. This latter effect is less likely since a ^{17}O-enriched TiO_2 sample was calcined at 600°C for 2 h under a nitrogen atmosphere to attempt to remove any organic species prior to TZT manufacture, and this still resulted in a colourless sample. Any organic residues formed during calcination could still interfere with the reaction though. Trace levels of oxygen in the nitrogen atmosphere are unlikely to be the cause of the problem since a rehearsal using non-enriched TiO_2 resulted in a vibrant orange coloured sample.

7.4.2 ^{17}O enriched SnO_2

^{13}C CPMAS NMR of the sol-gel produced SnO_2 indicates that $Sn(OPr)_4$ begins to decompose when heated to 150°C. By 300°C, only sp^2-hybridised carbon and unsaturated carbon can be seen. When heated to 600°C, there were either no carbon-containing species remaining, or any carbon present was not linked to any protons and could not be detected by CPMAS NMR.

^{119}Sn MAS NMR shows quantitatively the degree of crystallisation of SnO_2, which increases sharply once the sample had been heated to 300°C, with continued ordering throughout subsequent heat treatments. ^{17}O MAS NMR at two magnetic fields allows the quadrupolar parameters at the Sn-O-Sn bond to be measured. The crystallinity of the sample did not have as big an influence on the ^{17}O quadrupolar parameters as it had on the ^{119}Sn linewidth. This is because ^{17}O is a relatively light isotope compared to ^{119}Sn which has a much wider chemical shift range, and is a more sensitive probe of local order.

References

[1] J. W. Jenkins and J. Wolstenholme, Colored inorganic complex for use as a pigment and compositions containing it, *United States Patent*, 4,448,608 (1984).

[2] J. W. Jenkins and J. Wolstenholme, Colored inorganic complex for use as a pigment and compositions containing it, *European Patent Application*, 0 113 229 (1983).

[3] S. Ishida, F. Ren, N. Takeuchi, New yellow ceramic pigment based on codoping pyrochlore-ytpe $Y_2Ti_2O_7$ with V^{5+} and Ca^{2+}, *Journal of the American Ceramic Society*, **76** 2644 (1993).

[4] I. Campbell, Lead and cadmium free glasses and frits, *Glass Technology*, **39** 38 (1998).

[5] M. Jansen and H. P. Letschert, Inorganic yellow-red pigments without toxic metals, *Nature*, **404** 980 (2000).

[6] J. W. Adams, T. Botinelly, W. N. Sharp and K. Robinson, Murataite: a new complex oxide from El Paso county, Colorado, *American Mineralogist*, **59** 172 (1974).

[7] T. S. Ercit and F. C. Hawthorne, Murataite, a UB_{12} derivative structure with condensed keggin molecules, *The Canadian Mineralogist*, **33** 1223 (1995).

[8] M. J. Fuller and M. E. Warwick, The catalytic oxidation of carbon monoxide on tin(IV) oxide, *Journal of Catalysis*, **29** 441 (1973).

[9] T. Seiyama, A. Kato, K. Fujishi and M. Nagatani, A new detector for gaseous components using semiconductive thin films, *Analytical Chemistry*, **34** 502 (1962).

[10] K. L. Chopra, S. Major and D. K. Pandya, Transparent conductors - a status review, *Thin Solid Films*, **102** 1 (1983).

[11] J. Proscia and R. G. Gordon, Properties of fluorine-doped tin oxide-films produced by atmospheric-pressure chemical vapor-deposition from tetramethyltin, bromotrifluoromethane and oxygen, *Thin Solid Films*, **214** 175 (1992).

[12] W. H. Baur, Über die verfeinerung der kristallstrukturbestimmung einiger vertreter des rutiltyps: TiO_2, SnO_2, GeO_2 und MgF_2, *Acta Crystallographica*, **9** 515 (1956).

[13] K. N. P. Kumar, A. Keizer, A. J. Burggraff, T. Okubo and H. Nagamoto, Synthesis and textural properties of unsupported and supported rutile (TiO_2) membranse, *Journal of Materials Chemistry*, **3** 923 (1993).

[14] T. J. Bastow, L. Murgaski, M. E. Smith and H. J. Whitfield, Atomic ordering in tin-containing titania gels, *Materials Letters*, **23** 117 (1995).

[15] S. K. Kulshreshtha, R. Sasikala and V. Sudarsan, Non-random distribution of cations in $Sn_1 - xTi_xO_2$ $(0.0 \leq x \leq 1.0)$: a ^{119}Sn MAS NMR study, **11** 930 (2001).

[16] M. J. Hampden-Smith, T. A. Wark and C. J. Brinker, The solid state and solution structures of tin(IV) alkoxide compounds and their use as precursors to form tin oxide ceramics via sol-gel-type hydrolysis and condensation, *Coordination Chemistry Reviews*, **112** 81 (1992).

[17] M. A. Aegerter, A. Reich, D. Ganz, G. Gasparro, J. Pütz and T. Krajewski, Comparative study of SnO_2:Sb transparent conducting films produced by various coating and heat treatment techniques, *Journal of Non-Crystalline solids*, **218** 123 (1997).

[18] A. Gamard, B. Jousseaume, T. Toupance and G. Campet, New fluorinated stannic compounds as precursors for F-doped SnO_2 materials prepared by the sol-gel route, *Inorganic Chemistry*, **38** 4671 (1999).

[19] J. F. Goodman and S. J. Gregg, The production of active solids by thermal decomposition. Part XI. The heat treatment of precipitated stannic oxide, *Journal of the Chemical Society*, **237** 1162 (1960).

[20] B. Orel, U. Lavrencic-Stangar, Z. Crnjak-Orel, P. Bukovec and M. Kosec, Structural and FTIR spectroscopic studies of gel-xerogel-oxide transitions of SnO_2 and SnO_2:Sb powders and di-coated films prepared via inorganic sol-gel route, *Journal of Non Crystalline Solids*, **167** 271 (1994).

[21] Q. Li, X. Yuan, G. Zeng and S. Xi, Study on microstructure and properties of nanosized stannic oxide powders, *Materials Chemistry and Physics*, **47** 239 (1997).

[22] I. A. Rusakova, A. Homed and A. P. Litvinchuk, Evolution in structural and optical properties of stannic oxide xerogel upon heat treatment, N. Wu, L. Wu, I. A. Rusakova, A. Hamed and A. P. Litvinchuk, *Journal of the American Ceramic Society*, **82** 67 (1999).

[23] N. J. Clayden, C. M. Dobson and A. Fern, High-resolution solid-state tin-119 nuclear magnetic resonance spectroscopy of ternary tin oxides, *Journal of the Chemistry Society Dalton Transactions*, 843 (1989).

[24] A. Sebald, L. H. Merwin, W. A. Dollase and F. Seifret, A multinuclear, high-resolution solid-state NMR-study of sorensenite $(Na_4SnBe_2(Si_3O_9).2H_2O)$ and comparison with wollastonite and pectolite, *Physics and Chemistry of Materials*, **17** 9 (1990).

[25] C. Cossment, J. Darville, J. M. Gilles, J. B. Nagy, C. Fernandez and J. P. Amoureux, Chemical shift anisotropy and indirect coupling in SnO_2 and SnO, *Magnetic Resonance in Chemistry*, **30** 263 (1992).

[26] K. J. D. MacKenzie and M. E. Smith, *Multinuclear Solid-state NMR of Inorganic Materials*, Pergamon, Amsterdam, 2002.

[27] N. Bloembergen and T. J. Rowland, On the nuclear magnetic resonance in metals and alloys, *Acta Metallurgica*, **1** 731 (1953).

[28] B. Langer, I. Schnell, H. W. Spiess and A. R. Grimmer, Temperature calibration under ultrafast MAS conditions, *Journal of Magnetic Resonance*, **138** 182 (1999).

[29] P. J. Titler and J. Silver, The University of Greenwich (unpublished).

[30] R. H. Herber, Mössbauer lattice temperatures of tetragonal ($P4/nmm$) SnO, *Physical Review B*, **27** 4013 (1983).

[31] J. L. Solis, J. Frantti, V. Lantto, L. Häggström and M. Wikner, Characterization of phase structures in semiconducting $SnWO_4$ powders by Mössbauer and Raman spectroscopies, *Physical Review B*, **57** 13491 (1998).

[32] M. S. Moreno and R. C. Mercader, Mössbauer study of SnO lattice dynamics, *Physical Review B*, **50** 9875 (1994).

[33] J. Chouvin, J. Olivier-Fourcade, J. C. Jumas, B. Simon, P. Biensan, F. J. Fernádez Madrigal, J. L. Tirado, C. Pérez Vicente, SnO reduction in lithium cells: study by X-ray absorption, ^{119}Sn Mössbauer spectroscopy and X-ray diffraction, *Journal of Electroanalytical Chemistry*, **494** 136 (2000).

[34] I. P. Swainson, M. T. Dove and M. J. Harris, Neutron powder diffraction study of the ferroelastic phase transition and lattice melting in sodium carbonate, Na_2CO_3, *Journal of Physics: Condensed Matter*, **7** 4395 (1995).

[35] J. M. Egan and K. T. Mueller, Detection and identification of corrosion products of sodium aluminoborosilicate glasses by ^{23}Na MQMAS and ^{1}H $\rightarrow$ ^{23}Na CPMAS NMR, *Journal of Physical Chemistry B*, **104** 9580 (2000).

[36] C. O. Bjoerling, The crystal structure of Potassium hydroxostannate and some related compounds, *Arkiv foer Kemi, Mineralogi och Geologi, B*, **15** 1 (1942).

[37] S. Hayashi, Magic-angle spinning nuclear magnetic resonance of half-integer quadrupolar nuclei: effect of spin-locking efficiency on powder lineshapes, *Solid State Nuclear Magnetic Resonance*, **3** 93 (1994).

[38] S. P. Brown and S. Wimperis, Two-dimensional multiple-quantum MAS NMR of quadrupolar nuclei. Acquisition of the whole echo, *Journal of Magnetic Resonance*, **124** 279 (1997).

[39] S. Andersson and A. D. Wadsley, The crystal structure of $Na_2Ti_3O_7$, *Acta Crystallographica*, **14** 1245 (1961).

[40] G. D. Soraru, F. Babonneau and J. D. MacKenzie, Structural evolutions from polycarbosilane to SiC ceramic, *Journal of Materials Science*, **25** 3886 (1990).

[41] N. Suyal, D. Hoebbel, M. Menning and H. Schmidt, A solid state ^{29}Si and ^{13}C study on the synthesis of thin silicon-oxycarbide glass sheets by a sol-gel route, *Journal of Materials Chemistry*, **9** 3061 (1999).